Human Skin Modelling and Rendering

by

Guillaume Poirier

A thesis
presented to the University of Waterloo
in fulfilment of the
thesis requirement for the degree of
Master of Mathematics
in
Computer Science

Waterloo, Ontario, Canada, 2003

Abstract

Creating realistic-looking skin is one of the holy grails of computer graphics and is still an active area of research. The problem is challenging due to the inherent complexity of skin and its variations, not only across individuals but also spatially and temporally among one. Skin appearance and reflectance vary spatially in one individual depending on its location on the human body, but also vary temporally with the aging process and the body state. Emotions, health, physical activity, and cosmetics for example can all affect the appearance of skin. The spatially varying reflectance of skin is due to many parameters, such as skin micro- and meso-geometry, thickness, oiliness, and pigmentation. It is therefore a daunting task to derive a model that will include all these parameters to produce realistic-looking skin. The problem is also compounded by the fact that we are very well accustomed to the appearance of skin and especially sensitive to facial appearances and expressions. Skin modelling and rendering is crucial for many applications such as games, virtual reality, films, and the beauty industry, to name a few. Realistic-looking skin improves the believability and realism of applications. The complexity of skin makes the topic of skin modelling and rendering for computer graphics a very difficult, but highly stimulating one. Skin deformations and biomechanics is a vast topic that we will not address in this dissertation. We rather focus our attention on skin optics and present a simple model for the reflectance of human skin along with a system to support skin modelling and rendering.

Acknowledgements

I would like to thank professors William Cowan (University of Waterloo) and Pierre Poulin (Université de Montréal) for their expertise, guidance, and support throughout my Master's degree. This work would have been impossible without them and I have an immense respect and gratitude for these devoted individuals. I would also like to thank professors Craig Kaplan and Forbes Burkowski for agreeing to read my thesis. Their comments and recommendations were all helpful. I would also like to thank Steven Stahlberg for interesting discussions about skin rendering. His work on skin as a 3D artist is both impressive and stimulating.

I would like to thank the graduate students at the University of Waterloo Computer Graphics Lab and at the Laboratoire d'Informatique Graphique de l'Université de Montréal with whom I spent countless hours. Their support was much appreciated. I would specifically like to thank Kevin Moule, Tiberiu Popa, and François Duranleau for their technical help. They are among the best programmers I have met in my life. Kevin Moule provided some code for pBuffers and Worley textures and fixed many bugs in my programs. Tiberiu Popa provided some code for loading geometry, François Duranleau for generating simple objects, Pierre-Marc Jodoin for creating centroidal Voronoi diagrams and helped me with LaTeX issues. François Duranleau, Mathieu Ouimet, Emric Epstein, and Martin Granger-Piché were always helpful with C++, Cg, and Qt issues.

Finally, I would like to thank my family, my father for moving me several times between Montréal and Waterloo, and Geneviève Denis for coping with my graduate lifestyle and my frequent exiles in Waterloo. I also thank her and Tiberiu Popa for allowing me to use their pictures and 3D head models in this work.

This thesis was partially funded by a FCAR scholarship (Le Fonds Québécois de la Recherche sur la Nature et les Technologies, now FQRNT) and by the University of Waterloo under the form of Teaching and Research assistantships.

Trademarks

SpectroScan is a registered trademark of Gretag Macbeth.

OpenGL is a registered trademark of SGI.

Cg is a registered trademark of Nvidia.

3D Capturor is a registered trademark of Inspeck.

Maya and *Maya Skin Shader* are registered trademarks of Alias|Wavefront.

Cover Girl is a registered trademark of Procter & Gamble.

The 3D head model used in Plates XVI and XIX is courtesy of Nvidia corporation.

All other products mentioned in this thesis are trademarks of their respective companies.

The copyright for Figure 2.1 (2001) is held by Benjamin Cummings, an imprint of Addison Wesley Longman, Inc.

The copyright for Figure 2.4 (2001) is held by Freinkel and Woodley, an imprint of CRC Press-Parthenon Publishers, Inc.

The copyright for Plate II and III (1999) is held by Angelopoulou.

The copyright for Figure 2.6 (1999) is held by Marschner, Westin, Lafortune, Torrance, and Greenberg.

The copyright for Figure 3.2 (2002) is held by Meglinski and Matcher.

The copyright for Figures 3.8 and 3.9 (2002) is held by Koenderink and Pont.

The copyright for Figure 3.7 (1974) is held by Montagna and Parakkal, an imprint of Academic Press, Inc.

The copyright for Plate VIII (2001) is held by Kukla and Bedwell.

The copyright for Plate X (2003) is held by Macy.

Contents

List of Tables

List of Figures

Chapter 1

Introduction

> *"CG artists will capture the holy grail of animation when they can bring virtual skin to life."*
>
> - Joel L. Swerdlow, "Unmasking Skin", National Geographic (November 2002): 112-34.

The statement above reflects the fact that skin is probably one of the most difficult materials to reproduce in computer graphics imagery and that realistic portrayal of human skin is a problem of the utmost importance. There are several factors that distinguish skin from other materials and put it in a very special category. The first one is the complexity of the material itself; Chapter 2 is devoted to the anatomy and the optics of skin. We will see that skin is an intricate layered material whose internal and external structures vary with individuals, body locations, and time.

The second factor is a perceptual one. A person's skin — its shape, colour, and texture — provides the perceiver with a very large amount of information about their character, emotions, and health. Human perception is highly specialised for perception of skin, something that has long been known, implicitly or explicitly, by artists and perceptual scientists. Here are some examples.

- Some artists have been famous for bringing characters to life with their ability to create realistic skin. Guido Reni was known as 'the divine Guido' largely because of his ability to paint skin realistically [195].

- Make-up, which alters or improves the appearance of skin, is ubiquitous in everyday life, and even more so in film and theatre, where appearance conveys thoughts and feelings [20, 21, 52].

- Colour names label most colours prototypically or categorically. The exception is a collection of colours with names like 'tan', 'peach', 'light brown', and so on. All colours of human skin lie in this collection; clearly the human visual system processes these colours specially [30].

- Eight bit quantization of colour is adequate for most of the colour space, but finer quantization is necessary to get adequate resolution of skin colours. Experimental LCDs, with a fourth yellow pixel, have been tried as a method of solving this problem. Digital cameras manufacturers like *Canon* and *Nikon* already use a cyan, yellow, magenta, and green mask for their point-and-shoot cameras.

Examples like these show that human skin requires rendering methods that go beyond the requirements for other materials. Our contribution to skin modelling and rendering is twofold. First we present a simple model for the reflectance of human skin. Our model is physiologically-based and suitable to represent different body areas and skin types precisely and efficiently. Moreover, our model has physiological parameters — concentration of melanin, concentration of hemoglobin, and thicknesses of the various skin layers — that allow intuitive hand modelling by an artist. The implementation of the model uses simple arithmetic operations (multiply-accumulate) that can easily be implemented in current graphics hardware. Our model is derived as follows. First we start with skin anatomy and optics to construct a layered skin model. Making some assumptions on how the skin will be illuminated and viewed allows us to solve the equations of light transport in our layered skin model. We then compute reflectances for all plausible values of the model parameters. The resulting data is linearized using Principal Components Analysis in order to obtain an efficient and intuitive representation.

Second, we present a system to support human skin modelling and rendering. This system is a first step in developing efficient and intuitive high-level tools to support skin rendering. Artists can for example manipulate skin meso-geometry, oiliness, or other structures associated with skin like hairs. Specific user interfaces are provided in order to simplify the modelling process without hindering the artist's creativity and freedom.

We present in Chapter 2 a short review of the anatomy, physiology, and optics of skin. The reader already familiar with these topics may decide to skip to Chapter 3 where we present a survey of the techniques currently employed in computer graphics for rendering skin and discuss their advantages and disadvantages. We then continue with our implementation and results in Chapter 4, where we present a rendering technique that uses the optical properties of skin to provide a new way of calculating skin reflectance. We also present our system to support skin rendering in Chapter 4. Finally, we conclude and discuss future work in Chapter 5.

Our model is certainly not the last word on human skin, but one model among many, where the appropriate model to use in a given application depends on the resources available and the quality of results required. Rendering a material as varied and important as human skin is rarely possible within a single algorithmic framework.

Chapter 2

Anatomy, Physiology, and Optics of Skin

Skin is the largest body organ and forms the interface between the human body and the environment. Some of its functions are thermo-regulation, protection, metabolic functions, and tactile sensitivity. Skin tissue varies in thickness according to body location and wear-and-tear and this thickness variation contributes to the overall skin reflectance. Skin represents about $12 - 16\%$ of the total body mass and covers an area of about $1.2 - 2\ m^2$ in adults [151]. Skin tissue is also different between men and women, being generally less thick in women. The *stratum corneum* layer of the epidermis exhibits the greatest variation in thickness: in thin skin there may be fewer than 10 cell layers in the *stratum corneum* compared to over 100 layers in thick skin. The overall skin structure is constructed from three main layers: the epidermis, dermis, and hypodermis, as shown in Figure 2.1. Each structure provides a distinct role in the overall function of the skin. Skin reflectance is mainly determined by two pigments: melanin and hemoglobin. Skin optics have been investigated by several authors in medicine, biology, and biophysics [39, 54, 57, 94, 179, 202, 215, 218], to name a few. As we will discuss, skin is a highly scattering media, i.e., scattering is much more important than absorption, and it also exhibits a strong forward scattering behaviour. Skin models are complicated by the fact that skin is irregularly shaped, inhomogeneous, multi-layered, has anisotropic physical properties, and has hair follicles and glands [218]. The next sections provide descriptions of the anatomy, physiology, and optics of the various skin layers. The interaction of light with skin plays a metabolic function since the action of light on a precursor compound in the skin produces vitamin D which has a role in calcium and phosphate metabolism [232].

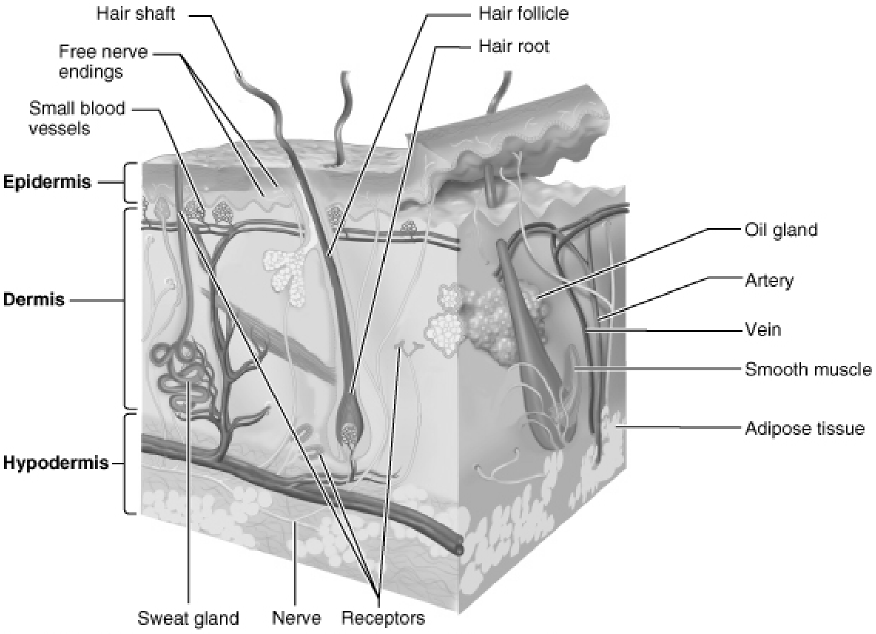

Figure 2.1: Epidermis, dermis, and subcutaneous tissue skin layers.

2.1 The Epidermis

The epidermis, sometimes called the epithelium, is the outermost layer of the skin. It is composed of a superficial layer of dead cells called keratinocytes. The epidermis also contains a pigment called melanin which contributes to the skin colouring. The epidermis, like other epithelia, does not contain any blood vessels. It contains some nucleic acids with an absorption peak at 260 *nm* and urocanic acids with a peak at 277 *nm* [46]. In the visible portion of the spectrum, however,

Body Site	Mean Thickness (μm)
Palm	429.0
Fingertip	369.0
Back of hand	84.5
Forearm	60.9
Upper arm	43.9
Thoracic region	37.6
Abdomen	46.6
Upper back	43.4
Lower back	43.2
Thigh	54.3
Calf	74.9
Forehead	50.3
Cheek	38.8

Table 2.1: Mean values for full epidermal thickness (data from Whitton and Everall [227]).

melanin is essentially the only chromophore affecting the transmittance of the epidermis [13]. It is well established that epidermal thickness varies considerably over the whole body surface and at comparable sites in different individuals. The variation in thickness throughout the body depends mainly on frictional forces and is thickest on the palms of the hands and soles of the feet. The mean values for epidermal thickness from a selected set of body sites are given in Table 2.1. The epidermis is subdivided into five layers, from the most superficial to the deepest: the *stratum corneum*, the *stratum lucidum*, the *stratum granulosum*, the *stratum spinosum*, and the *stratum germinativum*. Only thick skin (plantar and palmar regions) have all five layers easily recognisable [232]. The epidermis is constantly regenerated thanks to a mitotic layer of cells in its stratum germinativum layer. The generated keratinocyte cells migrate upward through the different layers, until they are keratinized at the skin surface.

Stratum Corneum

The stratum corneum, also called the horny layer, is the most superficial layer of the epidermis. It is mostly comprised of polygonal flattened dead cells filled with mature keratin. Keratinocyte cells are constantly pushed to the surface and gradually die and break apart, a process called desquamation. It is thought that as cells accumulate keratinohyalin granules, rupture of lysosomal membranes release lysosomal enzymes that eventually cause cell death. The whole keratinization process, from the stratum germinativum to the most superficial layer of the stratum corneum, takes about 15-30 days to accomplish. Van Gemert et al. [218] reports that a least squares fit identifies the Henyey-Greenstein phase function (Section A.11) as a good choice for describing scattering behaviour in the stratum corneum. The anisotropy factor g for the stratum corneum is approximately 0.9 with a tendency to increase with wavelength. The stratum corneum is covered with a thin layer of sebum, an oily-waxy material produced by the sebaceous glands. It keeps the stratum corneum layer flexible and water-resistant [232].

Stratum Lucidum

The stratum lucidum, also called the clear layer, is normally only distinguishable in thick epidermis and represents a transition from the stratum granulosum to the stratum corneum.

Stratum Granulosum

The keratinization process is characterised by the accumulation of keratin by the keratinocyte cells. The cells in the stratum granulosum, also called the granular layer, accumulate dense basophilic keratohyalin granules in their cytoplasm which give the layer its particular appearance. These granules contain lipids whose role is to help prevent fluid loss from the body. The stratum granulosum usually consists of about three to six layers of cells that are flattened and polygonal in shape. The keratohyalin granules also form the precursor material of the keratin which is found in the most superficial cells of the epidermis.

Stratum Spinosum

The stratum spinosum, also called the spiny layer, lies superficial to the stratum germinativum and consists of several layers of polyhedral cells. It is often called the prickle-cell layer or the Malpighian layer. This is because newly formed cells in the stratum germinativum accumulate desmosomes on their outer surface that give them their characteristic “prickles”.

Stratum Germinativum

The stratum germinativum, sometimes called the stratum basale, is the deepest layer of the epidermis. It is composed of a single layer of germinal cells necessary for the regeneration of the upper layers. The germinal cells are separated from the dermis by a thin layer of basement membrane. Mitotic processes in this base layer form new cells that will migrate upward through the different layers in a progressive maturation process of keratinization. The rate of proliferation of the cells of the stratum germinativum is under the influence of epidermal chalone, an hormone secreted by other cells of the epidermis. The production of this hormone is affected when we loose epidermis cells, whether by normal wear or due to an injury. The cells of the stratum germinativum usually appear cuboidal or low columnar in cross section.

2.1.1 Melanin Pigments

Melanin is a pigment produced by cells called melanocytes located in the stratum germinativum layer of the epidermis. Melanin is also present in the stratum spinosum. The more superficial layers of the epidermis contain no melanin pigment. The role of melanin is to protect the nuclear material of the mitotic cells from ultraviolet rays and the melanin absorption spectrum increases steadily toward shorter wavelengths to act as this protective filter. Szabò et al. [204] show that the different racial skin colours are due to differences in size, number, and distribution of melanosomes inside the keratinocytes of all the human races. Black skin absorbs 34% more radiant energy than white skin and the epidermis removes twice as much UVB radiation in black skin than white skin [77]. Melanin is found in skin, hair, and eyes. Two types of melanin pigments exist. The black-to-dark-brown insoluble pigment is called *eumelanin* and is found in skin, black hair, and in the retina of the eye. The yellow-to-reddish-brown alkali-soluble pigment found in red hair is called *pheomelanin*. All individuals have varying content of eumelanin in their epidermis whereas pheomelanin is only found among individuals who possess the corresponding genetic trait.

2.1.2 Baseline Skin Spectral Absorption Coefficient

"The optical properties of human skin are understandable." So says Steven Jacques in a very useful summary of medical research on the optical properties of skin [93, 94, 218]. The provided values are a starting point for describing the skin optics of any particular individual. The total optical absorption coefficient $\mu_{a.epidermis}$ of the epidermis depends on a minor baseline skin absorption and a dominant melanin absorption due to the melanosomes in the epidermis. The independent parameters that specify the absorption coefficient $\mu_{a.epidermis}$ are the wavelength λ and the volume fraction of melanosomes $f_{melanosome}$ in one individual, i.e., the proportion of melanosome volume over the total volume of tissue.

The baseline absorption accounts for skin absorption without melanin or hemoglobin pigments. The baseline absorption of both epidermis and dermis are approximated by the following absorption coefficient [94]:

$$\mu_{a.skinbaseline}(\lambda) = 0.244 \; + \; 85.3 \; e^{\frac{-(\lambda-154)}{66.2}} \qquad [cm^{-1}]. \tag{2.1}$$

Another measurement for the baseline absorption was done by Saidi [185]. The approximation function is

$$\mu_{a.skinbaseline}(\lambda) = (7.84 \times 10^{8}) \; (\lambda^{-3.255}) \qquad [cm^{-1}]. \tag{2.2}$$

According to Jacques [94], the first expression is based on measurements of bloodless rat skin using an integrating sphere calibrated with careful phantom measurements (R. Huang and S. Jacques, unpublished data). The second expression was generated with in vitro neonatal skin samples using an integrating sphere after accounting for excess absorption due to residual hemoglobin and bilirubin in the samples [185]. The second expression for neonatal skin is only a little higher in absorption than the first expression based on rat data. Again according to Jacques [94], the rat data was based on a more careful calibration of the integrating sphere apparatus and is consistent with the rather low absorption found by many researchers for bloodless tissues.

2.1.3 Water Spectral Absorption Coefficient

Some computational models of skin such as the Meglinski-Matcher model (Section 3.2) include water spectral absorption. We have plotted in Figure 2.2 the spectral absorption coefficient of water in the $300 - 800$ *nm* range using data from Buiteveld *et al.* [35]. Water absorption has to be considered for applications using near infrared light. We will not however consider water absorption in our own model since it is specifically developed for applications using the visible spectrum of light where water absorption can be considered negligible.

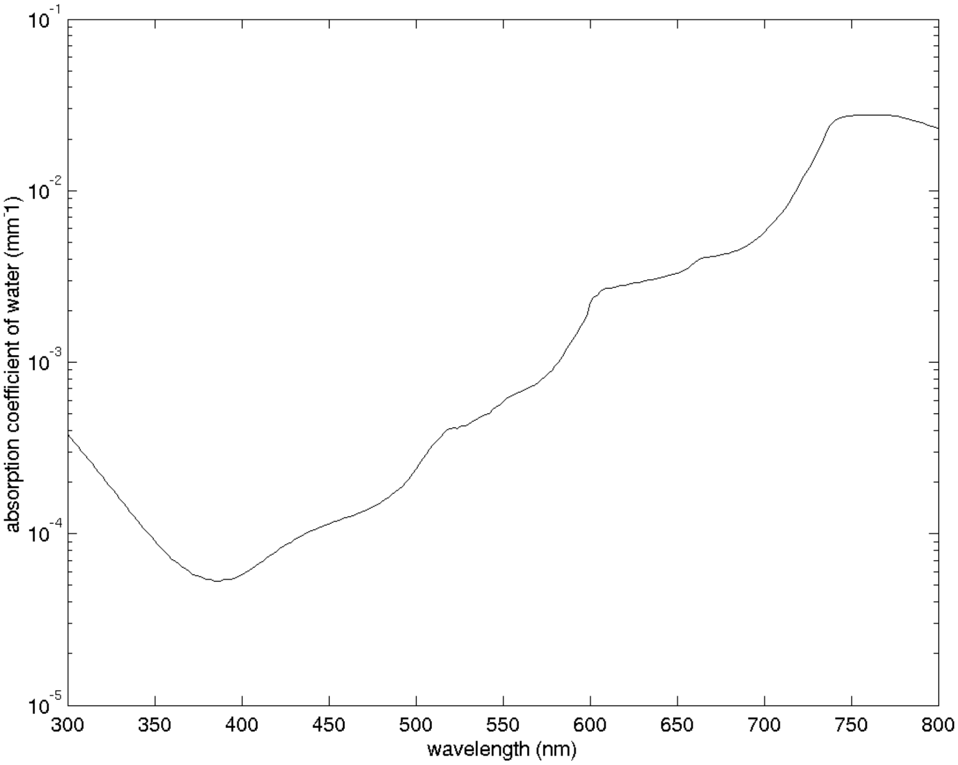

Figure 2.2: Absorption coefficient of water $\mu_{a.water}$ with respect to wavelength λ (data source: Buiteveld *et al.* [35]).

2.1.4 Melanin Spectral Absorption Coefficient

The total absorption of the epidermis is usually dominated by melanin absorption in most individuals. The absorption spectrum of melanin exhibits stronger absorption at shorter wavelengths. Jacques [94] approximates the absorption coefficient of one melanosome by:

$$\mu_{a.melanosome}(\lambda) = (6.6 \times 10^{11})\ (\lambda^{-3.33}) \qquad [cm^{-1}]. \tag{2.3}$$

2.1.5 Epidermis Spectral Absorption Coefficient

The epidermal absorption coefficient $\mu_{a.epidermis}$ combines the baseline skin absorption coefficient $\mu_{a.skinbaseline}$ (Section 2.1.2) and the melanin absorption coefficient $\mu_{a.melanosome}$ (Section 2.1.4) [94]:

$$\mu_{a.epidermis}(\lambda) = (f_{melanosome})(\mu_{a.melanosome})\ +\ (1 - f_{melanosome})(\mu_{a.skinbaseline}) \quad [cm^{-1}]. \tag{2.4}$$

According to Jacques [94], the volume fraction of melanosomes $f_{melanosome}$ varies in skin:

- $\approx 1 - 3\%$ for light skinned Caucasians.
- $\approx 11 - 16\%$ for well-tanned Caucasians and Mediterraneans.
- $\approx 18 - 43\%$ for darkly pigmented Africans.

Using the skin baseline approximation of Saidi [185], we have plotted in Figure 2.3 the absorption coefficient of the epidermis $\mu_{a.epidermis}$ relative to wavelength λ, assuming a volume fraction of melanosomes $f_{melanosome}$ of 6%, corresponding to a light skinned Caucasian.

The absorption spectrum of the epidermis is tightly correlated to the absorption spectrum of eumelanin. The absorption spectrum is decreasing with wavelength, and has maximum absorption in the ultraviolet range. This is no surprise since the role of melanin is to protect the nuclear material of the epidermis mitotic cells against the ultraviolet radiations of the sun.

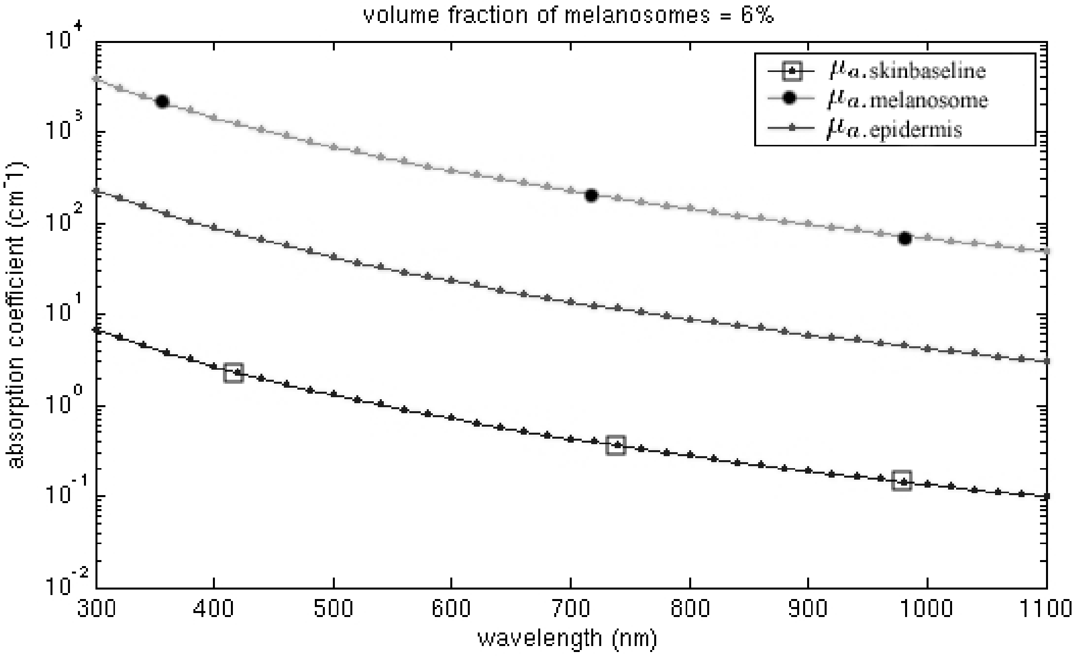

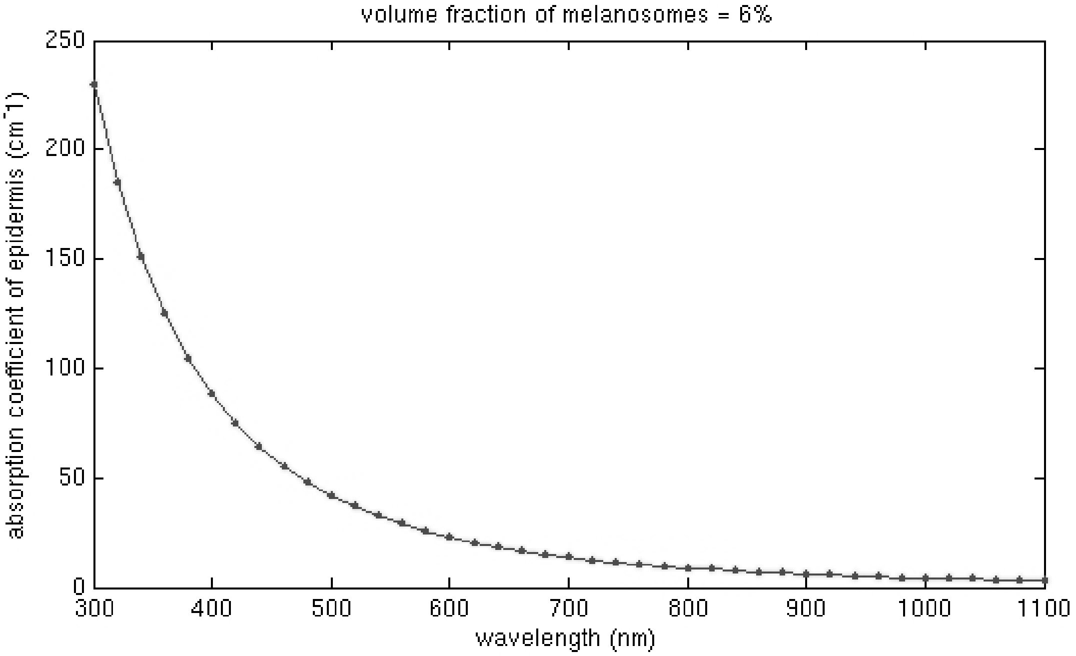

Figure 2.3: Absorption coefficient of epidermis $\mu_{a.epidermis}$ with respect to wavelength λ, with $f_{melanosome} = 6\%$.

2.1.6 Epidermis Spectral Scattering Coefficient

Backward scattering in the epidermis is very weak and was measured by Anderson *et al.* [13] to be only about 5% of the incident radiation in the visible spectrum range. The mean cosine of deflection angle g due to a scattering event varies in the range of 0.7-0.95 for skin tissue and varies with wavelength [94]. Van Gemert *et al.* [218] report that the Henyey-Greenstein phase function fits well the scattering behaviour of the epidermis. They report values of g between 0.71 at 300 nm and 0.78 at 540 nm, varying linearly with wavelength. The reduced scattering coefficient $\mu_{sp.epidermis}$ of the epidermis depends on its scattering coefficient $\mu_{s.epidermis}$ and mean cosine of phase function $g_{epidermis}$ [94]:

$$\mu_{sp.epidermis} = (\mu_{s.epidermis})\ (1\ -\ g_{epidermis}) \quad [cm^{-1}]. \tag{2.5}$$

Since the epidermis is very thin, and because its micro-structure composed of keratin fibres is analogous to the collagen fibres of the dermis, dermal scattering can be used to approximate skin scattering [94].

2.2 The Dermis

The dermis is mostly comprised of collagen fibres (about 70% of the dermis), fatty tissue, proteoglycans, fibroconectin, blood vessels, lymphatic vessels, and nerves. The collagen fibres range from $2\mu m - 15\mu m$ in diameter [127]. In contrast to the epidermis which is almost entirely cellular, the dermis contains few cells, the collagen and elastin of the dermis being proteins [232]. The main functions of the dermis are thermo-regulation and providing the vascular network to supply the avascular epidermis with nutrients. The dermis accounts for more than 90% of the skin mass and for the greatest part of its physical strength. Its thickness varies from about $0.6mm$ to $3.0mm$ or more. The blood vessels that irrigate the skin surface contain hemoglobin pigments that contribute to the overall skin reflectance. When we exercise, more blood is drained at the surface of the skin to act as a cooling mechanism, which explains why the skin colour is redder during intense physical activity. Emotions can also alter skin colour due to increased or decreased blood flow. The dermis is subdivided into two regions, namely the *papillary dermis* and the *reticular dermis*. The collagen, elastin, and ground substances present in the dermis provide the support and elasticity of skin. The dermis also contains immune cells to protect the body from pathogen agents that may pass through the epidermis. Scattering in the dermis is mostly due to the collagen fibres whereas absorption is caused by the different blood pigments. In normal skin, the scattering component can therefore be fixed with the absorption depending on the amount and nature of the blood present.

Papillary Dermis

The papillary dermis is the outermost layer of the dermis and is composed of loose connective tissue. Its structure consists of a fine network of collagen fibres and is not flat; it is intercalated with the epidermis at intervals, being more frequent and deeper where the skin is more likely to undergo abrasive forces. It mostly contains the vascular network that provides thermo-regulation and supplies nutrients to the avascular epidermis. By increasing or decreasing blood flow, heat can either be conserved or dissipated. Arteries that penetrate deep muscles and subcutaneous fat give rise to a deep horizontal plexus located at the interface between the dermis and the hypodermis. From this deep plexus a network of tributaries also irrigate hair follicles and eccrine glands, and ascend vertically to interconnect with a superficial horizontal plexus. The latter lies in the papillary dermis approximately $1-2\ mm$ below the epidermis. From this superficial plexus arborize the dermal papillary loops. Each dermal papilla has a single loop of capillary vessels, one arterial and one venous. A schematic diagram of cutaneous vasculature is shown in Figure 2.4. The papillary dermis also contains the free sensory nerve endings in highly sensitive areas of the body.

Reticular Dermis

The reticular dermis consists of dense irregular connective tissue and contains most of the structures that give skin its strength and elasticity. It also contains glands, hair follicles, blood vessels,

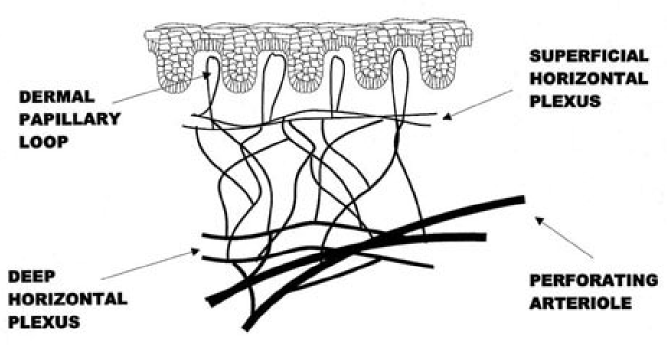

Figure 2.4: Schematic diagram of cutaneous vasculature (from Freinkel and Woodley [65]).

and some sensory nerve endings. The collagen fibres it contains are inelastic and have a tensile strength greater that of steel. They are aggregated into thick bundles which are arranged nearly parallel to the skin surface [127]. The collagen fibres are made with collagen proteins, the most abundant protein in the body forming about 30% of the body dry weight. The reticular dermis also contains elastic fibres that are made with elastin proteins.

2.2.1 Hemoglobin Pigments

The number of blood vessels in the dermis, their dilatation, and the colour of the blood within these vessels have a major influence on skin colour, particularly among Caucasians, since the smaller quantity of eumelanin pigments in the epidermis allows more light to reach the deeper layers of the dermis. There are two arterial plexuses in skin. One lies between the papillary layer and the reticular layer of the dermis and the second lies between the dermis and the hypodermis. There are three plexuses of veins: one between the papillary layer and the reticular layer of the dermis, one between the dermis and the hypodermis, and the third in the middle of the reticular layer of the dermis. The principal pigment in the blood is hemoglobin. It has a normal concentration of $150 g/liter$ in blood and composes 95% of the dry mass of red blood cells. Hemoglobin is itself separated into *oxy-hemoglobin* (HbO_2) when it is bound to oxygen, *deoxy-hemoglobin* (Hb) when it is bound to nothing, and *carboxy-hemoglobin* ($HbCO$) when it is bound to carbon monoxide. All these types of hemoglobin have different spectra of absorption. The absorption coefficient

$\mu_{a.dermis}$ of the dermis depends on a minor baseline skin absorption $\mu_{a.skinbaseline}$ and a dominant hemoglobin absorption $\mu_{a.blood}$ due to the cutaneous blood perfusion. The independent parameters that specify the absorption coefficient $\mu_{a.dermis}$ are the wavelength and the volume fraction of blood f_{blood} in one individual. This produces an average absorption coefficient $\mu_{a.dermis}$. A more rigorous analysis would specify a depth profile for capillaries in the dermis since different wavelengths sample blood at different depths with different efficiencies [94, 218].

2.2.2 Carotene Pigments

Carotene, an orange pigment, contributes to the overall skin colour, but much less than melanin and hemoglobin. It is one of the chromophores of the dermis and it can also be found in the blood. It is an unsaturated hydrocarbon found as a pigment in many plants and vegetables. Its presence in human skin mostly depends on food consumption. The absorption peak of carotene is around 480 nm. However, its overall effect on skin reflectance can be considered negligible [33].

2.2.3 Bilirubin Pigments

Bilirubin is the waste product that results from the breakdown of hemoglobin molecules from worn out red blood cells. Ordinarily, it is excreted from the body as the main component of bile. Bilirubin metabolism begins with the breakdown of red blood cells by phagocytic cells. Red blood cells contain hemoglobin, which is broken down to heme and globin. Heme is converted to bilirubin, which is then carried by albumin in the blood to the liver. Excessive levels of bilirubin stain yellow the fatty tissues in skin; this condition is called jaundice. Normal concentrations of bilirubin vary between $0.3 - 1.9$ mg/dl. Bilirubin is found in blood either bound to albumin or in its soluble form.

2.2.4 Blood Spectral Absorption Coefficient

The major absorbers in blood are oxy-hemoglobin and deoxy-hemoglobin and the total absorption of the dermis is usually dominated by hemoglobin absorption. The absorption spectrum of oxy-hemoglobin exhibits two characteristic absorption bands at 420 nm and in the $545 - 575$ nm

range where it forms a very characteristic 'W' pattern. The absorption spectra of both oxy-hemoglobin and deoxy-hemoglobin tend to exhibit lower absorption with increasing wavelength. The absorption coefficient of whole (45% hematocrit) blood $\mu_{a.blood}$ relative to wavelength λ is plotted in Plate I from obtained data [234].

2.2.5 Dermis Spectral Absorption Coefficient

The dermal absorption coefficient $\mu_{a.dermis}$ combines the baseline skin absorption coefficient $\mu_{a.skinbaseline}$ (Section 2.1.2) and the blood absorption coefficient $\mu_{a.blood}$ (Section 2.2.4). We must also have a measure of how much blood there is in the dermis. The average volume fraction of blood f_{blood} provides an average over the whole body and assumes that blood is uniformly distributed in the skin, which is not the case in reality. A typical value for f_{blood} is 0.2% [94]. In reality the cutaneous blood content is concentrated in a superficial plexus about $100 - 200\mu m$ from the surface and the volume fraction in this region is likely to be about 2-5%, which is a common blood volume fraction in other well-perfused tissues. In other parts of the dermis, the local volume fraction is much lower. On average, however, to an external observer a homogeneous blood distribution with a low f_{blood} and a heterogeneous distribution with a superficially localised high f_{blood} appear roughly equivalent. According to this description, the absorption coefficient $\mu_{a.dermis}$ of the dermis is [94]:

$$\mu_{a.dermis}(\lambda) = (f_{blood})\ (\mu_{a.blood})\ +\ (1\ -\ f_{blood})\ (\mu_{a.skinbaseline}) \qquad [cm^{-1}]. \tag{2.6}$$

Again using the skin baseline approximation of Saidi [185], we have plotted in Plate I the absorption coefficient of the dermis $\mu_{a.dermis}$ relative to wavelength λ, assuming an average volume fraction of blood f_{blood} of 2%.

2.2.6 Dermis Spectral Scattering Coefficient

Anderson *et al.* [13] point out that the dermis scattering coefficient increases with decreasing wavelength, with red light penetrating far deeper than blue. The derivation of the scattering coefficients of the dermis (and as discussed in Section 2.1.6 of the epidermis) are somewhat complicated and the interested reader is referred to some of the original publications [93, 94, 185, 218]. The scattering behaviour of the dermis is accounted for by the combination of Rayleigh and Mie scattering (Section A.11) primarily from collagen fibres. The scattering behaviour is dominated by Rayleigh scattering from small-scale structures at short wavelengths below about 650 nm and is dominated by Mie scattering from fibres at longer wavelengths above 650 nm.

The Mie scattering behaviour in the dermis (and skin) can be mimicked by [94]:

$$\mu_{sp.Mie}(\lambda) = (2 \times 10^{5})\ (\lambda^{-1.5}) \qquad [cm^{-1}]. \tag{2.7}$$

The Rayleigh scattering component observed in the dermis (and skin) [94] is

$$\mu_{sp.Rayleigh}(\lambda) = (2 \times 10^{12})\ (\lambda^{-4}) \qquad [cm^{-1}]. \tag{2.8}$$

The reduced scattering coefficient $\mu_{sp.dermis}$ of skin is a combination of the Mie and Rayleigh scattering terms [94]:

$$\mu_{sp.dermis}(\lambda) = \mu_{sp.Mie}(\lambda) + \mu_{sp.Rayleigh}(\lambda) \qquad [cm^{-1}]. \tag{2.9}$$

We have plotted the reduced scattering coefficient $\mu_{sp.dermis}$ of the dermis relative to wavelength λ in Figure 2.5 using Equation 2.9. Jacques [93, 94] notes that the approximation is very close to measured data.

2.3 Hypodermis

The hypodermis, also called the subcutaneous connective tissue, consists of a *superficial fascia* and a *deep fascia*. The superficial fascia is made out of adipose tissue whereas the deep fascia coats the bones. The hypodermis allows the skin to have relatively free movement over the underlying tissues. The depth of the hypodermis can be up to 3 cm thick on the abdomen.

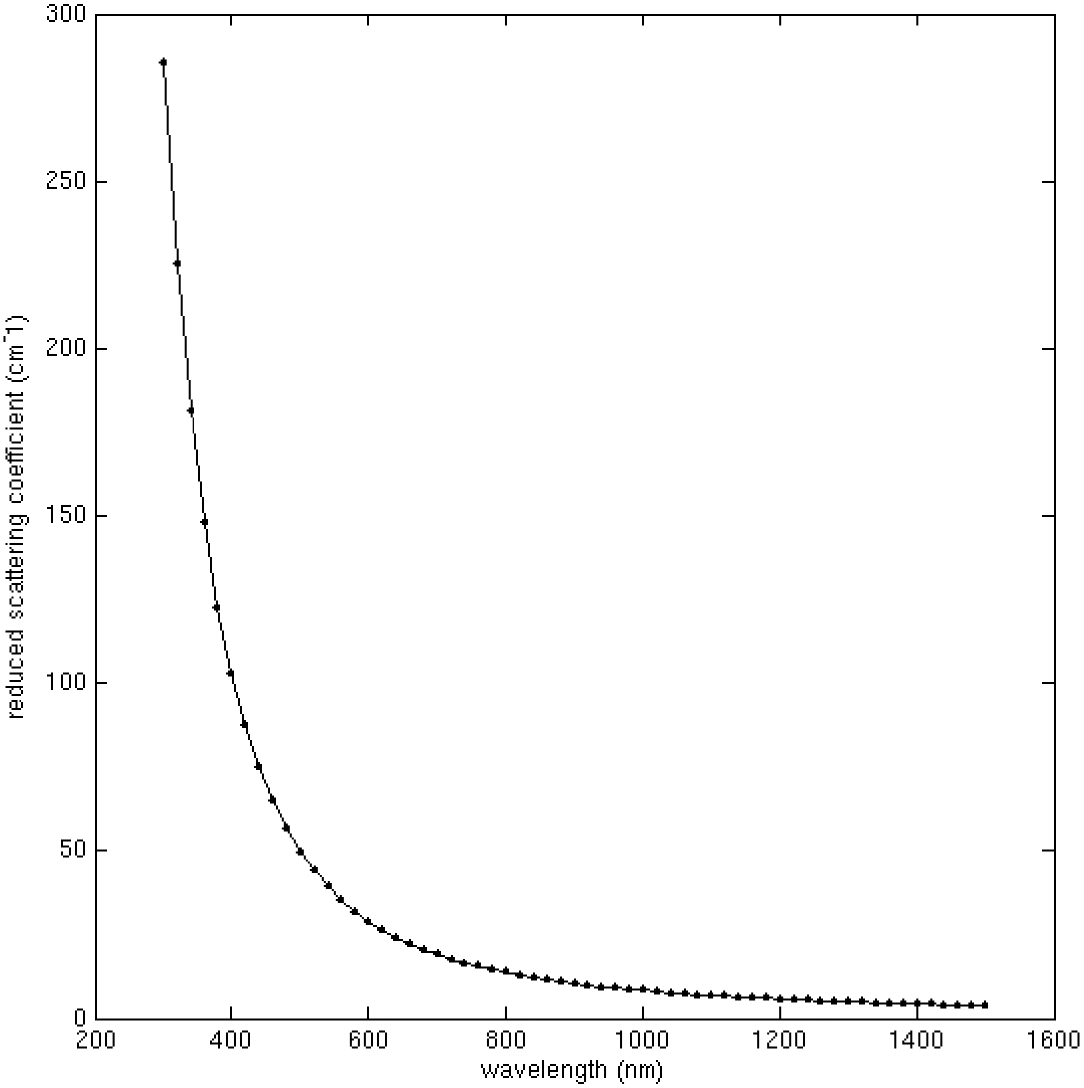

Figure 2.5: Reduced scattering coefficient $\mu_{sp.dermis}$ of the dermis (and of skin) with respect to wavelength λ.

2.4 Hair Follicles

A hair follicle consists of a hair together with a supporting internal and external root sheath. The hair consists of keratinised cellular structures derived from the epithelium of the epidermis. Each follicle has associated with it *arrector pili* muscles that can erect the hair (potentially a vestige of what used to be a thermo-regulation mechanism) and sebaceous glands. The base of the follicle has its root in the papillary dermis, containing capillaries that provide nutrients to the follicle. Hair follicles can be found over the entire body but are concentrated in the facial area and the scalp.

2.5 Sweat Glands

The most common sweat glands are the *eccrine sweat glands*. They are simple coiled tubular glands which open at the skin surface ($\approx 0.4\ mm$ diameter) and have their secretory component located in the dermis. Their excretory ducts ($\approx$ 2.5 million) spiral upwards and are widely distributed at the skin surface. They produce a watery secretion used for cooling the skin surface. Eccrine glands are denser in the axillae (arm pits), palms, soles, and forehead.

The other sweat glands are the *apocrine sweat glands*. They originate from the epidermis and are associated with hair follicles. They are also larger glands than the eccrine sweat glands. They are found in the axillae, perineum (pelvic area), and areolae (breasts), and are a phylogenetic remnant of the mammalian sexual scent gland.

2.6 Sebaceous Glands

Sebaceous glands produce a lipid secretion called sebum. Usually, sebaceous glands are attached to hair follicles, but they sometimes open directly at the skin surface as in the case of the lips for example. Sebaceous glands are found all over the body ($100/cm^2$) with exception of the palms of the hands and the soles of the feet. They are especially prominent with the hair follicles of the face ($400 - 900/cm^2$), scalp, chest, and back. The sebum secretion is under the control of testosterone and androgen hormones, and its production starts at puberty. Excess of sebum secretion is a cause of acne. The function of sebaceous glands remains unknown, although some have suggested that it might have antibacterial and antifungal properties along with helping to prevent water loss.

2.7 In-vivo Skin Reflectance Measurements

Skin reflectance data can be very precious for both computer vision and computer graphics communities. Such data lead to efficient models for skin recognition, simulation, and rendering. Numerous other applications also abound in medical imagery and dermatology, cosmetology, image display and reproduction, etc. The medical community has done extensive measurements of skin reflectance. However, most of this work is either laser-based or focused on the infrared part of the spectrum.

Angelopoulou *et al.* [14, 15, 16, 17, 18] at the GRASP Laboratory of the University of Pennsylvania have set up a BRDF measurement facility in order to obtain skin spectral reflectance data. The experimental setup is described in a technical report [14]. Some of their results are shown in Plates II and III. All measurements were done with a $0°$ angle of incidence and a $4°$ angle of reflectance on the back and palm of the hand of eight volunteers.

Note the relationship between the spectral skin reflectance plots and the spectral absorption and scattering plots of the epidermis and dermis shown previously. The increase of general skin reflectance with wavelength is explained by the fact that both melanin and hemoglobin absorptions decrease with wavelength. The characteristic 'W' pattern in the skin reflectance spectrum between $545 - 575\ nm$ is directly related to the absorption spectrum of oxy-hemoglobin. Finally, this 'W' pattern is much less observable among individuals with higher quantities of eumelanin pigments (Africans and Indians) since more light is absorbed in the epidermis, allowing a much smaller percentage of the incident illumination to reach the vasculature of the dermis. The data gathered by Angelopoulou *et al.* clearly demonstrate that skin reflectance varies among individuals. Nevertheless, the analysis that we presented in this chapter based on Jacques [94] is a good starting point for understanding the issues in designing a generic skin reflectance model. Angelopoulou *et al.* also note that reflectance studies of dead skin [33] show very different results from their in-vivo data. The reflectance spectrum of post-mortem skin is relatively flat. This has the important implication that BRDF measurements of skin acquired from dead skin samples, as is the case with the CUReT database [2, 50], cannot be used for photo-realistic skin rendering (unless of course the goal is to render dead people!).

In-vivo BRDF skin reflectance measurements were also done by Marschner *et al.* [136, 140, 139] with an inverse rendering approach. All measurements were performed on a sample of skin located on the subject's forehead. However, they assume that the BRDF is constant over the area of skin they measure, sacrificing spatially-dependent properties in exchange for a more complete angular coverage. Another problem with the technique is that the camera acquires information from micro-scale geometry that is not present in the geometric model used. Their results are shown in Figure 2.6, demonstrating coverage and incidence-plane slices for one of their datasets [139]. The overall qualitative conclusion is that their BRDF is almost Lambertian at small incidence angles, but exhibits strong forward scattering at higher angles of incidence.

We performed our own measurements of skin reflectance using a spectrophotometer and show the results in Section 4.1. Our data are in accordance with the data obtained by Angelopoulou et al. [14] and Imai et al. [88], among others.

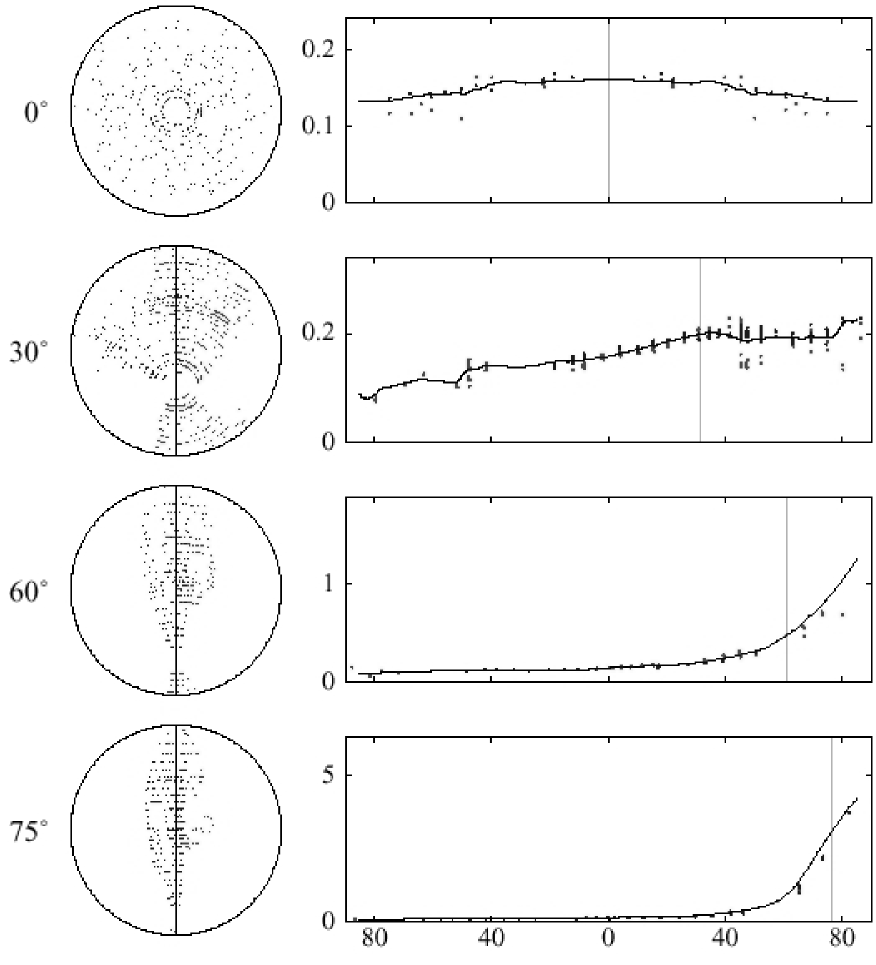

Figure 2.6: Skin reflectance from a sample of the forehead. Left column: sample coverage; right column: raw data and local polynomial fit (from Marschner *et al.* [139]).

Chapter 3

A Survey of Skin Rendering Techniques

Skin rendering techniques can be initially classified into reflectance models and image-based rendering techniques. Several skin reflectance models have been developed in different fields such as computer graphics, computer vision, and bioengineering. This is no surprise since as previously argued, skin rendering is an important problem. Potential applications for skin reflectance models include photorealistic skin rendering, skin colour detection, skin colour reproduction, and detection of skin diseases in-vivo. Clearly, applications abound and models are usually tailored to them. We further classify skin reflectance models as analytical or numerical.

Analytic skin reflectance models make assumptions in order to derive an analytic solution to light transport in skin. Those assumptions are justified by the applications. Some models describe skin as a layered structure and use Kubelka-Munk-like optical transport models. Other models use a diffusion approximation. The diffusion approximation is not as biologically accurate for skin as other materials since it assumes an homogeneous media, whereas skin clearly has a layered structure. Analytic models are useful for modelling because they allow intuitive model variations to map directly into variations in colour. The possibility of inverting the model, i.e., going from reflectance to skin parameters, has obvious implications in medical applications for example. Finally, analytic models are much more computationally efficient than numerical models. Most of the time they can be transformed into numerical models by combining them with an adequate scattering model in order to produce Bidirectional Reflectance Distribution Functions (BRDFs, see Appendix A) or Bidirectional Surface Scattering Reflectance Distribution Functions (BSSRDFs, see Appendix A) if need be. The diffusion approximation has been used for example by Jensen *et al.* [96] in a BSSRDF framework with great success and has won the authors a technical achievement award from the Academy of Motion Picture Arts and Sciences. Clearly, the choice of a skin reflectance model depends on the application, on the resources available, and on the quality of the result required. Some analytic models are presented in Section 3.1. Our own model of skin reflectance, described in Section 4.1, fits this category.

Numerical models solve the full light transport in skin tissue. They can use a very elaborate and biologically accurate description of the skin's anatomy to produce a very good approximation of its reflectance. In this case the quality of the approximation depends directly on the quality of the skin anatomy model. The numerical methods can be used both in a BRDF or BSSRDF framework, although the full multiple scattering simulation within a BSSRDF framework might be computationally very prohibitive. Monte Carlo simulation is often the tool of choice to solve the light transport problem. For computer graphics rendering, this technique suffers however from its high computational complexity and hinders the modelling process since it precludes the intuitive connection of parameters to physiology. Those models are also not easily invertible. Moreover, the sampling nature of Monte Carlo methods results in noise, which is not satisfactory for skin's smooth appearance. We present some numerical models in Section 3.2.

Most of the image-based techniques and the analytic models, like our own model (Section 4.1), can easily be made interactive or real-time. Full light transport simulations are however not well suited for interactive rendering. Recent works on real-time reflectance models of subsurface scattering use the diffusion approximation in a BSSRDF framework. They are discussed in Section 3.3.

Image-based approaches to skin rendering are discussed in Section 3.4. Effects such as self-shadowing, inter-reflections, and subsurface scattering are quite difficult to simulate for a specific individual using the skin models discussed previously. The acquisition of skin model parameters for a particular individual is also a non-trivial problem. Image-based techniques can be useful in some applications and produce good visual results at reasonable costs. Those techniques suffer however from the usual problems associated with image-based rendering, such as high memory requirements, incident illumination captured in the images, and the difficulty of modifying the results.

Level of detail issues are important for reflectance models and are discussed in Sections 3.5 and 3.6. We finally discuss briefly wrinkle models in Section 3.6 and an asperity scattering model in Section 3.7 that is used to simulate the scattering of light on small hairs at the skin's surface.

3.1 Analytical Skin Reflectance Models

Stam [199] presents a reflection model for a skin layer bounded by two rough surfaces. This model is used in the Maya Skin Shader [224]. There are two main differences between the Hanrahan-Krueger model [74] and the Stam model. The former assumes that layer interfaces are perfectly smooth and multiple scattering is accounted for by a Monte Carlo simulation. The latter does not assume smooth layer boundaries and derives an analytical approximation to multiple scattering using a discrete ordinate approximation of the radiative transfer equation. Also, Stam's model has only one layer of skin whereas a full simulation like the one performed in Hanrahan-Krueger allows multiple layers of different properties. Both models are used in a BRDF framework. However, Stam's model does not suffer from the traditional Monte Carlo simulations problems - it is much faster, consumes less memory, and does not suffer from noisy artifacts.

Cotton and Claridge [40, 46] and Claridge and Preece [41] use a predictive model based on the Kubelka-Munk theory (Section A.12). Their model predicts that all skin colours lie on a simple curved surface patch within a three-dimensional colour space bounded by two physiologically meaningful axes, one corresponding to the amount of melanin within the epidermis and the other to the amount of blood within the dermis. Their model assumes that scattering is negligible and that Beer's law (see Section A.9) can be used to describe the attenuation of light in the epidermis. All light not absorbed by melanin in the epidermis can be considered to pass into the dermis. The dermis has a high scattering coefficient and therefore cannot be modelled with Beer's law. It is divided into two layers with different scattering properties: the papillary dermis and the reticular dermis (Section 2.2). Scattering varies in an homogeneous material with the size and structure of the particles. The large collagen structures of the reticular dermis are modelled using Mie scattering (highly forward scattering) whereas the smaller collagen fibres present in the papillary dermis are modelled with Rayleigh scattering. The re-emitted light from the reticular layer is thus considered negligible due to the highly forward-directed Mie scattering. Their target application aims to help clinicians in performing early diagnosis of malignant melanoma and therefore restricts its calculations to RGB values and does not concern itself with how to render the results.

The basic diffusion approximation is an analytic technique and is therefore described in this section. Most works using the diffusion approximation do it however in a numerical simulation context. Diffusion simulations of light propagation in biological tissues were performed in the medical and biomedical communities before being introduced to computer graphics [57, 108, 110, 221]. Diffusion theory was considered in computer graphics [114, 197]. The diffusion approximation can be quite helpful to counteract the high cost of Monte Carlo methods used when performing path sampling for subsurface scattering. This is especially true when the albedo is high, e.g., when the material is highly scattering. It has been shown that this is the case for skin, as discussed in the previous chapter. Often, several hundred scattering events can occur before light exits the skin surface.

Unlike previous work that only used BRDF-based models for subsurface scattering, Jensen *et al.* [96, 97] use the complete BSSRDF along with a diffusion approximation to model subsurface scattering. This allows them to simulate effects that BRDF models cannot capture, such as colour bleeding within materials and diffusion of light across shadow boundaries and silhouettes. An analogy can certainly be made between BRDF versus BSSRDF and local versus global illumination. In this work, only materials with high albedos were considered, where multiple scattering events account for a large portion of diffuse reflectance. The model presented combines the exact solution for single scattering with a dipole point source diffusion approximation to account for multiple scattering. As some authors have suggested though, considering the single scattering term in that context is probably superfluous since the initial assumption of the diffusion approximation states that multiple scattering largely dominates the diffuse reflectance.

Jensen *et al.* note that light distribution in highly scattering media tends to become isotropic since each scattering event blurs the light. This is true even when the initial light source distribution and the phase function are highly anisotropic. Diffusion theory can provide a good approximation for multiple scattering in highly scattering medium without having to resort on costly Monte Carlo simulations.

The diffusion equation has a simple solution in the case of a single isotropic point light source in an infinite medium [97]:

$$\phi(x) = \frac{\Phi}{4\pi D} \, \frac{e^{-\sigma_{tr} r(x)}}{r(x)}, \tag{3.1}$$

where

$\phi(x)$: radiant flux,

Φ : power of point light source,

D : diffusion constant $= \frac{1}{3\sigma_t'}$,

σ_a : absorption coefficient,

g : mean cosine of the phase function,

σ_t' : reduced extinction coefficient $= \sigma_s' + \sigma_a$,

σ_s' : reduced scattering coefficient $= \sigma_s \ (1 - g)$,

$r(x)$: distance to the point source, and

σ_{tr} : effective transport coefficient $= \sqrt{3\sigma_a\sigma_t'}$.

A more accurate approximation is the dipole diffusion approximation. In this model, the volumetric source distribution is modelled using two point sources. The first one, the positive real light source, is located at distance z_r beneath the surface. The second one, the negative virtual light source, is located above the surface at a distance $z_v = z_r + 4AD$. This model is shown in Figure 3.1.

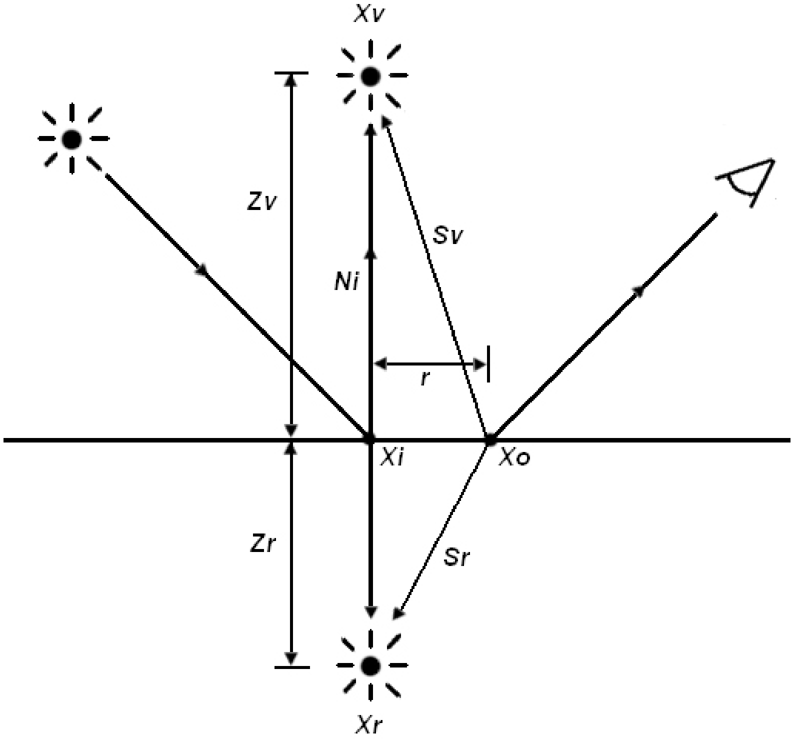

Figure 3.1: Dipole diffusion approximation.

The diffuse reflectance at point x_o due to illumination at point x_i is

$$R_d(x_i, x_o) = \frac{\alpha'}{4\pi}\left(z_r(1 \ + \ \sigma s_r)\frac{e^{-\sigma s_r}}{s_r^3} \ + \ z_v(1 \ + \ \sigma s_v)\frac{e^{-\sigma s_v}}{s_v^3}\right), \tag{3.2}$$

where

$z_r = \frac{1}{\sigma_t'}$ and $z_v = z_r + 4AD$,

$s_r = ||x_r - x_o||$, with $x_r = x_i - z_r \ \cdot \ N_i$,

$s_v = ||x_v - x_o||$, with $x_v = x_i + z_v \ \cdot \ N_i$,

$A = \frac{1 \ + \ F_{dr}}{1 \ - \ F_{dr}}$,

$F_{dr} = -\frac{1.440}{\eta^2} \ + \ \frac{0.710}{\eta} \ + \ 0.668 \ + \ 0.0636\eta$,

$D = \frac{1}{3\sigma_t'}$ and $\sigma = \sqrt{3\sigma_a\sigma_t'}$,

$\sigma_t' = \sigma_a + \sigma_s'$ and $\alpha' = \sigma_s'/\sigma_t'$,

σ_s' : reduced scattering coefficient

σ_a : absorption coefficient, and

η : relative refraction index.

The diffusion approximation has been shown to be accurate when $\frac{\sigma_a}{\sigma_a \ + \ \sigma_s} \ll 1 \ - \ g^2$ [66]. The complete multiple scattering term takes into account the Fresnel reflection for both incoming and exiting radiances [97]:

$$S_d(x_i, \omega_i; x_o, \omega_o) = \frac{1}{\pi} \ F_t(\eta, \omega_i) \ R_d(x_i, x_o) \ F_t(\eta, \omega_o), \tag{3.3}$$

where

η : relative refraction index, and

$F_t(\eta, \omega)$: Fresnel transmittance factor.

The BSSRDF is very costly to compute since we have to sample the incident flux on the surface, which is more costly than a BRDF. If area or volumetric light sources are used, sampling has to be performed at both the light and the translucent object surface. Jensen and Buhler [96] present a technique to speed up the computation for shading translucent objects. The acceleration is achieved by decoupling the computation of irradiance at the surface from the evaluation of scattering inside the material in a two-pass algorithm. The first pass computes the irradiance at selected points on the object's surface. The points are uniformly generated on the mesh surface using Turk's point repulsion algorithm [217]. The maximum distance between the points is set to be the mean-free path $l_u = \frac{1}{\sigma_a + \sigma_s}$ to avoid low-frequency noise in the reconstruction of the diffusion approximation. Each point stores its location, its associated area, and its irradiance estimate.

The second pass evaluates the dipole diffusion approximation using the pre-computed irradiance samples stored in an octree data structure. The octree clusters distant samples together to make the computation fast. The diffusion approximation has an exponential fall-off so that the octree structure proves to be efficient. An error criterion has to be specified to select the node in the octree; in this case the criteria to subdivide a voxel is based on an approximation of the maximum solid angle spanned by the irradiance points in the voxel. For further efficiency, the authors allow up to eight irradiance samples in a leaf node. Finally, note that this data structure speeds up the irradiance gathering at the surface for each shaded point but needs to be recomputed every time the illumination changes with respect to the translucent object. Real-time techniques for subsurface scattering are discussed in Section 3.3.

3.2 Numerical Skin Reflectance Models

Subsurface scattering of light in skin tissues is an important element to model in order to provide accurate skin reflectance models. In Plate IV, we can see that more light enters in the skin in the first image because Fresnel reflection is low due to the light source being perpendicular to the surface. The back-scattered light gives a reddish tint to the face because, as described in Chapter 2, skin absorbs predominantly the lower frequencies of the incoming light. In the second image, the light source is grazing the surface and surface reflection predominates over body reflection. The face is much whiter (the colour of the illuminant). Note also that the skin

Component	$\sigma_a(mm^{-1})$	$\sigma_s(mm^{-1})$	$d(mm)$	g	η
Epidermis	3.8	50.0	0.001-0.15	0.79	1.37-1.5
Dermis	0.3	21.7	1.0-4.0	0.81	1.37-1.5
Pigment	-	-	-	0.79	1.37-1.5
Blood	32.6	0.96	-	0.0	1.37-1.5

Table 3.1: Optical properties of skin used by Hanrahan and Krueger [74].

micro-structure is much more distinguishable in the shadow boundary where the light rays graze the surface. In this case, a texture map would not correctly account for surface variation as in the first image. Micro-structure is less distinguishable in the first image since subsurface scattering blurs the effect of small geometric details on the surface of the skin.

Commercial skin reflectance models include those of Industrial Light + Magic [83] and Pixar [209]. Those models are usually qualitative models where the focus is on the modelling interface rather than on the biological plausibility of the model. Approximations are often made in order to accelerate rendering times for production.

Hanrahan and Krueger [74] perform the full multiple scattering simulation using a Monte Carlo numerical integration method. They present a model for subsurface scattering in layered surfaces in terms of one-dimensional linear transport theory. The optical properties of each layer are the index of refraction η, the absorption cross section σ_a, the scattering cross section σ_s, the layer depth d, the scattering phase function $p(\cos j)$, and the mean cosine of the phase function g. The parameter values they use to describe the optical properties of skin are shown in Table 3.1.

Chandrasekhar gave an analytic solution to the integral transport equation assuming a single scattering event [38]. Solution of the light transport integral assuming multiple scattering events is performed using a Neumann series. When the albedo W is high (scattering $\gg$ absorption), the first order term is only a small percentage of the total reflectance. When W is small (greater absorption), a few low-order terms accurately approximate the reflectance, e.g., single scattering dominates the overall diffuse reflectance. They assume that the boundaries of the different layers are all flat, which is not always the case in reality, especially with the outermost layer of the epidermis (the horny layer) and the boundary between the epidermis and the dermis. Note that the parameters they used are not wavelength dependent and not biologically accurate. They also consider only one level of inter-reflection and miss the effect of multiple internal reflections before light leaves a layer. Finally, they use a BRDF model and do not consider the more general BSSRDF when performing rendering since it would be extremely prohibitive within a Monte Carlo framework.

Pharr and Hanrahan [174] present a non-linear integral scattering equation that describes the overall scattering behaviour of an object or volume accounting for all the scattering events that happen inside of it. This technique mitigates some of the shortcomings of Hanrahan and Krueger [74] and provides a simpler framework by working directly with scattering equations and mechanisms to add them together. Like Hanrahan and Krueger [74], they use a BRDF framework.

Ng and Li [159] perform a Monte Carlo simulation similar to Hanrahan and Krueger [74] but they use an extra third layer in their model - an outermost sebum layer which is set to have a refractive index of 1.5. The second layer is the epidermis and is set to have a refractive index of 1.3. The dermis is the last layer. Optical properties of skin are loosely based on Jacques [94] and are therefore more biologically accurate than those used by Hanrahan and Krueger. They compare their simulated BRDF to the CUReT database [2, 50] skin BRDF sample and claim good agreement of the data. This is somewhat surprising since the CUReT sample comes from a cadaver.

Many other Monte Carlo simulations of optical radiation propagation in biological tissues were performed in the medical and biomedical communities long before models were proposed in computer graphics [29, 61, 107, 145, 147, 148, 168, 180, 222, 231, 241]. Most of those skin anatomy models can be applied directly in computer graphics. We will now describe a model that goes further in its biological description of skin tissues than all models previously discussed. Meglinski and Matcher [147, 148] simulate the diffuse reflectance spectra of skin using a biological model that takes into account the spatial distribution of blood vessels, water, melanin content, and geometrical properties of skin histological structure. They use a stochastic numerical Monte Carlo simulation to model optical radiation propagation in tissue. Their computational model of skin is similar in spirit to Hanrahan and Krueger [74] but is much more accurate in its biological description and computes spectral reflectances. The model is divided into seven layers, namely the

1. stratum corneum ($20\mu m$),
2. living epidermis ($80\mu m$),
3. papillary dermis ($150\mu m$),
4. upper blood net dermis ($80\mu m$),
5. reticular dermis ($1500\mu m$),
6. deep blood net dermis ($100\mu m$), and
7. subcutaneous fat ($6000\mu m$).

Taking into account thickness variations over the body and differences in structure, their model represents the interfaces between the skin layers as quasi-random periodic surfaces [145, 146, 147]:

$$\begin{aligned} B_k(x,y) \;&=\; Z_{0k}(x_0,y_0) \;+\; (A_{kx}\sin(\omega_{kx}x \;+\; \phi_{kx}) \;+\; a_{kx}\sin(\omega'_{ky}y \;+\; \phi'_{kx})) \\ &\quad\; (A_{ky}\sin(\omega_{ky}y \;+\; \phi ky) \;+\; a_{ky}\sin(\omega'_{ky}y \;+\; \phi'_{ky})), \end{aligned} \tag{3.4}$$

where

$B_k(x,y)$: depth of the kth layer at the point (x,y),

$Z_{0k}(x_0,y_0)$: mean depth of the boundary,

$A_{kx}, A_{ky}, a_{kx}, a_{ky}$: amplitude coefficients in the x and y directions,

$\omega_{kx}, \omega_{ky}, \omega'_{kx}, \omega'_{ky}$: scale lengths of the roughness in the x and y directions,

$\phi_{kx}, \phi_{ky}, \phi'_{kx}, \phi'_{ky}$: arbitrary phase offsets in the x and y directions.

We show the values they use to characterise the different interfaces in Table 3.2. Meglinski and Matcher claim that these values produce layer boundaries that are comparable to the observed structure of real skin. As discussed in Section 2.2.1, blood content in tissues varies both in amount and distribution. Most of the blood in the dermis is concentrated in the superficial and deep plexuses within a layer of $50-100$ μm and with a concentration of $2-10\%$. The Meglinski-Matcher

k	Boundary between layers	A_{kx}, A_{ky} (μm)	$(\frac{\pi}{\omega})k_x$ (μm)	$(\frac{\pi}{\omega})k_y$ (μm)	Z_{0k} (μm)
0	Air-stratum corneum (skin surface)	2	100	150	0
1	Stratum corneum-living epidermis	2.5	80	80	20
2	Living epidermis-papillary dermis	20	50	45	100
3	Papillary dermis-upper blood net dermis	2	20	40	250
4	Upper blood net dermis-dermis	2	20	50	330
5	Dermis-deep blood net dermis	2	20	50	1830
6	Deep blood net dermis-subcutaneous fat	5	20	50	1910
7	Subcutaneous fat-other tissues	5	25	30	8000

Table 3.2: Parameter values used to characterise skin layer boundaries by Meglinski and Matcher [147].

k	Name of layer	C_{blood}	C_{H_2O}	μ_s (mm^{-1})	g	η
1	Stratum corneum	0	0.05	100	0.86	1.5
2	Living epidermis	0	0.2	45	0.8	1.34
3	Papillary dermis	0.04	0.5	30	0.9	1.4
4	Upper blood net dermis	0.3	0.6	35	0.95	1.39
5	Reticular dermis	0.04	0.7	25	0.8	1.4
6	Deep blood net dermis	0.1	0.7	30	0.95	1.38
7	Subcutaneous fat	0.05	0.7	5	0.75	1.44

Table 3.3: Optical properties of skin used by Meglinski and Matcher [147].

model tries to approximate this spatial distribution of blood content by dividing the dermis into four layers. The optical parameters of all the layers have been collected from numerous literature sources. The parameters used in their Monte Carlo simulations are displayed in Table 3.3. The spectral absorption coefficients for oxy- and deoxy-hemoglobin, melanin, and the skin baseline are similar to the ones presented in Chapter 2. They are shown in Figure 3.2.

Epidermal Layers

Epidermal layers contain melanin but no blood. The spectral absorption coefficients for the epidermis skin layers ($k = [1-2]$) are computed with the following formulas [147]:

$$\mu_a^{k=1}(\lambda) = ((0.1 - 0.3 \times 10^{-4}\lambda) + 0.125\,\mu_a^{(0)}(\lambda))\,(1 - C_{H_2O}) + C_{H_2O}\,\mu_a^{H_2O}(\lambda), \quad (3.5)$$

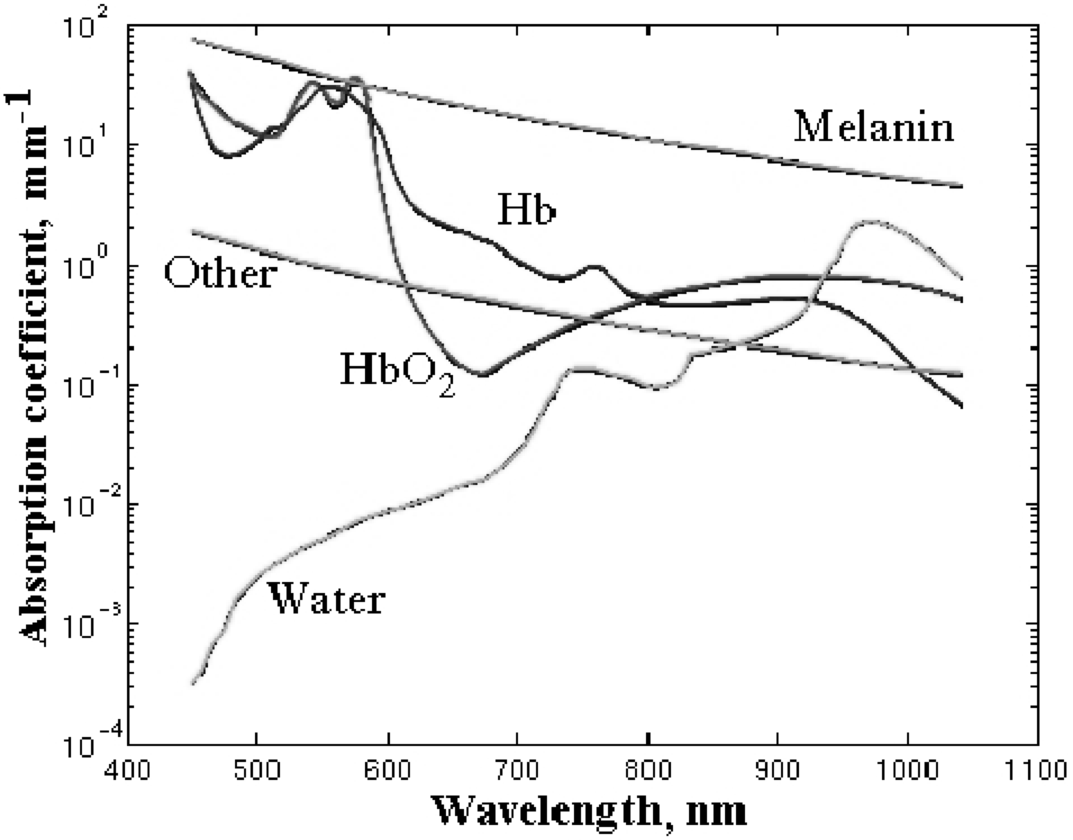

Figure 3.2: Absorption coefficients of oxy- and deoxy-hemoglobin, melanin, and water used by Meglinski and Matcher [147].

and

$$\begin{aligned} \mu_a^{k=2}(\lambda) &= (C_{melanin}\ \mu_a^{melanin}(\lambda) + (1 - C_{melanin})\ \mu_a^{(0)}(\lambda))\ (1 - C_{H_2O}) \\ &\quad + C_{H_2O}\ \mu_a^{H_2O}(\lambda), \end{aligned} \tag{3.6}$$

where

$\mu_a^{(0)}(\lambda)$: skin baseline spectral absorption coefficient (Section 2.1.2),

$\mu_a^{melanin}(\lambda)$: melanin spectral absorption coefficient (Section 2.1.4),

$\mu_a^{H_2O}(\lambda)$: water spectral absorption coefficient (Section 2.1.3),

$C_{melanin}$: volume fraction of melanin in layer (Section 2.1.5), and

C_{H_2O} : volume fraction of water in layer (see Table 3.3).

Dermal Layers

Dermal layers contain blood but no melanin. The spectral absorption coefficient for the dermis skin layers ($k = [3 - 7]$) is computed using the following formula [147]:

$$\begin{aligned} \mu_a^{k=3-7}(\lambda) &= (1 - S)\gamma\ C_{blood}\ \mu_a^{Hb}(\lambda) + S\gamma\ C_{blood}\ \mu_a^{HbO_2}(\lambda) \\ &\quad + (1 - \gamma C_{blood})\ C_{H_2O}\ \mu_a^{H_2O}(\lambda) \\ &\quad + (1 - \gamma C_{blood})(1 - C_{H_2O})\ \mu_a^{(0)}(\lambda), \end{aligned} \tag{3.7}$$

where

$\mu_a^{(0)}(\lambda)$: skin baseline spectral absorption coefficient (Section 2.1.2),

$\mu_a^{HbO_2}(\lambda)$: oxy-hemoglobin spectral absorption coefficient (Section 2.2.4),

$\mu_a^{Hb}(\lambda)$: deoxy-hemoglobin spectral absorption coefficient (Section 2.2.4),

$\mu_a^{H_2O}(\lambda)$: water spectral absorption coefficient (Section 2.1.3,)

C_{blood} : volume fraction of blood in layer (see Table 3.3),

C_{H_2O} : volume fraction of water in layer (see Table 3.3),

S : blood oxygen saturation = 0.6,

γ : volume fraction of hemoglobin in blood in layer = $F_{Hb}F_{RBC}H_t$,

F_{Hb} : volume fraction of hemoglobin in an erythrocyte = 0.25,

F_{RBC} : volume fraction of erythrocytes in total volume of all blood cells = 0.99, and

H_t : blood hematocrit = 0.45.

We have plotted the spectral absorption coefficient of each layer given by the Meglinski-Matcher model in Plates V and VI against the epidermis and dermis spectral absorption coefficients that were presented in Chapter 2. The Meglinski-Matcher model is probably one of the most comprehensible computational models of skin. It allows spatially varying distribution of tissue absorbers (oxy-hemoglobin, deoxy-hemoglobin, melanin, and water) within seven layers of distinct properties. Note however that they do not take into account the wavelength dependence of scattering coefficients. To our knowledge, this model was not implemented in the computer graphics community and it is not clear what could be gained in practice with this model assuming a photorealistic skin rendering goal. We believe that it would have to be implemented in a BSSRDF framework to produce important effects at a smaller scale, such as colour bleeding and shadow softening. The Meglinski-Matcher model is definitely useful in certain specific applications, such as medical simulations. However, due to its high tradeoff of computational cost versus impact on quality of rendering, the model does not seem practical for general purpose computer graphics. We aim at developing a simpler and more efficient model that will provide artists with a more intuitive relationship between model parameters and results.

3.3 Real-time Skin Reflectance Models

Accurate simulations of volume or subsurface light transport are computationally expensive and not well suited for interactive or real-time rendering applications. Several works emerged after Jensen *et al.* 's paper on subsurface light transport [96] with the goal of performing subsurface scattering in real-time. The vast majority of those works use the dipole diffusion approximation along with other hardware techniques in order to allow an interactive or real-time implementation. Early attempts to simulate subsurface scattering in real-time were based on "hacks" that computed the thickness of an object along a ray [73, 82, 141]. Recent works achieve more physically plausible real-time subsurface scattering.

Kniss *et al.* [113] describe a simple and qualitative interactive volume shading model that captures volumetric light attenuation effects to produce volumetric shadows and the qualitative appearance of subsurface scattering. This model is based on empirical observations of appearance of volumetric materials and does not require material optical properties to be specified in terms of scattering and absorption coefficients. The model can capture effects such as colour bleeding and diffusion of light across shadow boundaries. Multiple scattering produces indirect lighting whose qualitative effect is diffusion of light through the volume. To model this diffusion process, they use a Gaussian blur that averages the incoming light within a cone with an apex angle θ in the direction of the light. A simple spectral light attenuation term is used and the user-specified parameter consists of a transport colour, which is the colour the indirect light will become as it is attenuated by the material. Three buffers are required to implement the technique in hardware: two for the attenuation of light in the light direction and one for the accumulation of light for the observer. Two passes are required to perform the blurring and the number of samples used for the computation of the indirect light is limited by the number of texture units.

Lensch *et al.* [126] propose an interactive method for rendering translucent objects with arbitrary viewpoint or illumination. Their approach to model the blurring of incident illumination is to factor the light impulse response on the surface of a translucent object into a low frequency global component and a high frequency local component. The first component, the *smooth global part*, models subsurface scattering at large distances. The second component, the *detailed local part*, models subsurface scattering at small scattering distances. The technique goes as follows:

1. Incident illumination is computed and projected into a texture atlas.
2. The *smooth global part* is computed by projecting the illumination to the mesh vertices and multiplying the vertex irradiance vector with a vertex-to-vertex throughput factor matrix [126].

3. The *detailed local part* is computed by filtering the incident illumination map with spatially varying 7 × 7 texel-to-texel filter kernels.
4. The global and local parts are merged together.

The global and local responses cannot simply be blended together to obtain the correct result. The influence of the low-frequency part must be reduced at small scattering distances. Smooth blending must be ensured at the boundary where the influence of the local response ends. The pre-processing step generates the texture atlas and calculates the local and global distributions for light reaching an object at a single point. The texture atlas is composed of several triangle clusters that have similar orientations within some threshold. These clusters are packed into a square texture of predefined resolution.

Hao *et al.* [75] exploit the locality of the diffusion approximation to create a BSSRDF approximation within a local illumination context. The complexity of their algorithm is $O(n)$ where n is the number of vertices in a polygonal mesh. Subsurface scattering is relatively local due to its exponential falloff and their empirical model aims at mimicking multiple scattering reflection and transmission. They divide the local illumination process into two stages: a traditional local lighting stage and a scatter-bleeding stage. In a pre-processing phase, the set of all neighbours $N(x_o)$ of vertex x_o are computed. The neighbourhood of a vertex x_o is defined to include all vertices x_i that lie within the effective scattering range from x_o. This range will vary according to the relative refraction index η, the absorption coefficient σ_a, and the scattering coefficient σ_s. We can therefore eliminate all vertices whose impact is too small on the irradiance due to subsurface scattering at x_o. The total outgoing radiance at a point is computed by an integral over all incoming light directions and surface area and is expressed as a summation over all vertices in the neighbourhood of x_o. They pre-compute the integrals for a set of uniformly distributed directional light sources. Quaternion-based vector interpolation is used at run-time to evaluate outgoing radiance. The authors report that using 200 light directions yields good results with no visual discontinuities. This means however that 200 pre-computed integrals need to be stored per vertex. The pre-processing step is still very costly, the authors reporting a pre-processing time of 40 minutes for a 150K mesh and 200 light directions. The most important limitation of the technique is that it does not allow for interactive mesh deformations or modifications of material properties without recomputing all the integrals.

Carr *et al.* [37] propose an approach very similar to that of Lensch *et al.* [126], with modifications to allow a full GPU implementation of subsurface scattering. Their paper presents techniques to accelerate matrix radiosity and subsurface scattering. The matrix radiosity solution is computed entirely on the GPU given pre-computed form factors using support for floating point texture formats. Dynamic modification of lighting or reflectance properties is possible. Geometry is fixed however and pre-computation of all throughput factors between interacting surfaces has to be performed beforehand on the CPU. Contrary to Lensch *et al.* , they solve the matrix radiosity linear system on the GPU using a Jacobi technique. As in Lensch *et al.* , they use a texture atlas and a face cluster hierarchy. However, they use a novel multi-resolution mesh atlas applied to a surface cluster hierarchy, taking advantage of the hardware mipmapping capability. The algorithm performs three passes on the GPU [37]:

1. Compute and store irradiance on every patch of the model scaled by the Fresnel transmittance term.
2. Transmitted radiosity is gathered and scaled by the throughput factors. The result is stored in a texture map.
3. The object is rendered with the subsurface scattering light contribution by applying the texture map computed in the second pass scaled by the Fresnel term.

Using a texture atlas has the advantage of mipmapping the scattered irradiance map in a seamless manner. Moreover, the number of surface samples is independent of the mesh tessellation and the screen resolution, in opposition with real-time techniques that use a vertex to vertex approach to discretize the diffusion equation.

The model in Lensch *et al.* [126] is not practical since the global response is computed using a quadratic procedure. Also, all techniques discussed previously do not allow for real-time object deformation. A better technique was proposed by Mertens et al. [149] to palliate those problems. It allows interactive modification of lighting, viewpoint, subsurface scattering properties, and object geometry. The BSSRDF is dependent on the object's geometry; however, the authors note that it is reasonable to remove the solid angle dependencies from the BSSRDF term since multiple scattering diffuses illumination. The BSSRDF now depends only on incident and exitant positions (x_i, x_o). We still however need the incoming and outgoing directions to incorporate Fresnel transmittance. The model for the BSSRDF without solid angle dependencies, $R_d(x_i, x_o)$ (Equation 3.2), should be adaptable to different materials and should be efficient. They also use the dipole diffusion approximation over the full simulation approach. The dipole approximation, even though only valid in theory for highly scattering and homogeneous materials with semi-infinite planar surfaces, produces plausible results with curved surfaces. Radiosity and subsurface scattering share some similarities since a full surface to surface transfer needs to be computed, which is in the order of $O(n^2)$, where n is the number of vertices or faces in a mesh object. They use a hierarchical data structure to reduce the complexity to $O(\log k)$, where k is the number of patches considered. The integral

$$B(x_o) = \int_S E(x_i) R_d(x_i, x_o) dx_i$$

can be reduced to a sum if we break the object's surface into regions A_k with small lighting variations ($E(x_i) = E_k$ constant for all x_i in A_k):

$$B(x_o) = \sum_k E_k F(A_k, x_o),$$

and

$$F(A_k, x_o) = \int_{A_k} R_d(x_i, x_o) dx_i,$$

where $F(A_k, x_o)$ are the subsurface scattering form factors. Different approaches can be used to construct the mesh hierarchy such as face cluster hierarchy or mesh subdivision.

Dachsbacher and Stamminger [49] introduce an extension to standard shadow maps called *Translucent Shadow Maps (TSM).* A standard shadow map texture is rendered from the light's point of view and each texel stores the depth of the closest surface from the light source. TSMs are similar but store, in addition to depth values, irradiance and surface normal at each texel. The integral to compute the exitant radiance at a point x_o can then be computed by filtering the TSM irradiance samples. The evaluation of the subsurface scattering is divided into two phases, as was done in Lensch *et al.* [126], namely the local response (for small distances) and the global response (for larger distances). Note that this distinction is only made in order to speed up the rendering since the local response could well be computed using the more costly approach used in computing the global response. To compute the local response, all texels in the TSM that are in the neighbourhood of the exitant point x_o with a depth value close enough to the depth of x_o are weighted and summed up. The filter weights are heuristics that depend on the difference of depth Δz between the exitant point x_o (in light space) and the incident point x_i stored in the TSM. For large Δz, weights are small and decrease slowly with $(\Delta x, \Delta y)$. For small Δz, central weights are large but decrease quickly. The global response computes the dipole diffusion approximation between x_i and x_o using Δz and the normal at x_i stored in the TSM. The irradiance gathering at x_o is computed using a hierarchical filter based on a mipmap of the TSM. The filter size can be large since the effective subsurface scattering range can be in the order of centimetres for natural materials. Note that the technique is restricted to directional light sources and does not handle concave objects well due to the inherent nature of the translucent shadow map, which only stores the depth of the closest surfaces to the light source at each texel.

Other efforts to perform real-time subsurface scattering include release 1.1 of the *Nvidia Cg Toolkit* [164, 134] which incorporates a Cg skin shader demo. This shader was inspired in part by Pharr [173], which is itself an approximation to the Hanrahan-Krueger model [74] with some simplifications to make it faster and more visually pleasing. Its base reflectance model uses the Blinn model [25] along with a modified Fresnel term that amplifies Fresnel edge effects slightly. The model also incorporates three single subsurface scattering approximation terms, with mean cosine of phase function parameter g values of 0.8, 0.3, and 0.0 (isotropic) respectively. The 0.8 term comes from measured skin scattering data as reported by Hanrahan and Krueger [74]. The other two terms are used empirically to model multiple scattering with an increasing isotropic behaviour, as more scattering events tend to diffuse light.

3.4 Image-based Skin Rendering

Effects such as self-shadowing, inter-reflections, and multiple scattering are quite difficult and costly to simulate for a specific individual using the skin models discussed previously. Image-based techniques attempt to tackle the problem from a different angle. Some works in computer graphics use image-based techniques for skin representation and BRDF data acquisition. Georghiades *et al.* [67] and Debevec *et al.* [51] acquire the reflectance field of a human face. The latter work acquires a non-local reflectance field (directional illumination) of the face from two fixed cameras and varying illumination directions using a device they call a *lightstage*. They can then generate images of the face from the original viewpoints under any illumination conditions by computing linear combinations of the original images. The additive nature of light also allows to perform face re-lighting with sampled natural lighting environments, called light probes. However, they must use a skin reflectance model along with a geometric model of the face in order to render the subject under novel viewpoints.

The previous approach palliates the problem of textures with fixed illumination. A technique similar in spirit is the polynomial texture map (PTM) of Malzenber *et al.* [133]. This is a technique that aims at capturing the bidirectional texture function (BTF) of a surface by collecting multiple images of a static object with a static camera under varying lighting conditions. Coefficients of a biquadratic polynomial are stored per texel, which can be used to approximate the surface colour under varying lighting conditions in real-time using graphics hardware. It would therefore be interesting to apply PTMs to the lightstage results of Debevec et al. [51] in order to perform real-time rendering of human faces.

3.5 Level of Detail

The level of detail problem was first discussed in computer graphics by Clark [42] and is an important aspect to consider when discussing reflectance models. Level of scales in geometry are often divided into macro-structure, meso-structure, and micro-structure, and several works investigate transitions between levels of representation [36, 64, 169, 226]. The macro-structure, meso-structure, and micro-structure are usually represented with distinct rendering algorithms:

$$\begin{array}{rcccl} Macro-scale & \longleftrightarrow & Meso-scale & \longleftrightarrow & Micro-scale \\ BRDF & \longleftrightarrow & Bump\ Mapping & \longleftrightarrow & Displacement\ Mapping \end{array}$$

The rendering algorithm is chosen as a function of distance, viewing angle, and the bump frequencies in the bump map to provide the best trade-off between quality and computation time. The BRDF of the surface is sometimes constructed from distributions of normals recorded from various views of a single displaced surface patch.

Macro-structure Level

The macro-structure level is a geometric model represented as a polygonal mesh, curved surface, etc. It can be created in a geometric modelling application, acquired from 3D scanning devices or photographs, or any other acquisition technique. Geometry-based representations usually consider direct illumination and self-shadowing. Global illumination methods account for inter-reflections.

Meso-structure Level

The meso-structure level consists of geometric details that are finer but still visible and is usually represented as a bump or displacement map. Meso-structure details are very important in order to render convincing human skin at high resolutions. Techniques for shading bump maps were developed and can be used to render skin surface details. Max [144] proposes a technique to compute self-shadowing of bump maps called *Horizon Mapping*. Masking was investigated by Becker and Max [23]. For real-time bump map synthesis, Kautz *et al.* [105] present a method that automatically synthesises bump maps at arbitrary level of detail in real-time using a normal density function as input. Normal map filtering for level of detail was investigated by Fournier [63, 64]. Self-shadowing and inter-reflections in bump maps were investigated by several authors [80, 144, 193].

As observed by Yamada *et al.* [240] in a simple skin replica surface model, inter-reflections are most likely to affect low pixel intensities in an image. This is illustrated in Figure 3.3. The inter-reflections augment the pixel intensities, in addition to direct illumination. On surface A, most indirect light comes from B which has a small reflected radiance due to its orientation to the light source. The indirect light at B is much stronger since it comes mostly from A whose surface normal is almost parallel to the light direction.

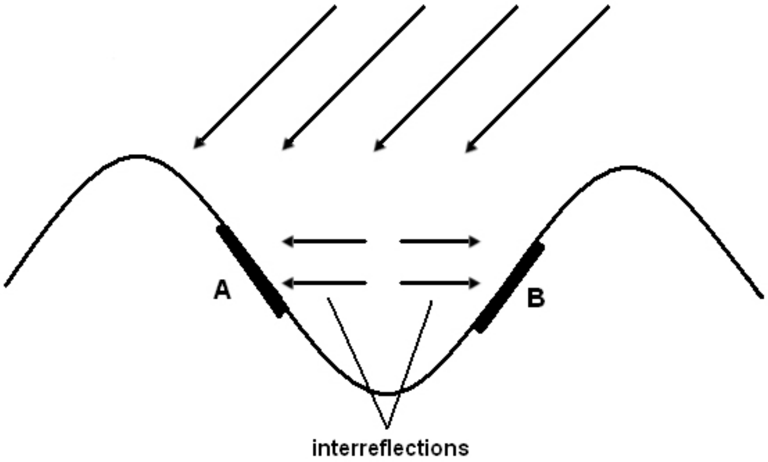

Figure 3.3: Inter-reflections effects in a simple bump map.

Subsurface scattering in bump maps has not been investigated to our knowledge. For highly forward scattering materials, as is the case with skin, we can see that subsurface scattering will mostly affect shadow regions by softening them since light is more likely to "bleed" through the bumps from the lit to the shadow side. This is illustrated in Figure 3.4.

Micro-structure Level

The micro-structure level consists of surface micro-facets that are not visible individually but contribute to the overall BRDF. BRDFs consider direct illumination but also account for self-shadowing and masking effects of the micro-geometry. It also accounts for indirect illumination

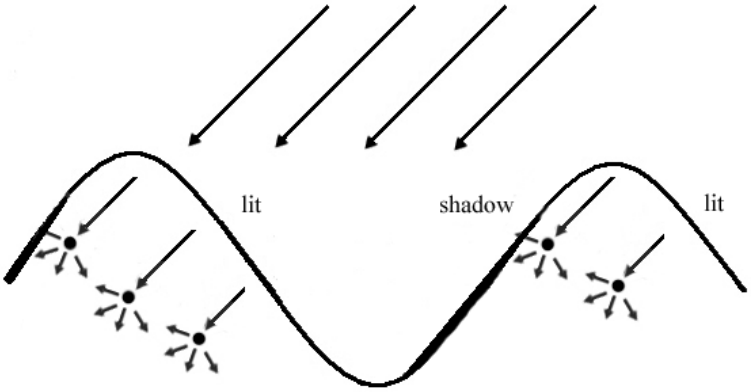

Figure 3.4: Subsurface scattering effects in a simple bump map.

resulting from light that scatters between the micro-facets and subsurface scattering in the material.

3.6 Acquiring and Modelling Skin Meso-structure

Every zone on the human body has a distinct micro- and meso-geometry. The forehead has a different composition than the cheeks or the nose for example. Articulations have wrinkle patterns that are aligned with the axis of motion. Moreover, micro-scale geometry will vary on one individual with age due to a decrease in skin elasticity. Since the overall BRDF of the skin will be influenced by this fine geometry and by other factors such as pigmentation, hair, oiliness, etc., we assume that only a spatially-varying BRDF can correctly model skin reflectance. Another interesting issue, fluctuations in facial skin colour due to variations in emotional state, was investigated by Macy [129]. Skin fine scale geometry mostly consists of ridges, furrows, hair follicles openings, and sweat gland openings. The ridges and furrows create global lattice or net structures. The hair follicles are located in the furrows, whereas sweat glands openings are located on the ridges. The lattice-type pattern is seldom isometric. The repetitive spacing in one direction is generally larger than in the other, and the most common repeat figure is a rectangle or parallelogram. The rectangles are in turned crossed by one or two diagonals, which subdivide them into two or four triangles [151]. Millington and Wilkinson [151] also report that the length of the sides of the triangles varies from about $0.5 - 0.9mm$. The importance of meso-structure for photorealistic skin rendering in computer graphics is highlighted in Plate VII. Until the early 1970s there had been few attempts to describe systematically and in detail the surface characteristics of skin, other than the ridge patterns of the fingers, hands, and feet [151]. Most first reports concerning skin topography were more concerned with the acquisition techniques employed than with the skin site variations.

Geometry in computer graphics can be acquired using 3D scanners, silicon molds, and image-based computer vision techniques. It can also be procedurally generated, or simply created by an artist. Texture on the other hand can be acquired using digital cameras, procedurally generated, or again painted by a skilled artist. Meso-geometry and texture are crucial elements that are required in order to render realistic-looking skin. Several works have been done in computer vision to capture meso-geometry, whether using photometric stereo, shape-from-shading, or laser scanners [32, 131, 142, 143, 155, 162, 184, 186, 187, 239, 240, 243]. Acquiring textures with a digital camera is both fast and easy and can produce realistic texture and bump maps [102, 207]. Texture maps however suffer from fixed illumination, e.g., the illumination present at the time of the capture. Shading removal techniques exist but in the case of skin it is an especially challenging problem. It is therefore sometimes useful to generate skin decal textures procedurally. This is also true for bump maps since capturing accurate skin meso-geometry involves more complicated apparatus, whether using a scanner [155], molds [76], or using a shape-from-shading approach. Procedural textures also do not suffer from seaming artifacts or distortion and can be used as 3D textures. They can also reveal quite useful in the design of imaginary characters.

Haro *et al.* [76] acquire normal maps for different zones of the face by using small latex molds employed in cosmetology. A shape-from-shading algorithm is performed to derive the normal maps from the latex samples. Since the samples are small (about the size of a nickel), a texture synthesis algorithm [56, 225] is performed to generate high resolution versions of the normal maps. In effect, this is an implicit approximation of the stochastic processes that generated each sample.

It is important to avoid any visual discontinuities between the different zones of the face. The authors employ random multi-resolution splines in an attempt to hide the seams across different patches. The motivation behind this is that curved boundaries suppress the highly noticeable visual artifacts associated with seams between rectangular regions. Texturing might also be accomplished using the lapped textures of Praun et al. [181]. Finally, per-pixel bump mapping is used in conjunction with a Lafortune shading model [124] that approximates the skin BRDF to render a model in real-time. More manipulation has to be considered if the latex sample is not perfectly flat. Only the high frequency perturbations are of interest in this case.

Ishii *et al.* [89, 90] model ridges and furrows using a simple model. They generate a 3D micro-scale geometric model of skin using a Voronoi diagram to represent the different skin cells and use the optical scattering properties of the skin layer to perform rendering. Geometric diversity is obtained using pseudo-fractal subdivision in the Voronoi procedure. Voronoi subdivision is applied hierarchically in order to obtain different levels of scale on the ridge surfaces. Each level of a ridge surface is represented by a cubic Bézier patch whose control points can be edited to produce different effects. The editable geometric parameters of the model are the original disposition of the Voronoi points (triangle lattice, square lattice, and random), the pseudo-fractal variation of the base polygon edges, the anisotropic scaling, the number of hierarchy levels, and the Bézier patch control points. More skin appearances can also be obtained by varying the optical properties of the skin layers. The optical parameters of the model are the total number of layers, the thickness of each layer, the layer absorption and scattering coefficients, and the refraction indices.

Voronoi-based textures can produce patterns that are similar to skin cells [90]. A Voronoi bump map is shown in Figure 3.5. We use a centroidal Voronoi algorithm that iteratively relaxes the Voronoi points, allowing the user more flexibility to manipulate the overall uniformity of the resulting bump map. Using a user-specified probability density function to generate the Voronoi points also helps to simulate anisotropic behaviour, as was done by Secord [191] to produce stippling drawings in a non-photorealistic rendering context. We use a hardware-based approach similar to that of Hoff *et al.* [84] to compute our Voronoi diagrams. We also experimented with Worley cellular textures [233], as shown in Figure 3.6. Real skin surface images from various zones of the body are shown in Figure 3.7. We believe that other procedural and computational tools could be used to create various synthetic skin patterns, such as reaction-diffusion [216] and fractal textures for example. Kukla and Bedwell [123] produce skin textures using a fractal approach and their result is shown in Plate VIII. We also show in Plate IX a skin decal texture that we made with a simple noise generator using a commercial animation software. Plate X from Macy [129] shows images of real human female skin acquired with a flatbed scanner. These images are all from the same individual and even greater variations would be found among different individuals. Single pores on the nose seem to follow a Poisson distribution whereas wrinkles in the eyelids and lips are clearly anisotropic. Understanding these meso-scale features and providing high-level tools for artists to generate and manipulate the resulting textures and bump maps is key to developing better applications geared toward human skin modelling and rendering. It would certainly be interesting to develop a morphological model of skin that creates a texture from a few simple parameters, therefore allowing human skin texturing on arbitrary models. A sphere rendered using a procedural decal texture and a Voronoi bump map is shown in Plate XVII (left). The same sphere is shown on the right with subsurface scattering added.

Wrinkle Modelling and Simulation

Wrinkle modelling and simulation was investigated in computer graphics by several authors [22, 28, 219, 220, 235, 236, 237, 238]. Wrinkles can add realism to synthetic characters and wrinkle animation can help to better convey facial expressions. Some applications in cosmetology also exist.

3.7 Asperity Scattering

Asperity scattering occurs when an object is covered with a thin layer of sparse scatterers, for example dust, hair, or high local curvature areas at its surface [115, 128]. Skin, especially facial skin of young children and women, is covered with small light hairs. An example of asperity scattering at the surface of the cheek is depicted in Plate XI.

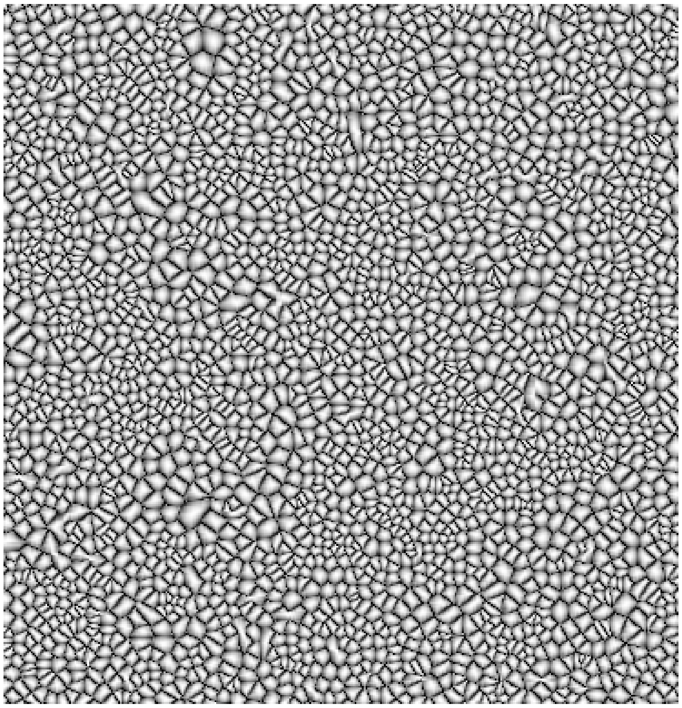

Figure 3.5: Example of a Voronoi bump map.

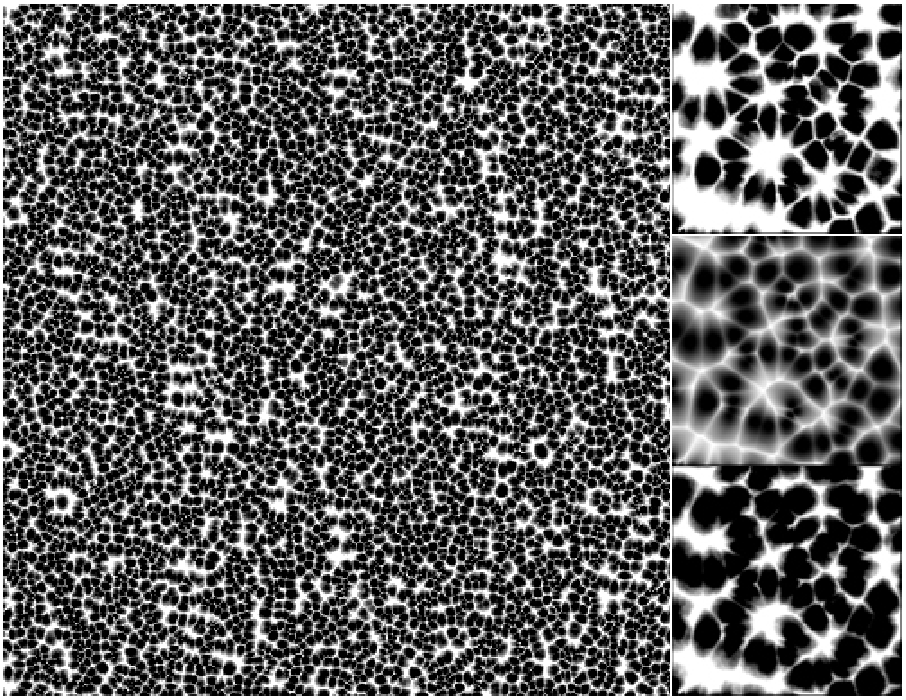

Figure 3.6: Example of a Worley bump map.

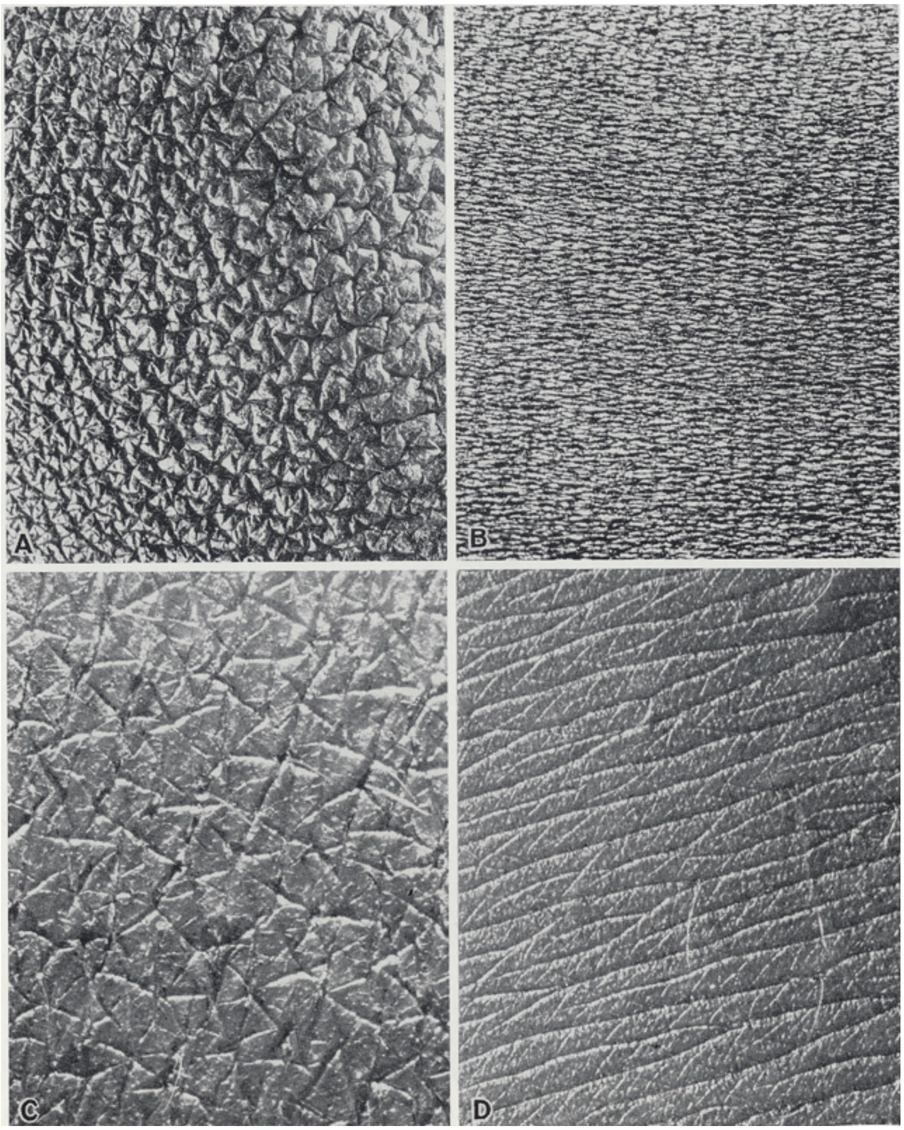

Figure 3.7: Surface inscription from (A) the elbow, (B) antecubital fossa, (C) knee, and (D) popliteal fossa of the same subject (from Montagna and Parakkal [152]).

Koenderink and Pont [115] derive a simple model to represent the asperity scattering lobe. The asperity scattering lobe influences mostly the occluding contour and the shadow terminator. According to them, the translucent or “milky” quality of skin is due to subsurface scattering whereas the soft or “peachy” quality is due to asperity scattering. The model assumes a layer of constant thickness Δ with uniform distribution of scatterers. The scatterers are sparse and therefore only single scattering is taken into account. The probability of a ray entering from a direction l and scattered back towards the viewer in direction e is derived in Koenderink and Pont [115]. The resulting BRDF for an optically thin layer of surface scatterers is:

$$f(l,e) \approx \frac{p(-l \cdot e)(\frac{\Delta}{\lambda})}{(n \cdot l)(n \cdot e)}, \tag{3.8}$$

where

$\Delta \ll \lambda$,

$p(-l \cdot e)$: phase function,

Δ : layer thickness, and

λ : mean free path in layer.

In the case of isotropic scatterers, Equation 3.8 becomes:

$$f(l,e) \approx \frac{\Delta \ / \ 4\pi\lambda}{(n \cdot l)(n \cdot e)}, \tag{3.9}$$

where $\frac{\Delta}{\lambda} \ll 1$ and $p(-l \cdot e) = \frac{1}{4\pi}$.

Clearly, from Equations 3.8 and 3.9, we can see that the asperity scattering lobe is inversely proportional to the cosines of illumination and viewing angles and directly proportional to the phase function. We can clip the BRDF to prevent Equations 3.8 and 3.9 from becoming unstable when the view or light vector grazes the surface. The asperity scattering lobe is shown in Plate XII against a Lambertian sphere. We can see that the effect of asperity scattering is predominant on the contour and the shadow boundaries and is far from exhibiting Lambertian behaviour. Koenderink and Pont show this by comparing a picture of a velvet cylinder to a Lambertian cylinder (Figure 3.8). Notice that the velvet is lightest where the Lambertian surface is darkest and vice versa. Even though the asperity scattering lobe has a small quantitative impact on the total outgoing radiance, it might have a strong perceptual role since it mostly affects contours and body shadows. The importance of contours has been recognised for ages by artists and has also been studied in non-photorealistic rendering [69, 135, 201]. Cinematic “rim lighting” also exploits Fresnel effect and asperity scattering to improve the contrast between the actor and the background. The importance of contour is depicted in Figure 3.9. Notice how the left sphere looks “softer” and “less dark” when compared to the right sphere.

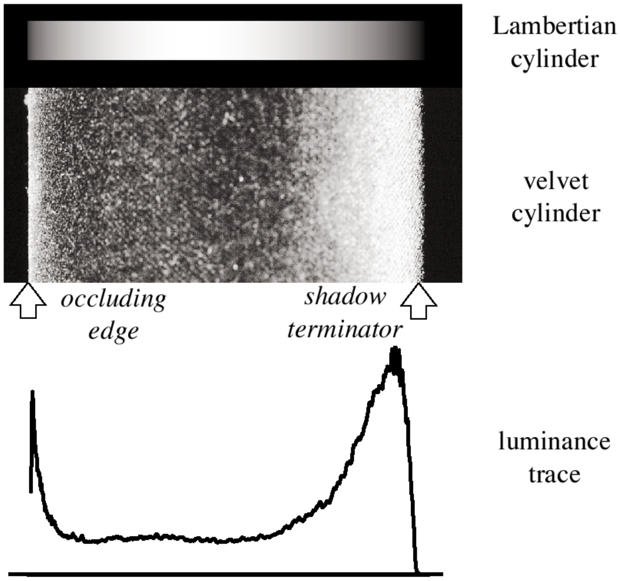

Figure 3.8: Velvet cylinder against Lambertian cylinder (from Koenderink and Pont [115]).

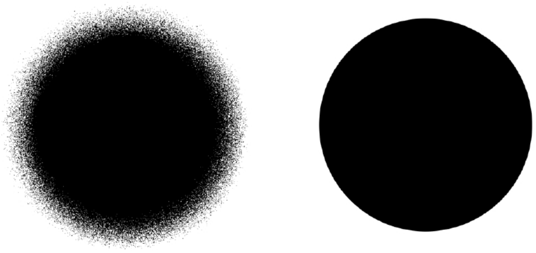

Figure 3.9: Effect of contour on perception (from Koenderink and Pont [115]).

Chapter 4

Implementation and Results

Our contributions to human skin modelling and rendering are twofold. First, we present a quantitative approach in Sections 4.1 to 4.1.8 that describe a simple physiologically-based model for the reflectance of human skin. Second, we present a qualitative approach in Sections 4.2 to 4.2.8 where we propose a system to support skin modelling and rendering. Our skin reflectance model is one tool among many that could be used in such a system.

4.1 A Simple Model for the Reflectance of Human Skin

We now present a computationally efficient model of skin colour which is able to compute skin reflectance from different body parts, different races, and different individuals. The model is parametrized in terms of lightness, melanin concentration, and hemoglobin concentration, which provide a good basis for an intuitive modelling interface.

4.1.1 Research Objectives

To start we lay out the goals of our model of skin colour. First, we wish to start with skin physiology. Skin varies by race, by body location, by physical state, etc., but it is a single material, one substance with varying physiological parameters, such as melanin concentration, blood flow, and thickness. A good model will vary similarly. Second, we want to keep the final results as computationally close to the model as possible, so that it is easy to discover how model variations map onto variations in colour. Thus, we want to simplify at the level of the model, doing as much mathematics as possible analytically rather than computationally. Third, we want the model to provide spectral reflectance, not just tristimulus values, because the play of illumination on skin is an important aspect of skin perception. In any case spectral reflectance models can easily provide tristimulus values when they are needed. Fourth, we want the model to be computationally efficient, because skin rendering is done at high resolution, and the model is evaluated frequently. Fifth, a model should be useful for hand-modelling, where an artist or animator specifies the variation of skin colour, and also useful for applications where the skin is connected physiologically to other body components such as muscles. Fortunately, these requirements are similar: the cognitive and emotional conditions that concern the artist are indicated by a small number of physiological factors, such as blood flow. Thus, a model parametrized using physiological variables is also useful to the artist. The duality of the fifth objective shows the difference between two views of the relationship between modelling and rendering. For hand-modelling two things matter.

1. The set of all combinations of parameter values determines a set of material properties. All needed materials must be available in the set, but the exact values that generate a material are unimportant.
2. Adjusting parameter values should change material properties predictably and intuitively. This feature makes modelling understandable and learnable.

Thus, for hand-modelling the primary criterion of success is existential: does there exist an easily achievable set of parameters specifying a material with desired properties. By contrast, coupling the model to a physiological simulation requires a match between externally specified physiological properties, such as volume fraction of blood, and calculable values of the input parameters. If, for example, the physiological simulation specifies that a particular volume fraction of blood is present, then it should be possible to supply that value to the skin model to produce skin of an appropriate colour. This criterion is universal: for every combination of physiological input parameters the skin model should produce the correct colour for that exact combination. This criterion is, of course, the goal of medical models of skin colour. Tests of computer graphics models are very commonly implicitly existential, asking, "Can the model provide satisfactory images?". For this primary reason we restrict the tests done in this dissertation to existential ones. (In any case, our laboratory lacks the ability to make in-vivo measurements of parameters such as volume fraction of blood, as do most medical laboratories.) We will, however, describe calibrations that would make it possible to extend our skin model so that it would pass universal tests.

4.1.2 Overview of the Model

The model described here is developed in a sequence of distinct stages, starting with the simplified model of skin optics described by Jacques (Chapter 2). This source is attractive because Jacques supplies optical properties appropriate for his model, and because physiological measurements can be taken under a wide variety of conditions. Medical investigators are far better equipped than computer scientists for matching particular measurements to components of what are inevitably schematic models. Then, assuming that our skin model will be illuminated in restricted ways and viewed at a restricted range of resolutions we further simplify the model, at which point it is possible to solve the equations that describe light transport. The solutions are used to compute reflectances for all physiologically plausible values of its parameters. The resulting data set is then linearized using Principal Components Analysis [62, 92]. The resulting model provides skin parametrized by concentration of melanin (how tanned the skin is), by concentration of blood (how flushed the skin is), and by skin thickness, which distinguish skin on different parts of the body.

4.1.3 A Simple Model of Skin Anatomy and Optics

This section describes a mathematical model of light transport in skin. The model is based on the compilation of Jacques et al. [93, 94, 218], which contains a complete set of suitable data. The model consists of a set of layers in which light scatters and is absorbed, with scattering and absorption coefficients that are tailored to the model. The remainder of this section describes and formalizes this model, introducing some additional approximations which are appropriate for computer graphics applications.

Our simple model is parametrized by melanin concentration in the epidermis, by hemoglobin concentration in the superficial horizontal plexus, and by the thickness of the dermal layers above and below the superficial plexus. The basic structure of the model is shown in Figure 4.1. The outermost layer is the epidermis and light passing through the epidermis is coloured by the presence of melanin chromophores, which absorb preferentially at short wavelengths. The concentration of melanin in the epidermis is one parameter of the model. Directly below the epidermis is a dermal layer (papillary dermis) composed mainly of small-scale collagen fibres that scatter light. The depth of this layer is one parameter of the model. Below this layer is the superficial horizontal plexus, in which are located most of the superficial dermal blood vessels. The presence of hemoglobin — oxygenated and de-oxygenated — colours light passing through this layer. The concentration of hemoglobin in this layer is another parameter of the model. Below the superficial plexus is another layer of collagen that is part of the reticular dermis, the thickness of which is the final parameter of the model. Only a very small amount of the incident light penetrates as far as the deep plexus, which is treated as a light absorbing background. Light enters the skin through the outer epidermis, is scattered, absorbed or transmitted through the different layers, then re-emerges. The ratio of re-emitted light to incident light is the skin reflectance.

No model-dependent adjustment of spectral dependencies is done; all spectral dependence that appears in the model is the result of unmodified physiological measurements. Skin reflectance calculated in the model depends on volume fractions of the pigmented components and thicknesses of the layers. These are treated as adjustable in the model — they produce the different types of skin. We are careful to ensure that values for these parameters remain physiologically reasonable.

Light Passing Through the Epidermis

The thickness of the epidermis layer varies among individuals and locations on the body. Table 2.1 provides good thickness approximations for a selected set of body sites. The variation of density of melanosomes, $1-2\ \mu m$ granules that are highly pigmented by melanin, plays the most important

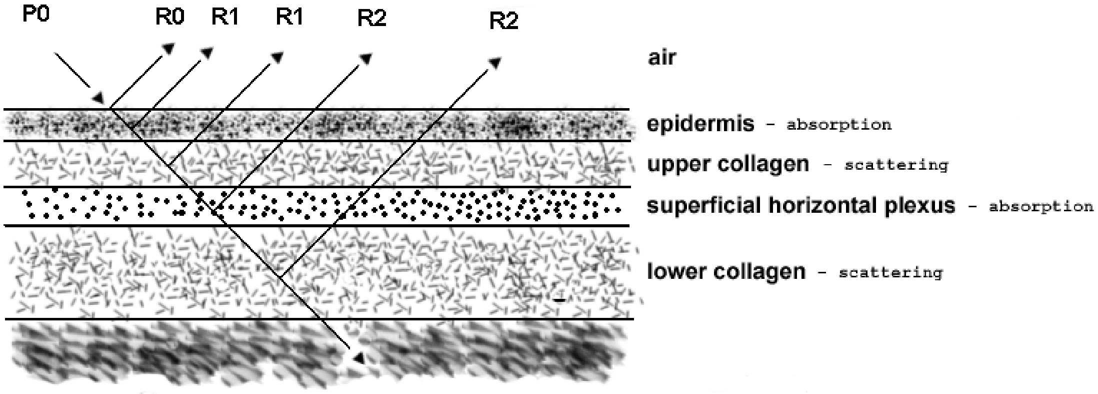

Figure 4.1: Reflected radiance from the simple human skin model.

role in colouring the light passing through the epidermis. As was seen in Chapter 2, the volume fraction of melanosomes can vary from 1% for light white skin to about 45% for dark black skin. The epidermis is thus a two-component system, one component being the basic skin, which is pigmentless. The basic skin is almost transparent: Jacques [94] models it as the skin baseline (Section 2.1.2). Besides basic skin the epidermis contains the melanosomes. Define K_{sb} as the absorption of the basic skin, and K_m as the absorption of one melanosome, with K_m about a thousand times larger than K_{sb}. Our simple model neglects scattering in the epidermis, so we take $S_{sb} = S_m = 0$. This is a valid simplification since epidermal scattering is incomplete, i.e., much of the incident radiation is transmitted with little deviation in direction (the mean cosine of phase function g for the epidermis is about 0.7-0.95).

Using Beer's Law (Section A.9) and the formulas of Chapter 2 to describe the absorption behaviour in the epidermis [94], the transmittance of the epidermis can be written as

$$T_e(\lambda) = e^{-(K_m(\lambda)c_m \ + \ K_{sb}(\lambda)(1-c_m))\theta_e}, \tag{4.1}$$

where θ_e is the thickness of the epidermis, c_m the volume fraction of melanosomes, and the wavelength-dependence of both transmittance and absorption are indicated explicitly.

Light Passing Through the Superficial Horizontal Plexus

The superficial plexus is a three-component system: basic skin, oxygenated blood, and de-oxygenated blood. The corresponding absorption coefficients are K_{sb}, K_{ob}, and K_{db}. The simple model neglects scattering in the superficial plexus: $S_{sb} = S_{ob} = S_{db} = 0$. Again using Beer's Law and the formulas of Chapter 2 to describe the absorption behaviour in the dermis [94], the transmittance of the superficial plexus of thickness θ_{sp} is then

$$T_{sp}(\lambda) = e^{-(K_{ob}(\lambda)c_{ob} \ + \ K_{db}(\lambda)c_{db} \ + \ K_{sb}(\lambda)(1-c_{ob}-c_{db}))\theta_{sp}}. \tag{4.2}$$

Often, only the overall blood concentration is known, and not the breakdown into oxygenated and de-oxygenated blood. When this is the case we use an approximate transmittance

$$T_{sp}(\lambda) = e^{-(K_b(\lambda)c_b \ + \ K_{sb}(\lambda)(1-c_b))\theta_{sp}}, \tag{4.3}$$

where $K_b(\lambda)$ is a suitable average of $K_{ob}(\lambda)$ and $K_{db}(\lambda)$, and $c_b = c_{ob} \ + \ c_{db}$.

Light Scattering by Collagen

To describe light scattering by a collagen layer of a given thickness we use a simple one dimensional model, illustrated in Figure 4.2. At the top of the layer light of intensity I_T enters, and light of intensity I_R exits. At the bottom of the layer, light of intensity J_T exits, while light of intensity J_R enters. We regard I_T and J_R as given and want to discover the values of I_R and J_T. Since there is no absorption in the layer the intensity of light entering the layer must be equal to the intensity of light leaving the layer. Thus,

$$I_T \ + \ J_R = I_R \ + \ J_T. \tag{4.4}$$

We now need a model of scattering which determines how the intensity leaving is distributed among its two components. The model we use is in the spirit of the Kubelka-Munk model, which has for many decades been used to describe paint mixing. Using this scattering model allows us to derive an analytic expression for skin reflectance. It would however be possible to use a more accurate scattering model [174] to produce a BRDF of comparable precision.

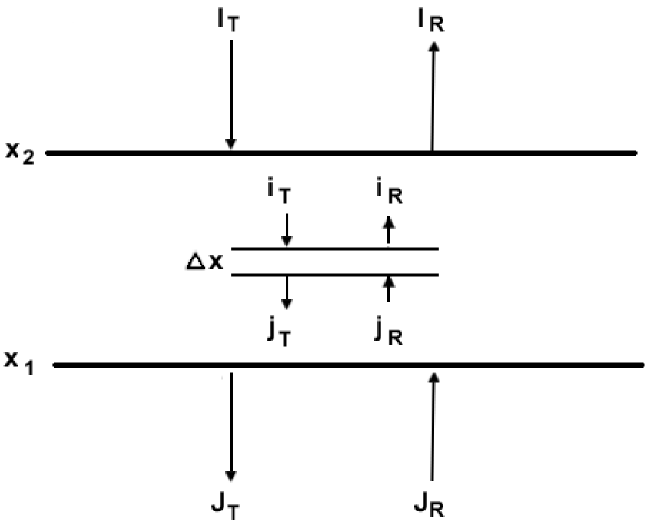

Figure 4.2: One dimensional scattering model for collagen layers.

The mathematics of the Kubelka-Munk model is developed in Appendix B for the case where both absorption and scattering are present. We do not use that solution here because it is degenerate when absorption is absent and qualitatively different solutions occur.

The Kubelka-Munk model looks at a small slab of thickness Δx within the layer. Entering it from above is an intensity i_T, and from below an intensity j_T. Within the slab there is a probability $S\Delta x$ that a unit intensity of light will be scattered from upward to downward, or vice versa. Thus,

$$j_T = i_T \; - \; S\Delta x \; i_T \; + \; S\Delta x \; j_R,$$

and

$$i_R = j_R \; - \; S\Delta x \; j_R \; + \; S\Delta x \; i_T.$$

Now, let x be a variable, increasing upward, taking on the value x_1 at the bottom of the layer and x_2 at the top of the layer. If the small slab is at x, then $i_T = j_T(x + \Delta x)$ and $i_R = j_R(x + \Delta x)$. We can then write the two equations above as

$$\frac{j_T(x + \Delta x) \ - \ j_T(x)}{\Delta x} = Sj_T(x) - Sj_R(x),$$

and

$$\frac{j_R(x + \Delta x) \ - \ j_R(x)}{\Delta x} = Sj_T(x) - Sj_R(x).$$

Taking the limit as the thickness of the slab goes to zero gives a pair of differential equations,

$$j_T{}'(x) = Sj_T(x) - Sj_R(x),$$

and

$$j_R{}'(x) = Sj_T(x) - Sj_R(x).$$

It is immediately obvious that the difference of the fluxes, $\sigma(x) = j_T(x) - j_R(x)$, obeys the differential equation $\sigma'(x) = 0$. Integrating this equation gives

$$\sigma(x) = I_T - I_R = J_T - J_R = \sigma_0$$

from which follows the energy conservation identity $I_T + J_R = I_R + J_T$.

To complete the solution define the sum of the fluxes by $\rho(x) = j_T(x) + j_R(x)$. It is the solution of the differential equation

$$\rho'(x) = 2S(j_T(x) - j_R(x)) = 2S\sigma_0.$$

The solution is

$$\rho(x) - \rho(x_0) = 2S\sigma_0(x - x_0),$$

which can be expressed in terms of the incoming and outgoing fluxes as follows:

$$I_T + I_R - (J_T + J_R) = 2S(I_T - I_R)(x_1 - x_0).$$

Now, remember that we want to solve for I_R and J_T in terms of I_T and J_R. The results are

$$I_R = \frac{S(x_1 - x_0)I_T + J_R}{1 + S(x_1 - x_0)}, \tag{4.5}$$

and

$$J_T = \frac{I_T + S(x_1 - x_0)J_R}{1 + S(x_1 - x_0)}. \tag{4.6}$$

Comments

1. The limiting cases where the layer is infinitely thin ($x_1 = x_0 : I_R = J_R$ and $J_T = I_T$) and infinitely thick ($x_1 - x_0 = \infty : I_R = I_T$ and $J_T = J_R$) are obviously correct.

2. Two special cases of the layer with scattering are interesting. The first is the black case, where the substance below the scattering layer is black and $J_R = 0$. Then,

$$I_R = \frac{S(x_1 - x_0)I_T}{1 + S(x_1 - x_0)}.$$

   The second is the white case, where the substance below the scattering layer is white and $J_T = J_R$. Then, $I_R = I_T$, which is exactly the same solution as the infinitely thick layer limiting case.

3. The scattering coefficient S can be wavelength-dependent without affecting any of the results, except of course making them wavelength-dependent.

4. The scattering coefficient can vary with depth in which case it is written $S(x)$. The solution for $\rho(x)$ is then

   $$\rho(x) = \rho(x_0) + 2\sigma_0 \int_{x_0}^{x} S(x)dx.$$

   The solution proceeds in terms of the initial conditions with the obvious substitution of the integral given in place of the linear form that appears above.

5. These equations can be used to calculate the reflectance and transmittance of a thickness of collagen. The reflectance is the fraction of light re-emitted through the surface by which it entered (J_T/J_R when $I_T = 0$, or I_R/I_T when $J_R = 0$):

   $$R(\lambda) = \frac{S(\lambda)\theta}{1 + S(\lambda)\theta} \tag{4.7}$$

   where θ is the thickness and where explicit wavelength dependences have been included. The comparable expression for the transmittance is:

   $$T(\lambda) = \frac{1}{1 + S(\lambda)\theta}. \tag{4.8}$$

Putting the Pieces Together

When light is incident on the skin the reflectance is separated into three parts (Figure 4.1):

1. a part that passes through the epidermis and is scattered in the upper collagen, passes once more through the epidermis, and is re-emitted from the skin.

2. a part that passes through the epidermis, the upper collagen and the superficial plexus, is scattered in the lower collagen, passes once more through the plexus, the upper collagen and the epidermis, and is re-emitted from the skin, and

3. a part that is re-emitted having interacted with neither melanin or hemoglobin. This part includes specular components, light reflected by non-skin elements such as hair, and so on.

These three parts are added together to produce the light that is re-emitted when the skin is illuminated.

Epidermal Light

The part of light that is coloured only by the epidermis is subject to three processes that affect its colour:

1. transmission through the epidermis, $T_e(\lambda)$,
2. reflection in the upper collagen layer, $R_{uc}(\lambda)$, and
3. a second transmission through the epidermis, $T_e(\lambda)$.

Thus, given incident illumination of intensity I_λ, light that is coloured only by the epidermis produces reflected light of intensity

$$\Phi_\lambda^e = T_e(\lambda)R_{uc}(\lambda)T_e(\lambda)I_\lambda = I_\lambda \frac{S_c(\lambda)\theta_{uc}}{1 + S_c(\lambda)\theta_{uc}} e^{-2(K_m(\lambda)c_m + K_{sb}(\lambda)(1-c_m))\theta_e}. \tag{4.9}$$

Dermal Light

The part of light that is coloured by the dermis is subject to seven processes that affect its colour:

1. transmission through the epidermis, $T_e(\lambda)$,
2. transmission through the upper collagen layer, $T_{uc}(\lambda)$,
3. transmission through the superficial plexus, $T_{sp}(\lambda)$,
4. reflection in the lower collagen layer, $R_{lc}(\lambda)$,
5. a second transmission through the superficial plexus, $T_{sp}(\lambda)$,
6. a second transmission through the upper collagen layer, $T_{uc}(\lambda)$, and
7. a second transmission through the epidermis, $T_e(\lambda)$.

This is the most simple process by which blood colours light, but there are others. In the simple model they can easily be enumerated as an elaboration of processes 3 to 5.

After step 5 reflection in the upper collagen layer is possible, followed by steps 3 to 5 again, and this can be continued up to an infinite number of times. The result is the sum:

$$V + VWV + VWVWV + \ldots = V \sum_{i=0}^{\infty} (WV)^i = \frac{V}{1 - VW}, \tag{4.10}$$

where V is the effect of steps 3 to 5 and W is reflection in the upper collagen layer. These processes, all taken together give reflected light of intensity:

$$\Phi_\lambda^d = T_e(\lambda) T_{uc}(\lambda) \frac{T_{sp}(\lambda) R_{lc}(\lambda) T_{sp}(\lambda)}{1 - T_{sp}(\lambda) R_{lc}(\lambda) T_{sp}(\lambda) R_{uc}(\lambda)} T_{uc}(\lambda) T_e(\lambda) I_\lambda. \tag{4.11}$$

All the Parts

The three parts are added together to give the total light re-emitted in the presence of illumination. The result is:

$$\Phi_\lambda = \Phi_\lambda^e + \Phi_\lambda^d + \Phi_\lambda^r, \tag{4.12}$$

where the final term is re-emitted light that is unaffected by either melanin or blood. Obviously even this simple model is too complex for a comprehensive analysis, and we will simplify it substantially before submitting it to analysis.

4.1.4 Simplifications and Approximations

In formalizing the model one important approximation is made: light flow is assumed to be perpendicular to the surface. In effect, the model retains only the components of light flow perpendicular to the surface of the skin. Why is this reasonable?

The model is translationally invariant. Thus under uniform illumination light flow parallel to the surface is equally likely to occur in any direction. For calculating reflectance the net light flow through the surface is all that matters. The sum of the horizontal light flow is zero, so these components can be ignored. This argument simplifies away several factors that are not important for our model.

1. Light flowing obliquely through a pigmented layer experiences a longer path length than light passing perpendicularly. On average this effect is identical to a pigmented layer with slightly higher pigment concentration. Because our success criteria are existential we are happy to compensate in this way.

2. The correct angular distribution of reflected light is lost. This loss does not concern us because we are only trying to model skin reflectance.

We must also consider the length scale on which light must be uniform for this argument to be valid. In skin light travels only one or two millimetres. Thus, illumination is effectively uniform if its variation is negligible on a scale of a few millimetres. But to look at skin on a scale smaller than a few millimetres it is necessary to consider the horizontal micro-structure of skin, pores, hair and the rest. Our model does not attempt to be valid on scales that small so it is reasonable to consider skin as being translationally invariant and illumination to be uniform. This assumption of one-dimensionality is very powerful because it allows us to formalise light transport in the style of Kubelka-Munk [121]. (Indeed, the ongoing success of the Kubelka-Munk model for many pigmented materials justifies a one-dimensional approximation.) Thus, we use simple models of light transport in each layer, matching results at the layer boundaries.

4.1.5 Relationship to Other Skin Models

Our model is closest in spirit to models created within the biomedical community for optical diagnosis of pathological skin conditions. Such models describe skin as a layered structure and use Kubelka-Munk-like optical transport models. The closest of these models to ours [46] (Section 3.1) is focused on image analysis of RGB images of skin and therefore restricts its calculations to RGB values, and does not concern itself with how to render the results. Other biomedical models such as [147, 148] (Section 3.2) use non-analytic techniques, like Monte Carlo simulation, to analyse their models, precluding the intuitive connection of parameters to physiology that is possible in our model. In computer graphics skin models close to ours [74, 174] (Section 3.2) also use Monte Carlo techniques. This enables them to obtain BRDFs, but both studies ignore the importance of computing reflectance and of working from measured spectral properties of physiological materials.

There have also been several excellent measurements of the BRDF of skin [15, 139] (Section 2.7). But while such studies provide valuable data that can be compared with skin reflectance and used for shading, they have limitations for modelling. Every desired type of skin must be measured separately, and interpolation between measurements is difficult for the modeller to control. A recent study [214] (Appendix D.2) uses measured data to produce a linear model, as we do in Section 4.1.7. Measured data, unfortunately, has an unknown sampling bias.

4.1.6 Testing the Simple Model

Our model was first tested by producing groups of reflectances in which particular parameters are varied systematically within biologically valid ranges. The graphs, shown in Figures 4.3 to 4.8, all show the expected behaviour.

In Figure 4.3 we vary the epidermis layer thickness from 50 μm to 150 μm. As expected, increase in epidermal thickness results in decrease in overall reflectance because more light is absorbed by melanin. Moreover, less light reaches the superficial plexus and thus the characteristic "W" absorption pattern of oxy-hemoglobin becomes less distinguishable as we increase the epidermis thickness. In Figure 4.4 we vary the volume fraction of melanosomes in the epidermis from 1% to 46%, ranging from a very lightly pigmented white skin to a highly pigmented black skin. Increasing melanin concentration lowers the reflectance across the spectrum, and particularly at short wavelengths. The lowest curves appear dark brown under most illumination, which is typical of dark skin. The highest curves have the reflectance of very fair skin, with the signature of hemoglobin prominent. This is in accordance with reflectance measurements done by Angelopoulou et al. [14] among four ethnic groups (Plate II and III). In Figure 4.5 we vary the upper collagen layer thickness from 100 μm to 200 μm. As expected, an increase in the collagen layer thickness results in an increase in overall reflectance. In Figure 4.6 we vary the superficial plexus layer thickness from 50 μm to 100 μm. As expected, increase in superficial plexus thickness results in decrease in overall reflectance because more light is absorbed by blood. In Figure 4.7 we vary the volume fraction of blood in the superficial plexus from 1% to 10%. Increasing hemoglobin concentration lowers the spectral reflectance near 550 *nm* and 450 *nm*, showing the signature of hemoglobin, a double minimum near 550 *nm* and a sharp fall-off at 450 *nm*, giving the skin a reddish appearance. Such reflectances are typical of increased blood flow near the skin surface, such as occurs with exercise. Finally, in Figure 4.8 we vary the lower collagen layer thickness from 1000 μm to 2000 μm, where again an increase in the collagen layer thickness results in an increase in overall reflectance.

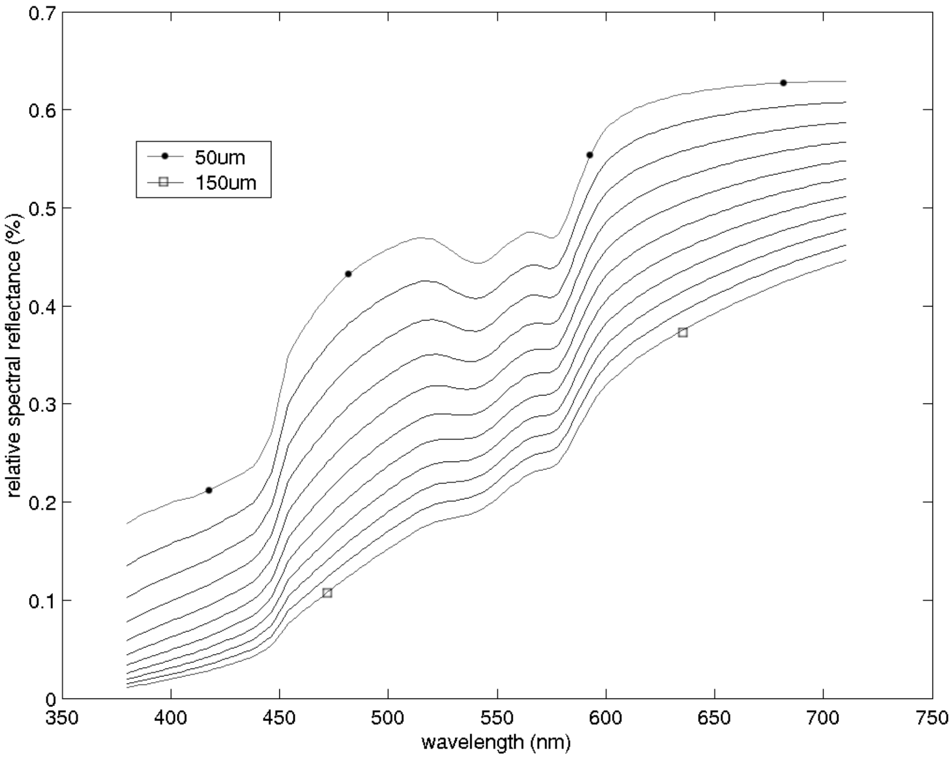

Figure 4.3: Variation of reflectance with epidermal thickness. The black dots and empty squares are simply used to distinguish the curves.

Thus, the reflectance variations in our model correctly reproduce effects that are observed when

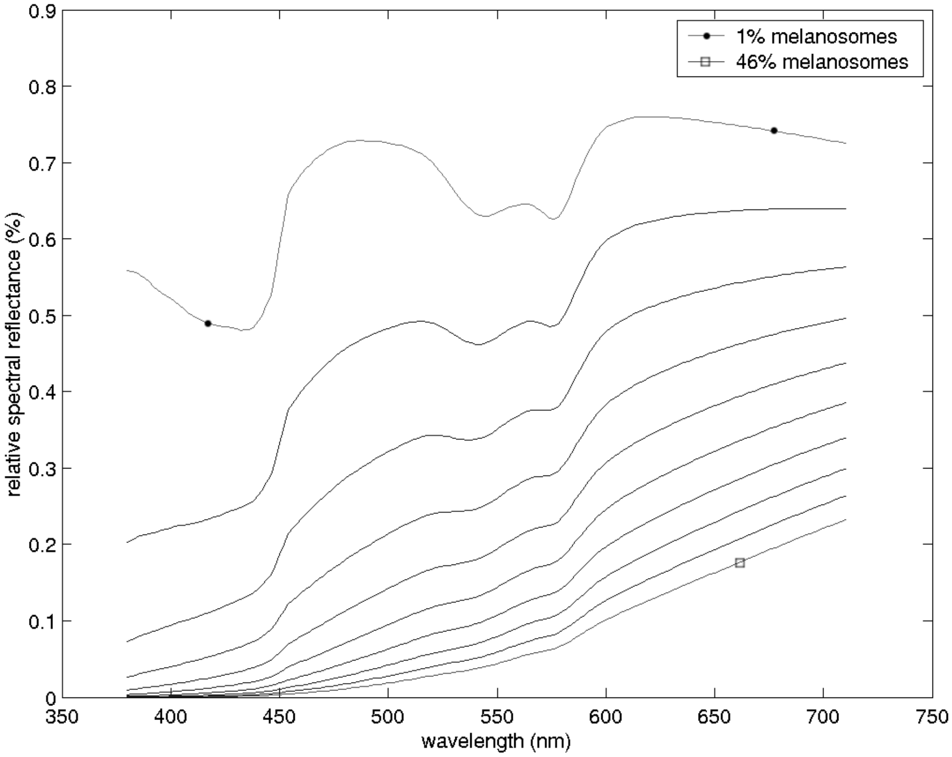

Figure 4.4: Variation of reflectance with melanin concentration. The black dots and empty square are simply used to distinguish the curves.

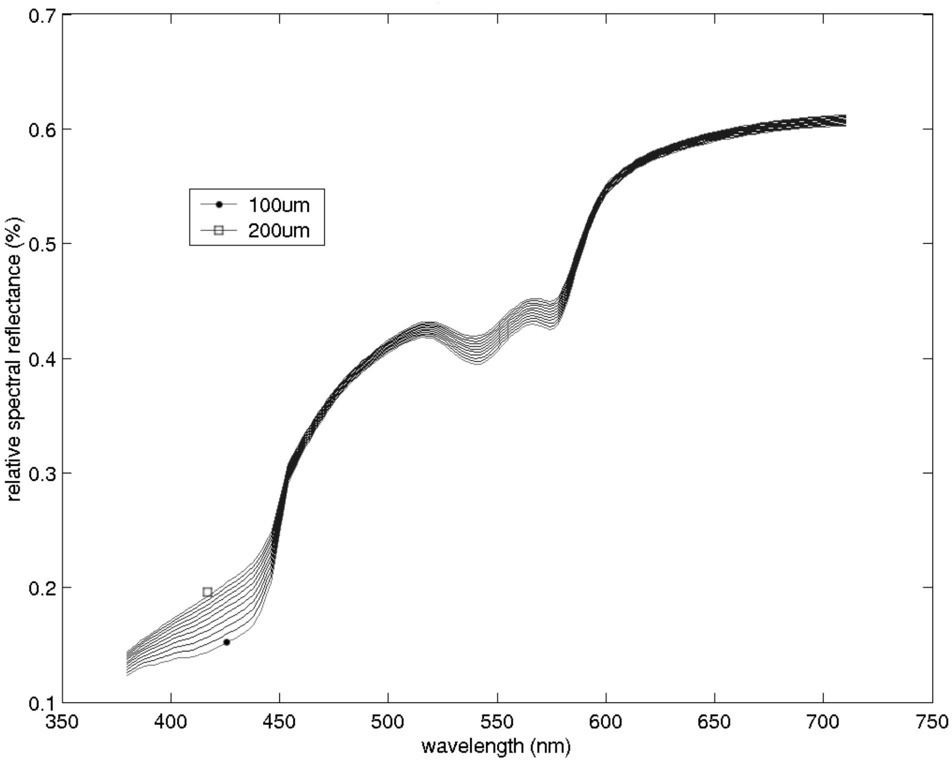

Figure 4.5: Variation of reflectance with papillary dermal thickness. The black dot and empty square are simply used to distinguish the curves.

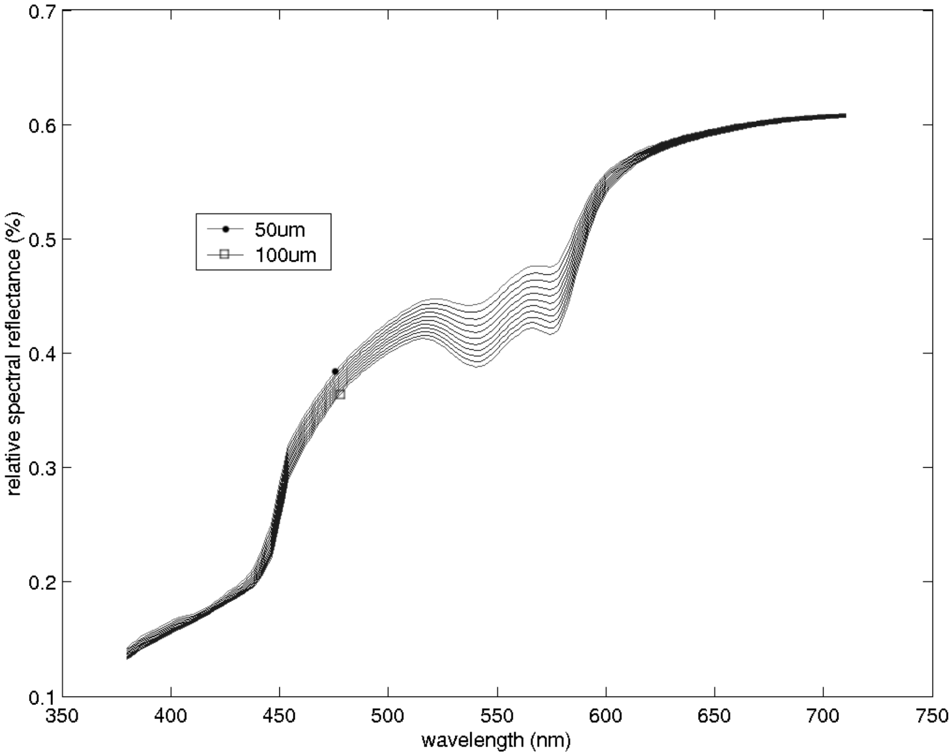

Figure 4.6: Variation of reflectance with superficial plexus thickness. The black dot and empty square are simply used to distinguish the curves.

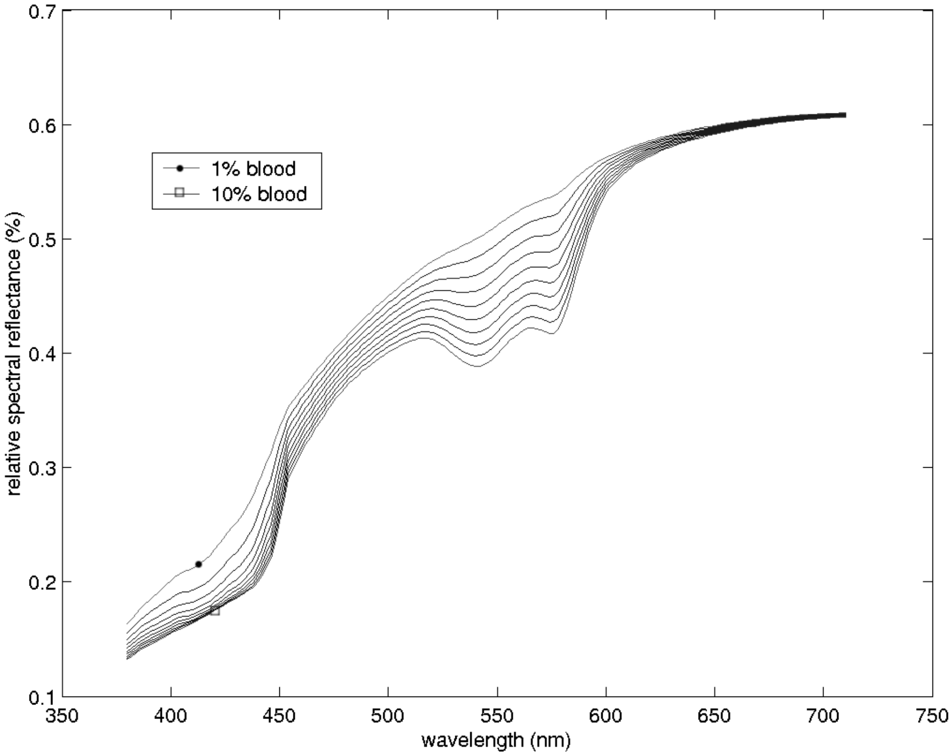

Figure 4.7: Variation of reflectance with hemoglobin concentration. The black dot and empty square are simply used to distinguish the curves.

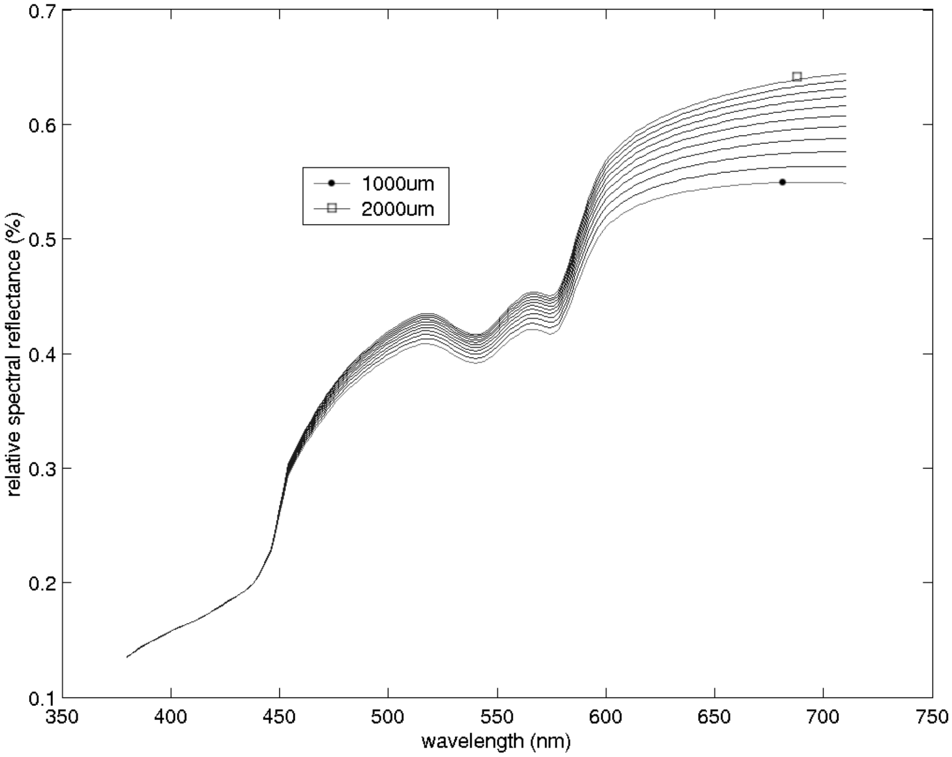

Figure 4.8: Variation of reflectance with reticular dermal thickness. The black dot and empty square are simply used to distinguish the curves.

spectral range	$380nm - 730nm$
resolution	$10nm$
modes	reflection, emission, transmission
measurement geometry	$45°/0°$ ring optic DIN 5033
measurement aperture	$4.5/8mm$
light source	gas filled tungsten, type A illumination
physical filters	D65 (approximated daylight), Po1 (polarised), No (neutral, incandescent lamp light A)
std. observer angles	$2°, 10°$

Table 4.1: Gretag Macbeth SpectroScan technical specifications.

the corresponding physiological parameters are varied. To test the model further we obtained the spectral reflectance of two skin areas — forehead, palm of the hand — from nine volunteer subjects: six light-skinned Caucasians, one dark-skinned African, and two dark-skinned Indians. The measurements were made using a Greytag Macbeth SpectroScan which gives reflectance spectra at $10nm$ intervals from $380nm$ to $710nm$. The technical specifications of the spectrophotometer are summarised in Table 4.1. Reflectances, averaged across subjects, are shown in Figure 4.9, together with curves produced by hand-fitting the model to each data set. The curves are absolute data, completely unscaled; the data are independent of the model, having played no role in model construction. Thus, this is a difficult test for the model, and the excellent agreement shown in the figure demonstrates conclusively the quality of the model's predictions for different races and body areas.

The parameters used to create the curves are shown in Table 4.2. Only the products of melanin and epidermal thickness, and of hemoglobin and plexus thickness appear in the model, so the fits actually have four free parameters. (Thicknesses were taken from physiological data, enabling us to get estimates of the volume fraction of pigments.) All the parameters given in the table are typical, increasing our confidence that the fits are not accidental.

We believe that these two tests show that the model fulfills the existential criteria described in Section 4.1.1. It is possible to achieve an adequate variety of skin reflectances; and the reflectances vary according to parameters that are easy to understand. The model successfully predicts reflectance spectra, which are both more difficult to predict and more useful than RGB values or rendered images.

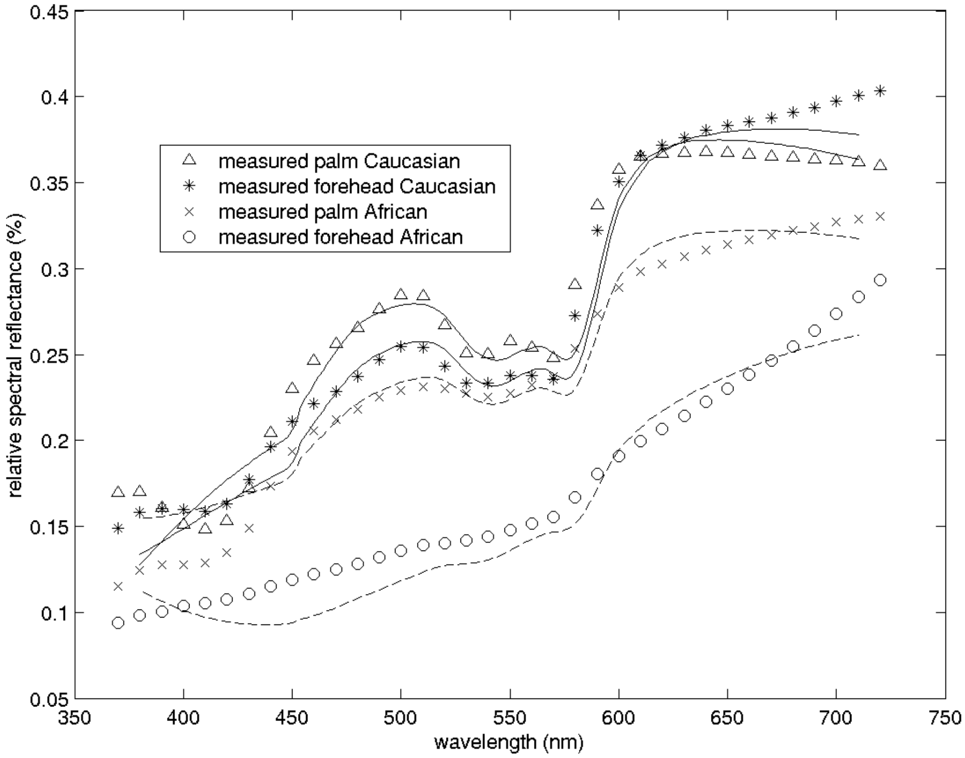

Figure 4.9: Comparison of model predictions to measured skin reflectance for two body areas of two racial groups. The model fits are indicated with a dashed line for dark skin and with a continuous line for white skin.

	Dark Forehead	Light Forehead	Dark Palm	Light Palm
Melanin (vf)	0.30	0.12	0.02	0.01
Epidermal thickness	50μ	50μ	400μ	400μ
Hemoglobin (vf)	0.10	0.10	0.10	0.10
Plexus thickness	275μ	275μ	275μ	275μ
Papillary dermis	150μ	200μ	150μ	150μ
Reticular dermis	300μ	375μ	250μ	300μ

Table 4.2: Parameters of calculated reflectances. ‘vf’ means volume fraction.

4.1.7 A Simple Implementation of the Simple Model

Any reflectance can be plotted as a point in an n-dimensional space, where n is the number of discrete wavelengths measured. So plotted, collections of related reflectances are frequently observed to lie within a low dimensional subset of the full n-dimensional space. When this occurs the set of reflectances can be economically stored and manipulated by re-parametrizing it using a set of basis vectors that spans the low dimensional space. Principal Components Analysis (PCA) or Singular Value Decomposition is the preferred analysis tool for finding such representations [132]. Given a set of multivariate measurements, the purpose of Principal Components Analysis is to find a smaller set of variables with less redundancy that would still give a good representation of the original data. In effect, PCA represents a large set of reflectance spectra, $R_i(\lambda)$, in terms of the basis vectors, $\rho_j(\lambda)$, that span the low dimensional space, with each reflectance represented by a set of coefficients, α_{ij}, one for each basis vector:

$$R_i(\lambda) \approx \sum_j \alpha_{ij} \rho_j(\lambda). \tag{4.13}$$

PCA finds sets of basis vectors and coefficients that optimize this approximation with respect to the Euclidean norm.

Earlier work [214] showed that measured skin reflectances from a racially homogeneous sample occupies a two-dimensional subspace, which was used to create a representation for modelling skin. Unfortunately, that research suffers from a limitation common to most PCA based on measured data: sampling bias. With a poorly defined universe of reflectances to model it is impossible to gauge how well the universe has been sampled. Avoiding the measurement approach we perform PCA on a set of data generated using our model. Here the sampling universe is well-defined: the set of reflectances generated by possible values of the physiological parameters that define the model. This approach is additionally attractive because non-uniform sampling of the physiological parameter space can be used to specialize the representation for particular skin types, and basic reflectances can be varied to use the representation for non-human characteristics, such as blood that uses copper-based analogues of hemoglobin.

Doing PCA on a 17,500 record data set produced by our model with a full range of physiologically valid parameters reveals the data to be well-represented by only three dimensions, which account for 95.74% of the variance. The eigenvalues of the spectral reflectance covariance matrix are shown in Figure 4.10 and the cumulative proportion rates of the principal components vectors are shown in Figure 4.11. The basis vectors are shown in Figure 4.12. Note that one reflectance shows the double minimum signature of hemoglobin, another shows the short wavelength minimum of melanin, and the third adjusts overall reflectance which is mediated by the thickness of the scattering layers. These features indicate which aspects of the skin colour change when colour is manipulated within this representation. This parametrization satisfies the second of our two existential objectives. The obvious computational efficiency of the linear representation satisfies another of our objectives.

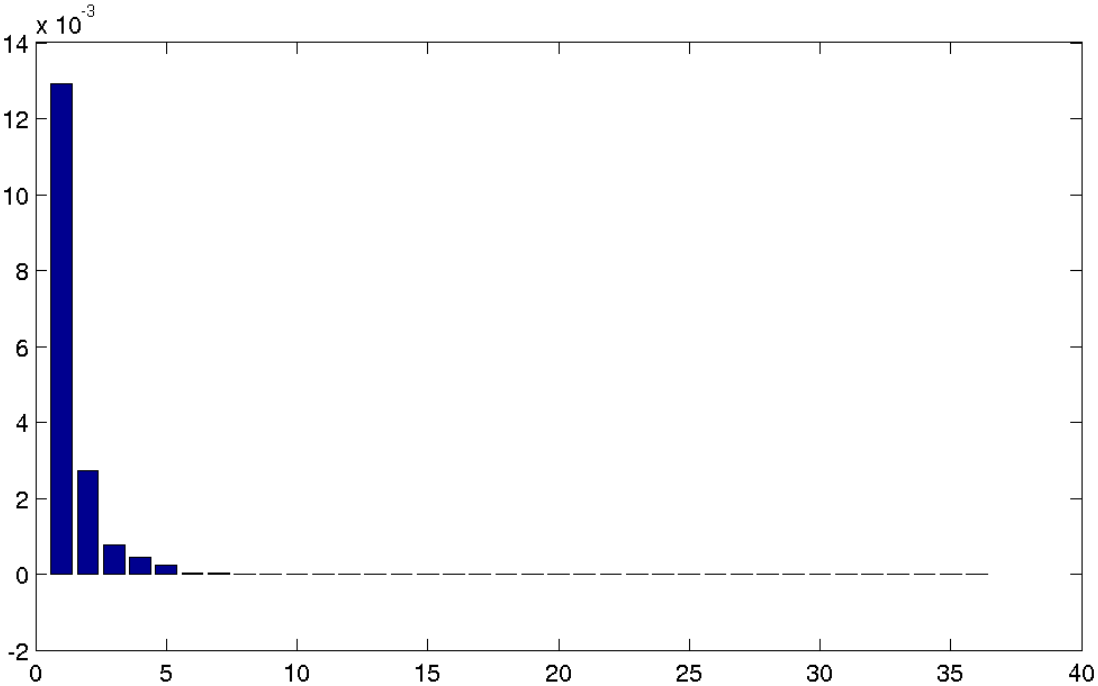

Figure 4.10: Eigenvalues of the spectral reflectance covariance matrix.

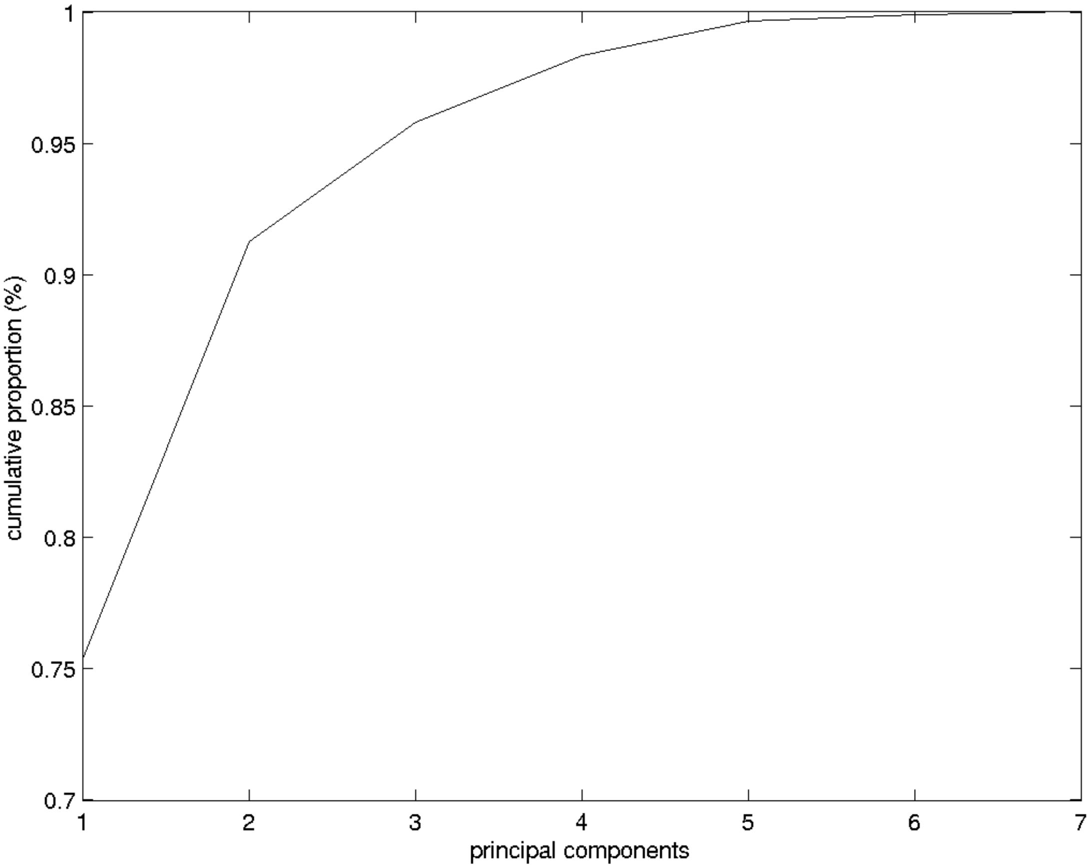

Figure 4.11: Cumulative proportion rates of the principal components vectors.

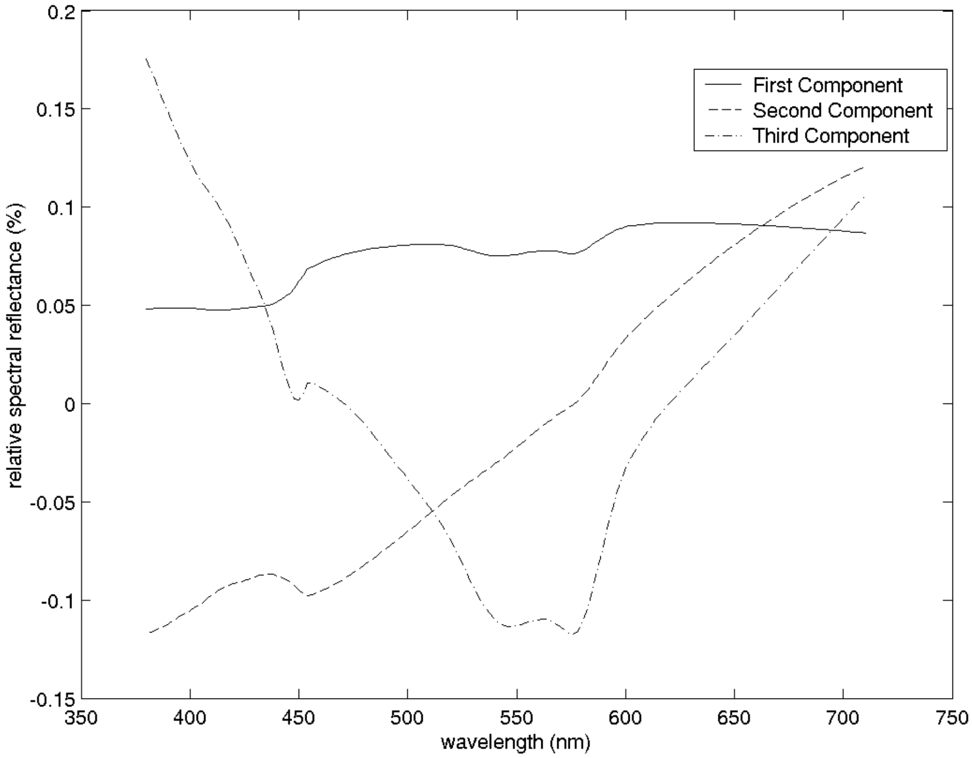

Figure 4.12: Reflectance basis functions for the linearized implementation of the model.

	α_1 (lightness)	α_2 (melanin)	α_3 (hemoglobin)
Dark Forehead	0.985	0.0832	0.0917
Light Forehead	1.642	0.0982	0.0962
Dark Palm	1.415	0.0423	0.0118
Light Palm	1.662	0.0181	0.0348

Table 4.3: Coefficient values of linear approximations.

4.1.8 Testing the Simple Implementation of the Simple Model

The implementation is tested by comparing it to the measurements described in Section 4.1.8. Each measured reflectance should be easily and accurately representable in terms of the linear model: that is, there should be a physiologically reasonable set of parameters that produces a reflectance that is well-matched to the measured reflectance. We also expect to understand the differences between skin from different body areas in terms of the parameters that represent that skin in the linear model. We find the relevant parameters by projecting the measured reflectances onto the three basis reflectances. Our first test projects all 18 measurements onto the basis vectors, calculates the approximate reflectance which is available in the linear representation, and compares the measured reflectance to the approximation. Because we wish the test to be illuminant-independent we compare using a Euclidean metric, not a colour difference metric. All 18 approximations match the corresponding measured reflectance very closely. The best match has an average error of 0.03%; the worst match has an average error of 0.14%. Given that the measured data are independent of the spectra used to create the model, this close agreement is very impressive. We then lumped the data across subjects, keeping data from different body parts separate and finding the best least squares fit. The approximate spectra along with the measured data are shown in Figure 4.13. The coefficients α_{ij} used to fit the data are shown in Table 4.3. Again, the agreement is impressive, showing that efficiency of calculation does not sacrifice either precision or range of applicability in the model.

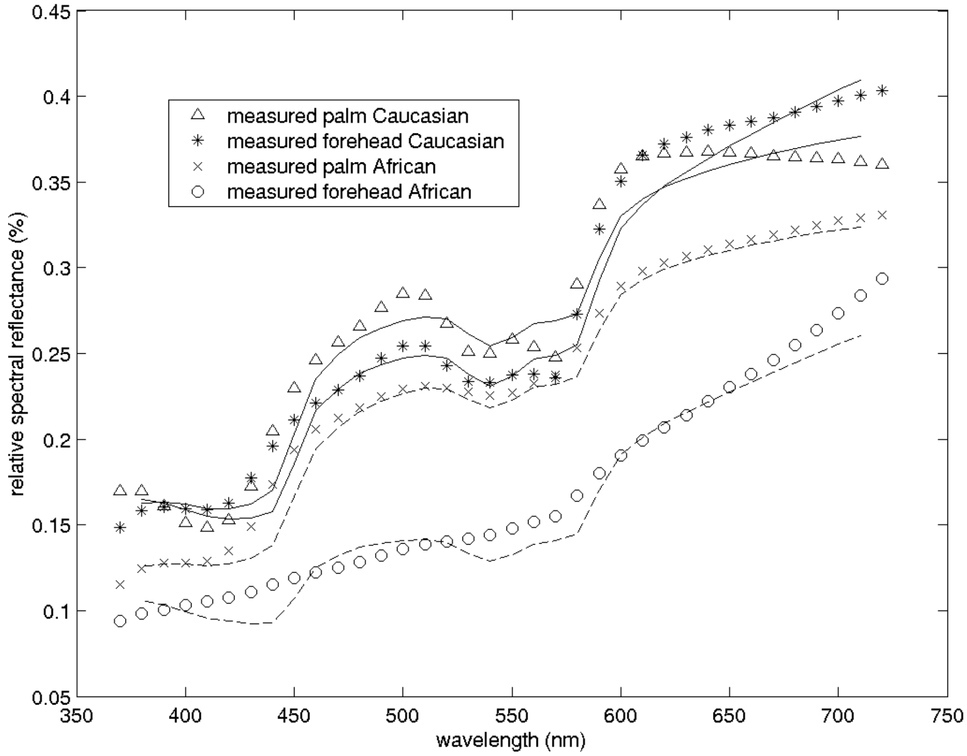

Figure 4.13: Linear approximations compared to measured skin reflectances. The approximations are indicated with a dashed line for dark skin and with a continuous line for white skin.

4.2 A System to Support Skin Rendering

Skin is a complex material and its reflectance is influenced by several phenomena. Our simple model for the reflectance of human skin is a first step in modelling and rendering skin. However, other “higher level” attributes of skin might be useful to model in order to render realistic-looking skin. The system we propose aims at providing artists with qualitative tools that will hopefully help them to model skin. The system is specifically designed for facial skin rendering, but can also render any type of human skin. We will however refer to facial rendering while discussing the various components of our system. We believe our system to be general enough to provide latitude and flexibility while at the same time providing specific tools for human skin rendering. The pipeline of our system is illustrated in Plate XIII. This system is certainly not a final word on tools for skin rendering. It is rather a prototype intended only as a proof of concept for skin rendering. Our simple skin reflectance model is one tool among many others that could exist in a skin rendering system.

One input to the system is a facial photograph of the subject. This image is decomposed into diffuse and specular reflectance images. These two images will be further modified and used as textures. Another input is the 3D mesh of the subject. All components that can be modified by the user are inside the red rectangle in Plate XIII. The specular image can be altered and will become the oiliness map (Section 4.2.5). The user provides a zone map that will eventually lead to the normal map (Section 4.2.6). The user also has control over several parameters, namely the pigmentation maps (Section 4.2.8), subsurface scattering (Section 4.2.2), asperity scattering (Section 4.2.3), blushing (Section 4.2.7), shadowing (Section 4.2.1), and hair (Section 4.2.4). Our system is well suited for real-time rendering with vertex and fragment shaders using multiple passes. Our current implementation uses a combination of *OpenGL* and Nvidia’s *Cg*. Accessibility shading, normal map generation, and pigment extraction are performed as pre-processing steps. For subsurface scattering, we currently use a variant of the Jensen and Buhler algorithm [96]. This algorithm is not real-time and is currently the bottleneck of our implementation. Several real-time subsurface scattering algorithms exist however, as was seen in Section 3.3. We are planning on incorporating translucent shadow maps [49] into our current implementation. All other components of the system were implemented as Cg shaders and perform in real-time. The various system components are discussed next.

4.2.1 Shadowing

Shadowing on the face can play an important role in rendering convincing human faces. In the case of real-time rendering, different techniques can be used to produce the shadows, such as shadow maps [230] and shadow volumes [31]. Our system provides a default shadow map in *OpenGL* that can be toggled on and off. To provide more control to the artist, we also experimented with the accessibility shading technique introduced by Miller [150]. Accessibility shading is a visibility technique that provides a measure of the accessibility of a point on a mesh in the form of how large a sphere can be extended at this point without intersecting the mesh. It only depends on the polygonal mesh used and does not depend on viewing or illumination directions. In facial rendering, this technique darkens some regions (especially around the eyes, underneath the nose, and in the crease of the mouth). The technique of horizon mapping [144] could also be used in place of accessibility shading. Figures 4.14 and 4.15 show the accessibility shading applied to a face model. Note that the noise present in the images is due to noise in the mesh itself generated by the acquisition process. Mesh smoothing techniques [58, 98] would significantly improve the results. The user has control on the amount of desired accessibility shading by varying the maximal sphere radius size in the accessibility shading algorithm [150].

4.2.2 Subsurface Scattering

Skin is a translucent material and it is assumed that a BSSRDF model can help capture some effects such as colour bleeding, light scattering back in the shadow terminator region, and a general softer appearance. These effects can be most readily observed on a face at the nose and the ears, and when the face is rendered and viewed at a high resolution. We implemented Jensen's BSSRDF model in software [96, 97] and the result is passed to the fragment program as a colour. We are planning on incorporating translucent shadow maps [49] into our current implementation. TSMs would provide the most visible qualitative effects of subsurface scattering in real-time. In

Figure 4.14: Example of accessibility shading applied to a face model.

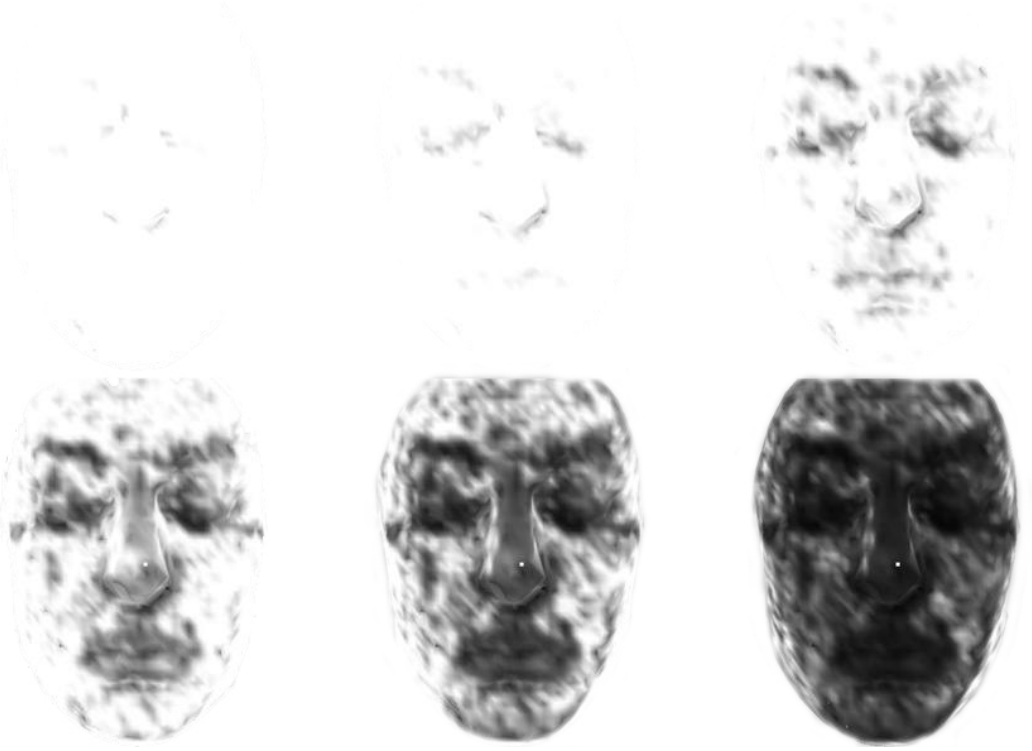

Figure 4.15: Varying the amount of accessibility shading.

practice, the model seems difficult to tweak and the effects are small for a typical head size. We used a kd-tree to speed-up the computations by only considering neighbours in the effective diffusion kernel in order of closest proximity. Jensen and Buhler use an octree with an error criterion (maximum solid angle spanned by the points in the voxel) to determine which voxels to use. The parameters for the diffusion subsurface scattering model are the relative refraction index, absorption coefficients, reduced scattering coefficients, subsurface diffuse colour, and the kd-tree kernel size. Absorption and scattering coefficients are specified as RGB triplets. Some interesting cartoon-like effects can be achieved when the BSSRDF model is used with extreme parameter values as demonstrated in Plate XVI. A shadow map is used in this image. Note the reddish appearance of the shadow terminator. The effect of subsurface scattering on a face is otherwise very subtle and could probably be modelled efficiently with a simple approximation [173]. This approximation would break in special cases, for example with strong back-lighting through the ears or with strong side lighting bleeding through the nose. Examples of translucency with front and side lighting are shown in Plates XIV and XV.

4.2.3 Asperity Scattering

Our asperity scattering shader is based on the work of Koenderink and Pont [115], described in Section 3.7. We have implemented the technique in a *Cg* fragment shader and experimented with several phase functions. The user can also specify a scattering layer thickness. The qualitative effect of asperity scattering is to provide a ‘halo’ effect when the light or view vector grazes the surface. Using a modified Fresnel coefficient can produce similar effects.

4.2.4 Hair

As seen in Chapter 2, hair follicles can be found over the entire body. Hair is an integral part of skin and we assume that it can add realism to skin imagery. There are many publications dealing with hair and fur. Our application currently uses the Kajiya-Kay reflectance model for hair shading [101]. Hair shading is handled by a *Cg* fragment program. The basic equation for the Kajiya-Kay reflectance model is

$$f_d = \sin(T, S)\ k_d, \tag{4.14}$$

$$f_s = ((T \cdot S)(T \cdot V) + \sin(T, S)\sin(T, V))^n k_s, \tag{4.15}$$

where

S = light source vector,

V = view vector,

T = hair tangent vector,

k_d = hair diffuse coefficient,

k_s = hair specular coefficient,

n = specular exponent, and

$\sin(A, B) = \sqrt{1\ -\ (A \cdot B)^2}$.

Besides the particular reflectance of hair, geometric parameters are used to control the overall hair appearance. These geometric parameters are:

1. hair local density (from user supplied hair density map),
2. number of segments or control points,
3. maximum length of hair,
4. hair radius,
5. perturbation (hair is assumed to grow in the normal direction and can be perturbed).

Gravitational force can also be applied to the hair to make it look more realistic. Figures 4.16 to 4.18 show the hair geometry and the results of modifying some of the hair parameters. Plate XVIII shows several hair examples produced by our system and Plates XIX and XX show some beard examples.

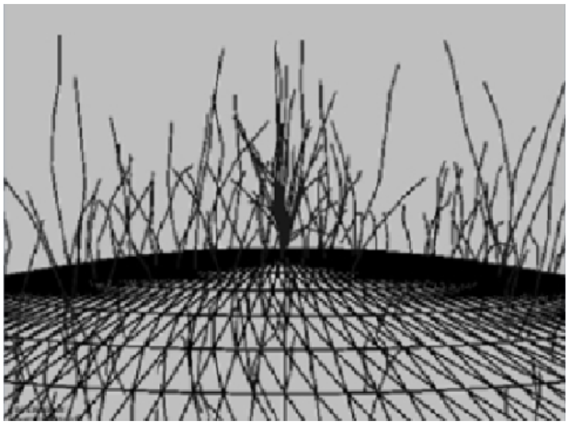

Figure 4.16: Close-up of hair geometry.

4.2.5 Oiliness

The specular highlights on the face can be affected by sebum and perspiration. The current implementation of our software allows the artist to draw an oiliness map that specifies the location of sebum and perspiration zones. It also provides functionality to increase or decrease the overall specularity with a single slider. This is accomplished by simply thresholding the luminance of the oiliness map. A painting interface allows the user to tweak the generated oiliness map by adding and removing oiliness in desired areas. Examples of generated oiliness maps are shown in Figure 4.19 where skin is more specular in darker regions.

4.2.6 Skin Meso-structure

Bump map generation is currently derived from a photograph and re-touched by an artist in an image manipulation software. We would also like to provide the user with automatic procedural bump map generation for various zones of the face. This could be particularly useful for imaginary characters. We have experimented with Voronoi diagram bump maps, Worley cellular bump maps, and noise functions (Section 3.6). We believe that an extensive statistical analysis of various skin images from different zones of the body could reveal important features of skin meso-geometry. Clearly, skin surface details vary spatially, as seen in Plate X. Procedural texture generation

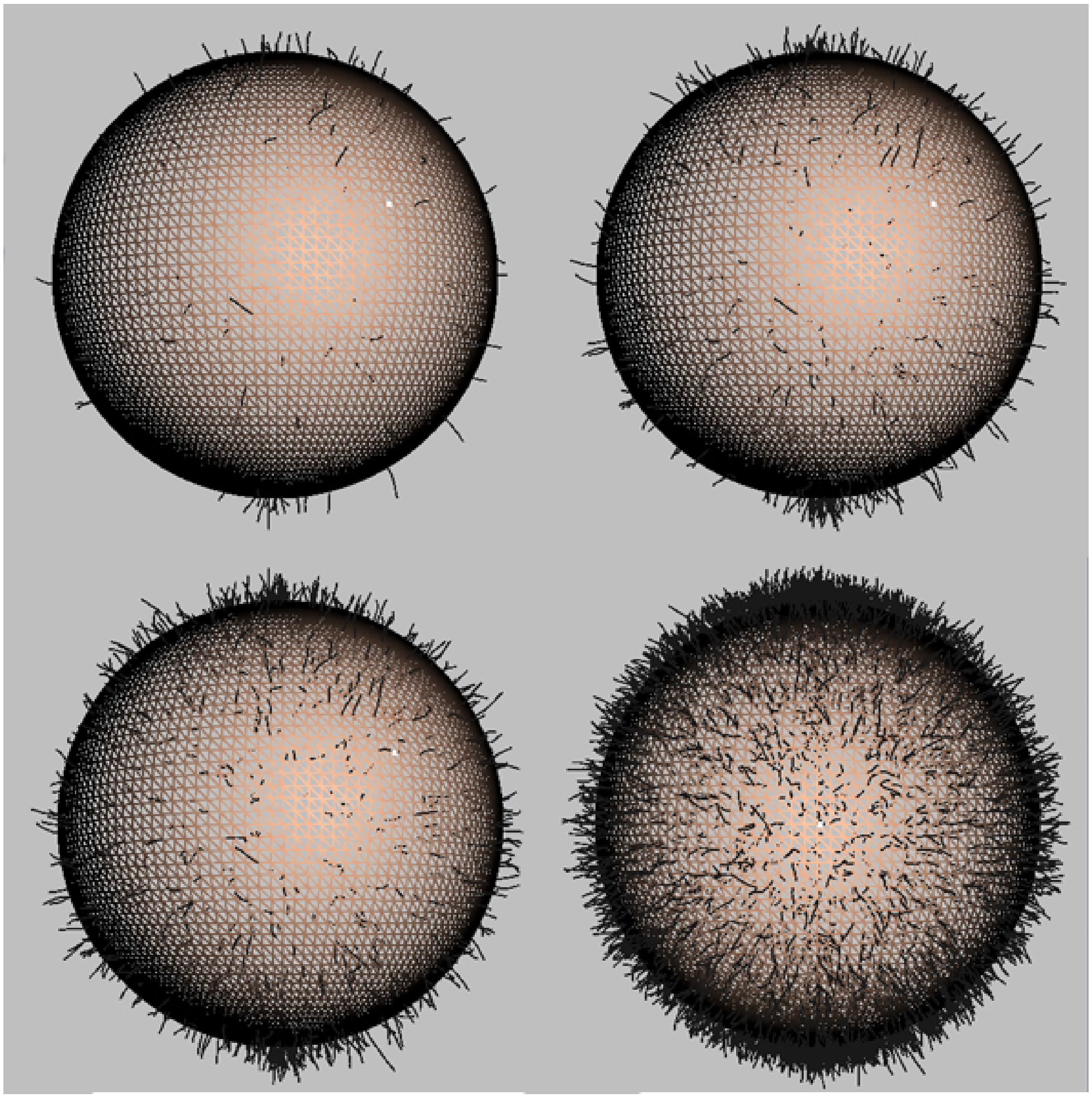

Figure 4.17: Varying the hair density.

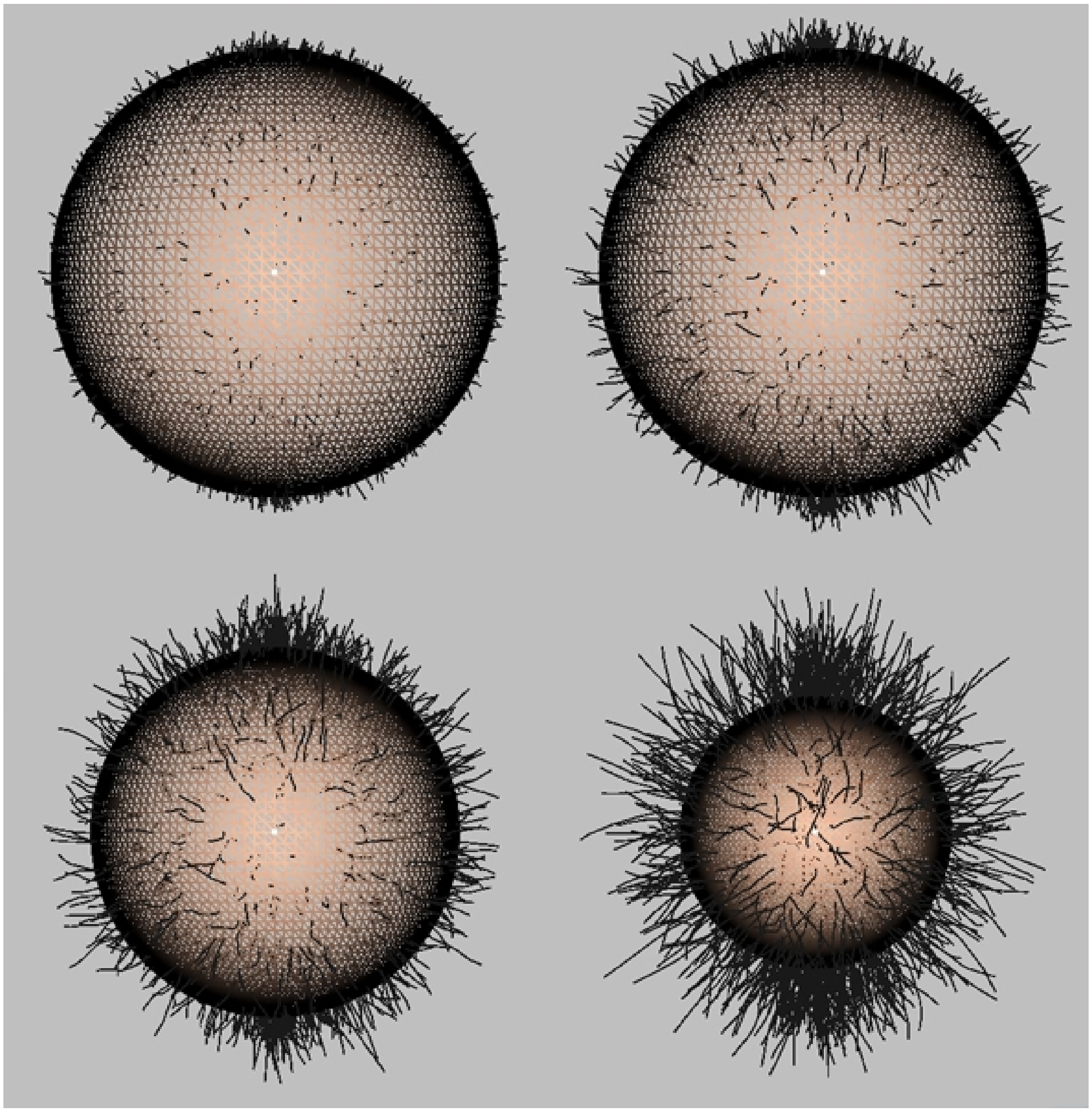

Figure 4.18: Varying the hair length.

Figure 4.19: Examples of oiliness maps for two different models.

algorithms could therefore be adapted. We are planning to provide our system with a user-supplied zone map that will delineate various zones on the face. A different algorithm could then be used to generate the meso-geometry for each zone. A painting interface could also be provided for touch-ups. Making sure that the different patches blend without visible artifacts is a stimulating problem. An approach similar to Haro *et al.* [76] could be used. A more elegant solution would also probably be possible thanks to the procedural nature of the generative algorithms.

4.2.7 Blushing

Colour changes can occur in skin due to constriction or dilatation of blood vessels. This can be caused by emotions, physical activity, temperature, etc. We provide the artist with tools to modify the face coloration. Pigment segmentation can provide general coloration modification but lacks user control. We experimented with a very simple technique [172] that gives a bit more control over the areas we want the blushing to occur (Section D.2). The user selects central points on the model and a Phong-like shading is used to create a blushing area around the selected points. The parameters to control the blushing effect are a blush colour and attenuation. The blushing technique is illustrated in Plates XXI and XXII. Instead of using a simple Phong-like shading for blushing, we can also use our skin reflectance model along with a texture map representing the volume fraction of blood at each pixel. It is therefore possible to manipulate the volume fraction of blood in the superficial plexus at a particular location (Section 4.1). The initial texture map containing the blood concentrations is computed following Tsumura *et al.* [214] (Section 4.2.8). Instead of being acquired from a photograph, the texture map could also be painted by an artist. We are then able to modify non-linearly the hemoglobin quantities in a user-specified area to simulate blushing. Extensive testing will however have to be conducted in order to determine the most effective tools for skin colour manipulation.

4.2.8 Skin Pigment Extraction

We extract our pigmentation maps following Tsumura *et al.* [88, 211, 212, 213, 214] using Independent Components Analysis (ICA) [86, 183] on a single skin image to extract relative quantities of pigments (see Section D.2). Independent Component Analysis is a statistical and computational technique used in blind source separation (BSS) problems. ICA defines a generative model for the observed multivariate data, which is typically given as a large database of samples. In the model, the data variables are assumed to be linear or nonlinear mixtures of some unknown latent variables, and the mixing system is also unknown. The latent variables are assumed non-Gaussian and mutually independent, and they are called the independent components of the observed data. These independent components, also called sources or factors, can be found by ICA. The basic noise-free model assumes a linear mixing generative model. The total pixel radiance is divided into three components: $R_0(\lambda)$, $R_1(\lambda)$, and $R_2(\lambda)$, as shown in Figure 4.1. $R_0(\lambda)$ represents the surface reflection, light that interacts with hair, and any noise in the data. $R_1(\lambda)$ represents the light that interacts with melanin chromophores, and $R_2(\lambda)$ represents the light that interacts with melanin, oxy- and deoxy-hemoglobin. Examples of extracted pigment maps from various photographs are shown in Plate XXIII. We are planning on using our simple skin reflectance model to perform pigment extraction. This would provide a more rigorous and biologically valid basis than using a purely statistical technique such as Independent Component Analysis. Also, using ICA only yields relative pigment quantities, whereas our skin reflectance model could in theory provide absolute values.

Chapter 5

Discussion and Future Work

First, we provide a very simple physiologically-based model of skin reflectance, suitable for computer graphics. The strength of the model is that it works for a wide range of body areas and skin types, it exhibits good precision, and it supports an efficient implementation. Furthermore it is parametrized in terms of parameters intuitive enough for an artist or a physiological simulation to use. The model predicts reflectances because illumination variation of skin colour is very important. However, deriving RGB reflectances or illuminated RGB colours from the model is straightforward. The implementation uses simple arithmetic operations that can easily be implemented in a modern graphics processing unit for very high on-line throughput. Each parameter of the model — concentration of melanin, concentration of blood, and thicknesses of the different skin layers — can be stored per texel in a texture map. The artist can thus easily modify the parameters locally. We believe that our model could be used in many applications such as image synthesis, skin detection in computer vision, skin pigment extraction, etc.

There are several interesting ways in which the model and implementation could be extended. Most obviously, for applications that require more precision the number of basis vectors can be increased, which is easy in our formalism. The linear basis functions can also be rotated to bring them closer to an optimal parametrization. For human modellers, optimal is defined by extensive interface experimentation. For whole body simulation, an adequately detailed physiological model must be developed. Then, experimental calibration of the linear model will be needed to join the physiologies. Also the model might incorporate a scattering model like [174] to produce a BRDF of comparable precision. For this extension the skin model needs to include a fluid surface layer to model accumulated sebum, sweat, or other fluids. A similar extension of the model would make it possible to add cosmetics to skin. It goes without saying that any such extension of the model should be accompanied by extensive testing of the results against measured skin colours. The more a model tries to predict, the more testing it needs to be believable.

Second, we develop a system to support skin modelling and rendering. The system is still in its infancy but it already supports features that are helpful for human skin rendering. Extensive user testing will have to be performed in order to better assess the different system features. We believe that it is however a first step towards providing efficient high-level tools for artists, tools that are specifically tailored for skin rendering. Our simple skin model is one tool among many that provides a strong physiological basis to our modelling interface, an easy and intuitive parametrization, reflectance spectra instead of tristimulus values, and finally computational efficiency that allows real-time rendering.

The current system already provides useful tools to artists but could be improved in many ways. Shadowing on the face is employed but we believe that more elaborate photographic lighting tools could be provided by allowing key, fill, and rim lights to be positioned in order to better light the skin. For facial rendering, semi-automatic texture mapping from photographs could be a very practical addition to the system [207]. The diffusion approximation can model some of the qualitative effects of subsurface rendering. We are however investigating other ways to mimic these effects and better predict the final results. This can be achieved for example by allowing the artist to modify the size of the shadow boundary region or its colour. Our simple skin reflectance model can be used in this region to increase the quantity of blood and thus to give a reddish appearance to the shadow terminator. Modelling hairs at the skin surface now allows us to generate a beard, but we would also like to develop a more extensive asperity scattering model at the skin surface. Skin meso-geometry is an interesting area of research and we are investigating procedural approaches to generate and render different skin features distinguishables at scales of a few millimetres. The use of a cosmetics layer in our simple reflectance model of skin would also require specific tools and user interfaces in order to simulate the real techniques employed by make-up artists. Finally, we are investigating the potential use of our simple skin model to perform pigment quantities extraction from photographs. The current approaches often use statistical techniques, like Independent Components Analysis, to extract an estimate of the quantities of skin pigments at a pixel location in an image [212, 214]. We believe that our simple skin reflectance model could provide a more physiologically valid basis to perform such pigment extractions.

Appendix A

Preliminaries

A.1 Basic Radiometry Concepts

Radiometry is the measurement of optical radiation, which is electro-magnetic radiation within the frequency range between 3×10^{11} and 3×10^{16} Hz, namely the ultraviolet, the visible, and the infrared. Photometry is the measurement of light, which is defined as electro-magnetic radiation which is detectable by the human eye. It is concerned with the visible spectrum of light, e.g., wavelengths between $360 - 830$ nm. Photometry is analogous to radiometry except that all quantities are weighted by the spectral response of the human eye. We do not use any photometry concept in this dissertation.

The quantities used in radiometry are :

Energy Q $(Joules\ J)$: Light is a form of energy measured in Joules.

Energy Density w (J/m^3) : Energy per unit volume, dQ/dV.

Radiant Flux or Power Φ $(Watt\,W\ or\ Joules/sec.)$: Total amount of energy passing through a surface or region of space per unit time, dQ/dt.

Irradiance or Flux Density E (W/m^2) : Power per unit area incident from all directions in a hemisphere onto a surface that coincides with the base of that hemisphere, $d\Phi/dA$.

Radiant Exitance or Radiosity M (W/m^2) : Power per unit area leaving a surface into a hemisphere whose base is that surface, $d\Phi/dA$.

Radiant Intensity I (W/sr) : Power per unit solid angle, $d\Phi/d\omega$.

Radiance L $(W/m^2\ sr)$: Power per unit projected area per unit solid angle.

We will assume that geometrical optics is an adequate basis for the description of light and light scattering. We make the following assumptions on the behaviour of light:

- Linearity : If two sources of light A and B are used to illuminate some optical system, then the output from that system due to A + B is the sum of the outputs due to A and B individually.
- Energy conservation : Reflected radiant exitance is never greater than the incident irradiance.
- No polarisation.
- No diffraction and interference.
- No fluorescence or phosphorescence.
- Steady state and infinite speed.

A.2 Bidirectional Surface Scattering Reflectance Distribution Function (BSSRDF)

For non-metallic materials, light arriving at a surface enters the material and then scatters inside it before leaving the surface at a different location. This is described by the bidirectional surface scattering reflectance distribution function (BSSRDF) [161]. The BSSRDF S relates the differential reflected radiance dL_o at exitant location x_o in direction ω_o to the differential incident flux

$d\Phi_i$ at incident location x_i from direction ω_i

$$S(x_i, \omega_i; x_o, \omega_o) = \frac{dL_o(x_o, \omega_o)}{d\Phi_i(x_i, \omega_i)}. \tag{A.1}$$

Note that all reflectance functions described in this section are dependent on the wavelength λ. All notation used omits this parameter and the dependence is always assumed implicitly. The amount of radiance leaving a point x_o due to subsurface scattering can be expressed as

$$L_o(x_o, \omega_o) = \int_A \int_\Omega S(x_i, \omega_i; x_o, \omega_o) L_i(x_i, \omega_i)(n_i \cdot \omega_i) d\omega_i dA(x_i), \tag{A.2}$$

where the term $S(x_i, \omega_i; x_o, \omega_o)$ in Equation A.2 is the bidirectional surface scattering reflectance distribution function. The BSSRDF is an eight-dimensional function and is costly to evaluate. Many authors have noted that single scattering accounts for a small percentage of the total outgoing radiance in highly scattering materials. In this context, the relationship between incoming and outgoing directions can be removed, simplifying the BSSRDF to a four-dimensional function $R_d(x_i, x_o)$ known as the diffuse BSSRDF.

A.3 Bidirectional Reflectance Distribution Function (BRDF)

When the flow of light hits the surface of an object, the energy is partly absorbed by the material and partly scattered back in the environment. The ratio of light scattered back in the environment and its directional distribution depend on the surface material properties.

The bidirectional reflectance distribution function (BRDF) [161] is defined as the differential reflected radiance in the outgoing direction per differential incident irradiance in the incoming direction. It is a way of describing how incoming light at a surface is reflected back toward the viewer. The BRDF is an approximation of the more general BSSRDF. In the case of the BRDF, it is assumed that light striking a surface location is reflected at that same surface location. This reduces the BRDF to a six-dimensional function

$$f_r(\theta_i, \phi_i; \theta_o, \phi_o) = \frac{dL_o(\theta_o, \phi_o)}{dE_i(\theta_i, \phi_i)}. \tag{A.3}$$

For physical accuracy, the BRDF must ensure the Helmholtz law of reciprocity:

$$f_r(\omega_i \ \rightarrow \omega_o) = f_r(\omega_o \ \rightarrow \omega_i).$$

A.4 Bidirectional Transmittance Distribution Function (BTDF)

The bidirectional transmittance distribution function (BTDF) is defined to the differential transmitted radiance in the outgoing direction per differential incident irradiance in the incoming direction. It is a way of describing how incoming light at a surface is transmitted through a transparent or translucent layer:

$$f_t(\theta_i, \phi_i; \theta_t, \phi_t) \equiv \frac{L_t(\theta_t, \phi_t)}{L_i(\theta_i, \phi_i) \cos\theta_i d\omega_i}. \tag{A.4}$$

A.5 Bidirectional Texture Function (BTF)

The bidirectional texture function (BTF) [50, 47] is a spatially varying bidirectional reflectance distribution function (BRDF). It is used to characterise a surface at a fine scale where surface variations produce local intensity variations. The BRDF is used at a coarser scale where local surface variations are sub-pixel and local intensity is uniform. Analogous to the BRDF, the BTF is a function of four independent angles. Spatial variations are achieved by adding a texture coordinate (u, v) in the description of the BTF.

A.6 Local Illumination Models

The use of a bidirectional reflectance distribution function (BRDF) to represent a surface reflectance suffers from numerous acquisition, storage, and representation problems that make it sometimes impractical for some applications. Analytic reflectance models were developed to palliate those problems. Local illumination models allow to characterise the shading of a point on a surface according to the position and colour of the light sources, the eye position, and the surface orientation and properties. These models can be categorised into empirical models and more physically-based models. The empirical models were developed based on qualitative observations and have the advantages of simple and intuitive parameters, ease of implementation, and efficiency. Such models include the Phong [34], Blinn [25], and Strauss [200] models, and are still widely used today in computer graphics. Local illumination models usually distinguish between diffuse and specular reflections.

Specular or surface reflectance takes place at the interface between two media with different refractive indices. Much work has been done in computer graphics to model accurately specular reflections from first principles. The Torrance-Sparrow micro-facet model [210] was introduced to computer graphics by Blinn [26] and Cook and Torrance [43]. This model uses a geometry shadowing term along with a Fresnel term. Probably the most comprehensive model introduced in computer graphics today is the model by He *et al.* [78]. Anisotropic specular reflection is also handled by several authors [36, 177, 223], and multiple scattering from complex micro-scale geometries by Westin *et al.* [226]. Diffraction effects have been investigated by Stam [198]. Other researchers have investigated compact ways to represent BRDF data, such as the works of Lafortune et al. [124] and Koenderink and Van Doorn [116].

Diffuse or body reflectance is due to multiple subsurface scattering of light within the material. Different materials absorb and scatter light at different wavelengths and thus characterise the diffuse reflected light colour. Much less work has been done on diffuse reflection, often been modelled in computer graphics using Lambert's law. This law states that exiting radiance is isotropic and proportional to the surface irradiance. This in turns depends on the cosine of the angle of incidence of light with the surface normal. In the case of subsurface scattering, the light's entry point in the material is usually different from the exit point. Multiple scattering events tend to make this exit point random and create isotropic reflectance. However, there exist few perfectly isotropic diffuse surfaces, and using Lambert's Cosine law to account for diffuse reflection is most of the time not physically valid. Oren and Nayar [157, 170] develop a comprehensive model that predicts accurately body reflectance from rough surfaces. While the brightness of a Lambertian surface is independent of viewing direction, they found that the brightness of a rough surface increases as the viewing direction approaches the light source direction. They also use a microfacet model with V-cavities [210], and assume that each facet has a Lambertian diffuse reflectance. They found that the overall surface is non-Lambertian due to facet foreshortening. Their model accounts for effects of masking, self-shadowing, and inter-reflections. The overall qualitative effect of the Oren-Nayar model is to make objects look more flat than with the standard Lambertian model. Subsurface scattering is discussed in more details in Section 3.1. Lu et al. [115, 128] noticed that a velvet cylinder exhibits a reflectance that is almost the reciprocal of what the Lambertian model predicts. This phenomenon is due to the light scattering by a multitude of small hair fibres that compose velvet and is discussed in Section 3.7 on asperity scattering.

A.7 Snell's Law

Snell's law (also called Descartes' law) gives the relationship between angles of incidence and refraction for light impinging on an interface between two media with different indices of refraction, shown in Figure A.1. The law follows from the boundary condition that a light wave is continuous across a boundary, which requires that the phase of the wave be constant on any given plane, resulting in

$$\eta_i(\lambda) sin\theta_i = \eta_t(\lambda) sin\theta_t, \tag{A.5}$$

where

η_i : index of refraction of outer media at wavelength λ,

η_t : index of refraction of inner media at wavelength λ,

θ_i : angle from the normal of the incident wave, and

θ_t : angle from the normal of the refracted wave.

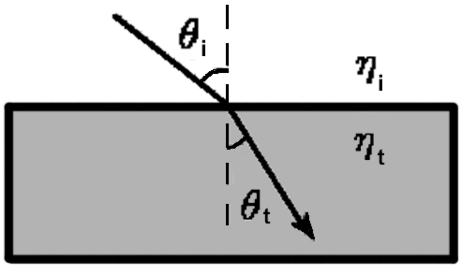

Figure A.1: Snell's Law.

The refractive index is the ratio of the speed of light in a vacuum to the speed of light in a given medium, namely

$$\eta(\lambda) = \frac{c}{\nu_\lambda}, \tag{A.6}$$

where

ν_λ : velocity of light of wavelength λ in the medium, and

c : speed of light in a vacuum.

A.8 Fresnel Equations

Fresnel's equations describe the reflection and transmission of electro-magnetic waves at an interface. If we assume a planar surface, then the radiance reflected from and transmitted across the plane is given by the Fresnel coefficients, the reflection and transmission coefficients for waves parallel and perpendicular to the plane of incidence. For a dielectric medium, Snell's Law can be employed to relate the incident and transmitted angles. The qualitative effect of Fresnel reflection is to augment surface reflection as the incident light direction grazes the surface. The Fresnel coefficients are

$$R_\perp = -\frac{\sin(\theta_i - \theta_t)}{\sin(\theta_i + \theta_t)}, \tag{A.7}$$

$$T_\perp = \frac{2\sin\theta_t\cos\theta_i}{\sin(\theta_i + \theta_t)}, \tag{A.8}$$

$$R_\parallel = \frac{\sin\theta_t\cos\theta_t - \sin\theta_i\cos\theta_i}{\sin\theta_i\cos\theta_i + \sin\theta_t\cos\theta_t}, \tag{A.9}$$

$$T_\parallel = \frac{2\sin\theta_t\cos\theta_i}{\sin(\theta_i + \theta_t)\cos(\theta_i - \theta_t)}. \tag{A.10}$$

Note that these coefficients are fractional amplitudes, and must be squared to get fractional intensities for reflection and transmission. If the incident light is unpolarised, the Fresnel reflectance is thus

$$F_r = \frac{1}{2}(R_\perp^2 + R_\parallel^2), \tag{A.11}$$

and the Fresnel transmittance F_t in terms of F_r is

$$F_t = \left((1 - F_r)\left(\frac{\eta_t}{\eta_i}\right)\right)^2. \tag{A.12}$$

When the light is at near-normal incidence to the interface ($\theta_i \approx \theta_t \approx 0$), the Fresnel reflectance is approximated by

$$F_r = \left(\frac{\eta_i - \eta_t}{\eta_i + \eta_t}\right)^2. \tag{A.13}$$

Schlick [190] provides a good and fast approximation to Fresnel equations.

A.9 Beer's Law

Beer's law (sometimes called Lambert-Beer law) states that the absorbance $A(\lambda)$ of a species at a particular electro-magnetic radiation λ is proportional to the concentration c of the absorbing species and to the length of the path b of the electro-magnetic radiation through the sample containing the absorbing species:

$$A(\lambda) = a(\lambda)bc, \tag{A.14}$$

where

$a(\lambda)$: absorptivity of the species at wavelength λ,

b : path length of the electro-magnetic radiation through the sample, and

c : concentration of the absorbing species.

The absorptivity is called the molar absorptivity (denoted ϵ) if the concentration is measured in moles/litre. Molar absorptivity has units of $Lmol^{-1}cm^{-1}$. The absorptivity is simply a measure of the amount of light absorbed per unit concentration and is sometimes called the extinction coefficient.

Transmittance T is defined as the fraction of light intensity that passes through the sample. The percent transmittance $\%T$ is simply defined as

$$\%T = 100\ I_t/I_i, \tag{A.15}$$

where

I_t : transmitted light intensity, and

I_i : incoming light intensity.

Since the amount of radiation absorbed can vary over an extremely wide range, absorbance is defined logarithmically. Absorbance is defined in term of transmittance as follows:

$$A(\lambda) = -\log T \tag{A.16}$$

or in term of percent transmission:

$$A(\lambda) = \log(100/\%T) = 2.000 - \log(\%T). \tag{A.17}$$

The wavelength at which the absorptivity is maximal is called the analytical wavelength of the substance.

A.10 Light Reflection and Transmission

Reflected Radiance

Surface radiance can be categorised into specular, diffuse, mixed, retro-reflection, and gloss [68]. The reflected radiance L_r from a surface has two components: surface reflectance and subsurface reflectance:

$$L_r(\theta_r, \phi_r) = L_{r,s}(\theta_r, \phi_r) + L_{r,v}(\theta_r, \phi_r), \tag{A.18}$$

where

$L_{r,s}$: reflected radiance due to surface scattering

$L_{r,v}$: reflected radiance due to subsurface scattering.

The reflection vector, $\hat{R}$, can be easily computed and is equal to $2(\hat{I} \cdot \hat{N})\hat{N} \; - \; \hat{I}$, where $\hat{I}$ is the illumination vector and $\hat{N}$ is the surface normal vector.

Transmitted Radiance

Transmitted radiance can be categorised into specular, diffuse, and mixed [68]. The transmitted radiance into the layer, L_t, also has two components: reduced intensity or attenuation and radiance due to volume scattering.

The reduced intensity is the amount of transmitted light through the layer without scattering inside it, but accounting for absorption. It is given by Beer's Law (Section A.9). The absorption coefficient σ_a describes how light is absorbed as it passes through the layer. After travelling some distance d, $e^{-\sigma_a d}$ of the light remains. Given a ray entering a volume of thickness z, $e^{-\sigma_a z/|\cos\theta|}$ of the light remains when it exits the layer, as illustrated in Figure A.2.

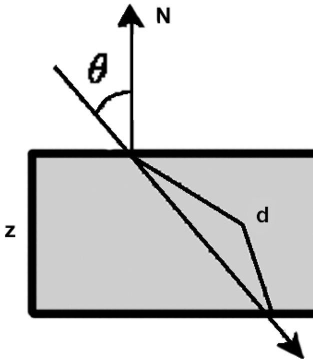

Figure A.2: Reduced intensity through a layer of thickness z.

The radiance due to scattering in the layer is modelled using phase functions to describe the results of light interacting with particles in the layer (Section A.11). The transmitted radiance is thus

$$L_t(\theta_t, \phi_t) = L_{ri}(\theta_t, \phi_t) + L_{t,v}(\theta_t, \phi_t), \tag{A.19}$$

where

L_{ri} : reduced intensity, and

$L_{t,v}$: transmitted radiance due to volume or subsurface scattering.

Since the reflected light L_r and the transmitted light L_t were separated into two components each, the BRDF and the BTDF also are separated into two components

$$f_r = f_{r,s} + f_{r,v}, \tag{A.20}$$

and

$$f_t = f_{ri} + f_{t,v}. \tag{A.21}$$

The relative contributions of the surface and subsurface terms are modulated by the Fresnel coefficients (Section A.8):

$$f_r = R f_{r,s} + T f_{r,v} = R f_{r,s} + (1 - R) f_{r,v}. \tag{A.22}$$

The transmission vector, $\hat{T}$, is derived by Heckbert [79]. It is equal to

$$-\frac{\eta_i}{\eta_t}\hat{I} \ + \ \hat{N}\left(\frac{\eta_i}{\eta_t}\cos\theta_i \ - \ \sqrt{1 \ - \ \left(\frac{\eta_i}{\eta_t}\right)^2 \ (1 \ - \ \cos^2\theta_i)}\right), \tag{A.23}$$

where $\hat{I}$ is the illumination vector, $\hat{N}$ is the surface normal vector, and θ_i is the angle of incidence (Figure A.2).

Single Scattering Approximation

It is possible to obtain a closed form expression for f_r and f_t if we only consider single scattering events. In this case, the BRDF that describes single scattering from a medium is [118]

$$f_r(\omega_i \to \omega_o) = \frac{a\ p(\omega_i, \omega_o) e^{-d(\frac{1}{\omega_i \cdot N} + \frac{1}{\omega_o \cdot N})}}{((\omega_i \cdot N) + (\omega_o \cdot N))}, \tag{A.24}$$

and the BTDF is [118]

$$f_t(\omega_i \to \omega_o) = \frac{a\ p(\omega_i, \omega_o)(e^{-\frac{d}{\omega_o \cdot N}} + e^{-\frac{d}{\omega_i \cdot N}})}{(\omega_o \cdot N) - (\omega_i \cdot N)}, \tag{A.25}$$

where

$a = \sigma_s/\sigma_a$: scattering albedo,

d : layer thickness,

$r \ll \lambda$	Atmospheric absorption
$r < \lambda$	Rayleigh scattering
$r \approx \lambda$	Mie scattering
$r \gg \lambda$	Geometrical optics

Table A.1: Criterion for phase function selection (data from Glassner [68]).

N : surface normal, and

$p(\omega_i, \omega_o)$: phase function.

A.11 Phase Functions

A phase function or scattering function describes the scattered distribution of light after a ray hits a particle in a layer. The layer is composed of a medium with particles in suspension within it. It is often assumed that the particles are uniformly distributed within the medium and that both the medium and particles are independently homogeneous. Phase functions are in general four-dimensional functions of the incoming and outgoing directions $p(\omega_i, \omega_o)$. For particles that are randomly oriented, the phase function can be reduced to a function of the phase angle between the two directions, $p(\cos\alpha) = p(\omega_i \cdot \omega_o)$. See Glassner [68] for a good survey of some phase functions commonly used in computer graphics. The choice of a particular phase function is usually determined by the ratio of the particle size to the wavelength of the light involved. It is important for skin since the collagen fibres of the papillary dermis are different in structure and size than that of the reticular dermis, for example. Table A.1 shows the selection criterion of a phase function by comparing the average radius of the particles with wavelength.

Rayleigh Phase Function

The Rayleigh phase function is used when the particle radius is somewhat smaller then the wavelength of light. Klassen [112] suggests that Rayleigh scattering should be used when $\frac{r}{\lambda} < 0.05$. Rayleigh scattering can model the scattering behaviour of cigarette smoke and dust. For skin, Rayleigh scattering is used to model the scattering of light by small-scale collagen structures in the dermis (Section 2.2.6).

The Rayleigh phase function is

$$P_{Rayleigh}(\cos\alpha) = \frac{3}{4}\ (1\ +\ (\cos\alpha)^2). \tag{A.26}$$

Mie Phase Function

The Mie phase function is used when the particles radius is comparable to the wavelength of light. Mie scattering can model the scattering behaviour of water droplets or fog. For skin, Mie scattering is used to model the scattering of longer wavelengths in the dermis (Section 2.2.6). Nishita *et al.* [163] propose two approximations for Mie scattering. The first one, *hazy Mie*, is used when the particle density is sparse. The second one, *murky Mie*, is used when the particle density is high.

The hazy Mie and murky Mie approximations are

$$P_{hazyMie}(\cos\alpha) = 1\ +\ 9\left(\frac{1+\cos\alpha}{2}\right)^{8}, \tag{A.27}$$

and

$$P_{murkyMie}(\cos\alpha) = 1\ +\ 50\left(\frac{1+\cos\alpha}{2}\right)^{32}. \tag{A.28}$$

Henyey-Greenstein Phase Function

Another Mie scattering approximation is the Henyey-Greenstein phase function [81]. It is very commonly used in computer graphics [26]. It takes an asymmetry parameter g, the mean cosine of the phase function, which goes from strong retro-reflection ($g = -1$) to strong forward scattering ($g = 1$). Isotropic scattering is achieved when $g = 0$.

The Henyey-Greenstein phase function is

$$P_{Henyey-Greenstein}(\cos\alpha, g) = \frac{1-g^2}{(1+g^2-2g\cos\alpha)^{3/2}}. \tag{A.29}$$

Function	r	g_1	g_2
Rayleigh	0.50	-0.46	0.46
Hazy Mie	0.12	-0.50	0.70
Murky Mie	0.19	-0.65	0.91

Table A.2: Parameter values of the Schlick phase function to approximate Rayleigh and Mie scattering (data from Blasi *et al.* [24]).

Schlick Phase Function

Schlick [189, 24] develops a model that can approximate both Rayleigh and Mie scatterings. The Schlick phase function uses a blending parameter r to blend two ellipses together and an asymmetry parameter g similar to the one used in the Henyey-Greenstein phase function. The Schlick phase function is

$$P_{Schlick}(\cos\alpha, r, g_1, g_2) = r\varphi(\cos\alpha, g_1) \ + \ (1-r)\varphi(\cos\alpha, g_2), \tag{A.30}$$

where $r \ \in]-1, 1[$ and

$$\varphi(\cos\alpha, g) = \frac{1-g^2}{(1-g\cos\alpha)^2}. \tag{A.31}$$

The values of r, g_1, and g_2 used to match the Rayleigh and Mie scattering functions are shown in Table A.2.

A.12 The Kubelka-Munk Model

The Kubelka-Munk model [120, 121, 122] is an early attempt to model the appearance of layered surfaces. It considers the problem of determining the resulting overall colour from a set of layers of differently coloured paint. The model makes a number of assumptions in order to obtain an analytical solution:

- Particles are small in comparison to the material thickness,
- The composition of each layer is homogeneous (uniform colour and scattering properties),

- The top layer is irradiated by incident light uniformly from all directions and light exiting each layer after scattering is also uniformly distributed.

These assumptions limit the model for physically-based rendering. Uniform incident illumination is rare in practice and uniform exiting distribution is a good approximation only for highly scattering media. Cotton and Claridge [46] however claim that the Kubelka-Munk model can be a good approximation in the case of skin (Section 3.1). Haase and Meyer [72] introduce the Kubelka-Munk model in computer graphics for rendering pigmented materials and Pharr use it in a skin shader [173]. The Kubelka-Munk model parameters are

- d : Depth of the layer,
- $\sigma_a(\lambda)$: Attenuation or absorption cross section of the layer at a particular wavelength, and
- $\sigma_s(\lambda)$: Scattering cross section of the layer at a particular wavelength.

For a single layer, the reflection coefficient R and the transmission coefficient T of the layer are given by the Kubelka-Munk equations:

$$R(\beta, K, d, \lambda) = \frac{(1-\beta^2)(e^{Kd} - e^{-Kd})}{(1+\beta)^2 e^{Kd} - (1-\beta)^2 e^{-Kd}}, \tag{A.32}$$

and

$$T(\beta, K, d, \lambda) = \frac{4\beta}{(1+\beta)^2 e^{Kd} - (1-\beta)^2 e^{-Kd}}, \tag{A.33}$$

where
$s = 2\sigma_s(\lambda)$,
$K = \sqrt{k(k+2s)}$,
$\beta = \sqrt{\frac{k}{k+2s}}$, and
$k = 2\sigma_a(\lambda)$.

Note that the Kubelka-Munk equations are wavelength-dependent. It is possible to derive equations for multiple layers by considering all possible scattering interactions between the layers.

Also, specular base layers can be approximated by treating the base layer specular component as a diffuse coefficient, assuming the top layer has no specular contribution. The roughness parameter of the base surface can be modified by the ratio of the new specular component to its original value. This approximates the diffusion of specular highlights from the base surface [173].

Appendix B

Mixed Scattering and Absorption

The analysis in this dissertation assumes that the different tissues either scatter light or absorb it, which greatly simplifies the equations of the skin model presented here. This simplification is not necessary; this appendix shows how to extend the model to include both scattering and absorption in each component of the skin.

To include absorption in the Kubelka-Munk model of scattering, an extra process must be considered. In addition to the scattering terms there is an absorption term $K\Delta x$, which gives the fraction of light that is absorbed as it passes through the thin slice. The basic equations describing a slice then become

$$j_T = i_T - (S+K)\Delta x i_T + S\Delta x j_R,$$

and

$$i_R = j_R - (S+K)\Delta x j_R + S\Delta x i_T.$$

These lead directly to the generalized differential equations,

$$j_T{}'(x) = (S+K)j_T(x) - Sj_R(x),$$

and

$$j_R{}'(x) = S j_T(x) - (S+K) j_R(x).$$

Using Section 4.1.3 $\sigma(x)$ and $\rho(x)$ gives the simplified equations

$$\sigma'(x) = K\rho(x),$$

and

$$\rho'(x) = (2S+K)\sigma(x).$$

These two equations combine to give the second order equation

$$\sigma''(x) = K(2S+K)\sigma(x),$$

which solves to

$$\sigma(x) = AKe^{\beta x} + BKe^{-\beta x}$$

and

$$\rho(x) = A\beta e^{\beta x} - B\beta e^{-\beta x},$$

where we have defined

$$\beta^2 = K(2S+K).$$

It is now necessary to solve for A and B in terms of the boundary cases $j_T(x_1) = I_T$ and $j_R(x_1) = J_R$. The algebra is not difficult, but is rather tedious. It can be made a bit simpler by solving for each boundary case individually, and then adding the solutions. For example,

$$I_T = j_T(x_1) = \frac{1}{2}(\rho(x_1) + \sigma(x_1)) = \frac{1}{2}A_I(K+\beta)e^{\beta x_1} + \frac{1}{2}B_I(K-\beta)e^{-\beta x_1}$$

and

$$0 = j_R(x_0) = \frac{1}{2}(\rho(x_0) - \sigma(x_0)) = \frac{1}{2}A_I(K-\beta)e^{\beta x_0} - \frac{1}{2}B_I(K+\beta)e^{-\beta x_0}.$$

From the second equation

$$B_I = A_I\frac{K-\beta}{K+\beta}e^{2\beta x_0},$$

and when we substitute it into the first equation we get

$$A_I = \frac{2(K+\beta)e^{\beta x_1}}{(K+\beta)^2e^{2\beta x_1} + (K-\beta)^2e^{2\beta x_0}}I_T,$$

and

$$B_I = \frac{2(K-\beta)e^{-\beta x_1}}{(K+\beta)^2e^{-2\beta x_0} + (K-\beta)^2e^{-2\beta x_1}}I_T.$$

We now do the same thing with J_R.

$$0 = \frac{1}{2}A_J(K+\beta)e^{\beta x_1} + \frac{1}{2}B_J(K-\beta)e^{-\beta x_1},$$

and

$$J_R = \frac{1}{2}A_J(K-\beta)e^{\beta x_0} - \frac{1}{2}B_J(K+\beta)e^{-\beta x_0}.$$

Then,

$$B_J = -A_J \frac{K+\beta}{K-\beta} e^{2\beta x_1},$$

$$A_J = \frac{2(K-\beta)e^{\beta x_0}}{(K+\beta)^2 e^{2\beta x_1} + (K-\beta)^2 e^{2\beta x_0}} J_R,$$

and

$$B_J = \frac{2(K+\beta)e^{-\beta x_0}}{(K+\beta)^2 e^{-2\beta x_0} + (K-\beta)^2 e^{-2\beta x_1}} J_R.$$

The parameters of the general solution are then $A = A_I + A_J$ and $B = B_I + B_J$. We use them to solve for $j_R(x)$ and $j_T(x)$ as follows:

$$j_R(x) = \frac{1}{2}(\rho(x) - \sigma(x)) = \frac{1}{2}A(K-\beta)e^{\beta x} - \frac{1}{2}B(K+\beta)e^{-\beta x},$$

and

$$j_T(x) = \frac{1}{2}(\rho(x) + \sigma(x)) = \frac{1}{2}A(K+\beta)e^{\beta x} + \frac{1}{2}B(K-\beta)e^{-\beta x}.$$

As above it is possible to calculate these functions as the sum of two parts, one due to I_T, and one due to J_R. The first part is

$$j_{RI}(x) = I_T \left(\left(\frac{K-\beta}{K+\beta} \right) \frac{e^{-\beta(x_1-x)}}{1+\gamma^2} + \left(\frac{K+\beta}{K-\beta} \right) \frac{e^{\beta(x_1-x)}}{1+\gamma^{-2}} \right)$$

and

$$j_{TI}(x) = I_T \left(\frac{e^{-\beta(x_1-x)}}{1+\gamma^2} + \frac{e^{\beta(x_1-x)}}{1+\gamma^{-2}} \right)$$

where

$$\gamma = \frac{K-\beta}{K+\beta} e^{-\beta(x_1 - x_0)}.$$

Sanity Check

To make sure that the solution makes sense we will inspect the limit $S \to 0$, where the result should be Beer's Law. In this limit $\beta = K$. Now calculating,

$$j_T(x) = \frac{1}{2}(\rho(x) + \sigma(x)) = \frac{1}{2} A_I (K+\beta) e^{\beta x} = I_T e^{-K(x_1 - x)},$$

and

$$j_R(x) = \frac{1}{2}(\rho(x) - \sigma(x)) = \frac{1}{2} B_J (K+\beta) e^{-\beta x} = J_R e^{-K(x - x_0)},$$

as expected.

Appendix C

Multi-component Materials

Appendix B develops the solution of materials composed of a single component. Skin components, such as the epidermis, actually consist of more than one component: melanosomes and basic epidermal tissue for example in the case of epidermis. The Kubelka-Munk model for multi-component materials treats the components as if they are homogeneously mixed at the length scales where light absorption and scattering. In this appendix we develop the model for two components, noting that it is easily generalized to more than two components. The model concentrates on a very small slice of the material, which is divided into two sub-slices. One sub-slice, the upper one in Figure C.1, contains the first component, which has scattering coefficient S_1 and absorption component K_1. The other sub-slice, the lower one in the figure, contains the second component, which has scattering coefficient S_2 and absorption component K_2. The thickness of the complete slice is Δx; the thickness of the upper sub-slice is $c_1 \Delta x$, where c_1 is the volume fraction of component 1; the thickness of the lower sub-slice is $c_2 \Delta x$, where c_2 is the volume fraction of component 2. We now consider light passing through the top and bottom of the slice, and through the division between the sub-slices.

As illustrated in Figure C.1, light passes two ways at each boundary. For example, at the upper boundary light flux i_T passes downward and light flux i_R passes upward. We can easily see that two fluxes, i_T and j_R, are determined by processes external to the slice. The following four equations describe those four light fluxes:

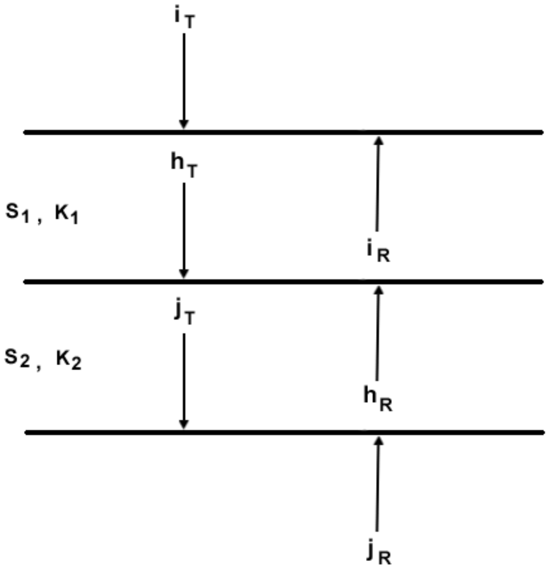

Figure C.1: Skin reflectance model for multi-component materials.

$$j_T = h_T - S_2c_2\Delta x h_T - K_2c_2\Delta x h_T + S_2c_2\Delta x j_R;$$

$$h_T = i_T - S_1c_1\Delta x i_T - K_1c_1\Delta x i_T + S_1c_1\Delta x h_R;$$

$$h_R = j_R - S_2c_2\Delta x j_R - K_2c_2\Delta x j_R + S_2c_2\Delta x h_T;$$

and

$$i_R = h_R - S_1c_1\Delta x h_R - K_1c_1\Delta x h_R + S_1c_1\Delta x i_T.$$

We now turn these into a pair of differential equations. First eliminate h_T and h_R to get the pair of equations

$$i_R = \frac{(1-S_1-K_1)(1-S_2-K_2)}{1-S_1S_2} j_R + \left(\frac{S_2(1-S_1-K_1)^2}{1-S_1S_2} + S_1\right) i_T$$

and

$$j_T = \frac{(1 - S_1 - K_1)(1 - S_2 - K_2)}{1 - S_1 S_2} i_T + \left(\frac{S_1(1 - S_2 - K_2)^2}{1 - S_1 S_2} + S_2 \right) j_R,$$

where the concentrations and distances have been omitted for simplicity. Now, define $j_T(x)$ as the downward directed flux at position x, and $j_R(x)$ as the upward directed flux at position x. Then, $j_T = j_T(x)$ and $i_T = j_T(x + \Delta x)$ for a slice positioned at x. Similar relations hold for the upward directed flux. We are going to let the thickness of the slice go to zero ($\Delta x \to 0$), so we can linearize the above two equations, keeping only terms that are linear in Δx. The resulting equations are

$$j_R(x + \Delta x) = j_R(x) - (S_1 c_1 + K_1 c_1 + S_2 c_2 + K_2 c_2)\Delta x j_R(x) - (S_1 c_1 + S_1 c_1)\Delta x j_T(x),$$

and

$$j_T(x) = j_T(x + \Delta x) - (S_1 c_1 + K_1 c_1 + S_2 c_2 + K_2 c_2)\Delta x j_T(x) + (S_1 c_1 + S_1 c_1)\Delta x j_R(x).$$

In the limit these become the differential equations

$${j_R}'(x) = -(S_1 c_1 + K_1 c_1 + S_2 c_2 + K_2 c_2) j_R(x) - (S_1 c_1 + S_1 c_1) j_T(x)$$

and

$${j_T}'(x) = (S_1 c_1 + K_1 c_1 + S_2 c_2 + K_2 c_2) j_T(x) - (S_1 c_1 + S_1 c_1) j_R(x).$$

Note that if we make the substitutions $S \to S_1 c_1 + S_2 c_2$ and $K \to K_1 c_1 + K_2 c_2$ these differential equations are identical to the ones solved in Appendix A. Thus, we can use the solutions provided there with more complex definitions of coefficients. The development in this appendix limits itself to a two component system. It is quite clear that generalization to a multi-component system is straightforward.

Appendix D

Digital Cosmetics for Computer Graphics

D.1 Why Cosmetics in Computer Graphics?

We have witnessed in recent years an emergence of entirely computer-generated films and animations. Some of those adopt a non-photorealistic artistic approach for their rendering [69, 201], whereas some attempt more photorealistic effects. One such example is the movie *Final Fantasy: The Spirits Within*. Even though it was not a commercial success, it is nonetheless considered as a landmark in the realm of computer-generated films. Such large projects are usually decomposed into different modules during the creation process. Examples of such modules include modelling (further divided into background and main characters), lighting, motion capture, animation, texturing, etc. In fact the development cycle of a computer-generated film closely mimics the one employed in traditional film media.

Computer graphics is used in most Hollywood productions in a way or another. We can anticipate that this percentage will grow and that an increasing number of productions will be entirely computer-generated. Creation modules in those productions will probably be even more specialised and reflect in many ways the more traditional creation pipeline. We could envision computer graphics hair stylists, makeup artists, costume designers, etc. This trend was reflected recently in an ACM SIGGRAPH 2002 paper dealing with hair styling and modelling [111] and in an ACM UIST 2002 paper on clothing manipulation [87].

We believe that digital makeup artists could be used in CG productions in the future and believe in providing tools for them that reflect as much as possible the way traditional makeup artists work. Research in skin rendering for computer graphics is very dynamic and has evolved significantly in the recent years. We suggest to build on this to provide new and useful tools for CG artists.

Digital cosmetics would not only be useful for film and animation. It could be used in many different media such as virtual reality, gaming industry, advertisement, simulations, fashion industry, and cosmetology. Virtual humans are used increasingly in many sectors of our society. Some artists already use makeup in their CG characters but we can guess that the process involved is not optimised and could benefit from digital makeup tools and techniques. One such artist that uses makeup very successfully in his CG faces is Steven Stahlberg [196]. Moreover, international modelling agencies, such as the famous Elite modelling agency, offer CG models to their customers [99] and digital makeup could be a very viable idea for these products. Two books by editor Taschen on female digital characters were also recently published [228, 229]. Animator Robert Baldwin, whose past projects include *Roughnecks: Starship Trooper Chronicles* believes digital animation is not yet sophisticated enough to replace expert makeup [154]. Research in digital makeup could palliate this problem and provide better tools to allow artists to express their creativity and push the boundary of what is currently possible in computer graphics.

D.2 Previous Work in Digital Cosmetics

Digital cosmetics have been investigated by some researchers [165, 166, 167, 192, 205]. Most of this work is used in analysing and quantifying the impact of cosmetic products on skin. The purpose of makeup is to alter skin reflectance properties and skin cosmetic products are clearly designed to modify the optical properties of skin in different ways. Fatty creams for example aim at minimising the effect of scattering by the superficial layer of the epidermis, which consists of dead and flaky skin cells that produce a dry look. Products like face powders have the opposite effect. When a powder is applied sparingly and not rubbed into the skin (to be attached to the downy hairs would be ideal), asperity scattering is enhanced and results in a “softer” look [115].

Limited work has been done directly on makeup reflectance in computer graphics. Song *et al.* [194] have measured the BRDF of a ball with make-up applied and re-mapped the reflectance function to other objects such as a human face. Marschner *et al.* [140] attempted to measure skin BRDF with Cover Girl replenishing (soft beige) makeup and found no significant difference with the untreated skin BRDF for the examined subject. They suggested further study of artificial modification of skin reflectance, including other forms of makeup: powder, theatrical makeup, etc. Boissieux *et al.* [28] modelled skin aging and wrinkles for computer graphics with target applications in cosmetology. Maggi Hairstyles and Cosmetics [4] is a shareware computer program that attempts to allow the creation of various hairstyles and cosmetics. Patel [172] investigated coloration issues in computer generated facial animation. He uses a simple Phong-related model to procedurally generate blushing on the cheeks [172]. He simulates eyeshadow makeup with the same technique. Other researchers have also considered the relationships between emotions and skin colour [103, 129].

Takemae *et al.* [206] trained a neural network to evaluate subjectively human skin surface condition based on evaluations provided by cosmeticians. Unlearned images are then evaluated by the system and results are compared with the cosmeticians’ evaluations. The goal is in effect to obtain information on the patient’s skin surface in order to propose adapted cosmetic products. In the learning phase, the cosmeticians’ subjective evaluations of skin together with extracted skin image features are the inputs of the neural network. The subjective evaluation is based on terms or qualities employed generally by cosmeticians, such as “dark”, “gloss”, “transparency”, etc. Examples of image features used are the rate of high frequency component, rate of specular reflection component, variance of hue, saturation, intensity, etc.

Tsumura *et al.* [214] propose an E-cosmetic function for skin reproduction that was derived using physiologically-based image processing. First, the original image is divided into body reflection and surface reflection. Shading is removed on the face using a colour vector space analysis as a simple inverse lighting technique. Once the shading has been removed, the extraction of hemoglobin and melanin components is performed by independent component analysis. Pigment information is recorded from a single skin colour image.

Let

$$\begin{aligned} c(x,y) &= \text{compound colour vector of the shading-removed pixel } x,y, \\ s_1(x,y) &= \text{quantity of hemoglobin pigment at pixel } x,y, \\ s_2(x,y) &= \text{quantity of melanin pigment at pixel } x,y, \\ a_1 &= \text{pure colour vector of hemoglobin / unit quantity, and} \\ a_2 &= \text{pure colour vector of melanin / unit quantity.} \end{aligned}$$

Then it is assumed that

$$c(x,y) = s_1(x,y)a_1 + s_2(x,y)a_2, \tag{D.1}$$

or

$$c(x,y) = As(x,y) \text{ in matrix form.} \tag{D.2}$$

In general, the extracted independent vector $e(x,y)$ is given by:

$$e(x,y) = Hc(x,y), \tag{D.3}$$

and

$$e(x,y) = R\Lambda s(x,y), \tag{D.4}$$

where

$$\begin{aligned}
H &= [h_1, h_2] \text{ separation matrix },\\
e(x, y) &= [e_1(x, y), e_2(x, y)]^t \text{ extracted signal vector},\\
R &= \text{ permutation matrix},\\
\Lambda &= \text{ diagonal matrix that relates the absolute quantities to relative quantities.}
\end{aligned}$$

Substituting Equations D.2 and D.3 into Equation D.4 we obtain

$$HAs(x, y) = R\Lambda s(x, y). \tag{D.5}$$

Thus, the mixing matrix A is

$$A = H^{-1}R\Lambda. \tag{D.6}$$

The authors specify that in practice the permutation and scaling matrices do not influence the results and are set to identity, e.g., $A = H^{-1}$. Once the mixing matrix A is obtained, an analysis step on the image can extract the relative quantities $s(x, y)$ by applying A^{-1} to the observed signals $c(x, y)$. New images can be generated by modifying the relative quantities of the pigments, by applying A to $s(x, y)$ in Equation D.2. Several experiments are performed to validate the technique. The proposed technique can realistically synthesize the increase of hemoglobin pigments due to alcohol consumption and the increase of melanin pigments due to tanning.

For realistic synthesis of skin colour and texture, the amount of pigment should be changed spatially in a nonlinear fashion. It is very difficult to obtain the parameters for a skin model such as skin depth, scattering coefficients, densities of pigments, etc., using an image-based technique. Reproduced skin colour and texture depends on imaging devices, illuminants, and environments. Scattering in the skin is modelled using a linear approximation based on a modified Lambert-Beer law. Using this model in conjunction with Independent Component Analysis, it is possible

Skin Type	Facial Makeup Type
Dry	Liquid or Cream
Normal to Dry	Liquid or Cream
Normal to Oily	Oil-free liquid or Powder
Oily	Oil-free liquid with a mate finish

Table D.1: Facial makeup type with respect to skin type.

to perform inverse optical scattering without any a priori information on the skin scattering and absorption coefficients. However, this is independently modelled per pixel and can therefore not model the change of skin translucency without considering a global approach that captures the dependencies between pixels.

D.3 Brief Survey of Cosmetic Products

Facial Makeup

The goal of facial makeup is to make the skin looks flawless. Different facial makeup types will be used in conjunction with different skin types. This is shown in Table D.1.

Concealers, often called “cover sticks”, are used to hide specific areas on the skin such as baggy eyes, pimples, and other blemishes. The concealer is applied underneath the foundation and should be lighter than the regular skin colour since the second layer, the foundation, will even it out. Concealers come as liquids and compact sticks, the former being better for dry skin and the latter for oily skin.

Foundations come as liquids, creams, and powders. They are usually applied after the concealers on the totality of the face to make it look uniform and smooth. The foundation should be oil-based for dry skin, oil-free for oily skin, and water-based for combination skin.

Powders are applied over the foundation and are used to make some adjustments and keep the face looking fresh as the day wears on. There exist loose and pressed powders.

Blush should be the last makeup type applied on the face. It usually has a red tone to provide a healthy look to the skin. Blush comes in different forms such as powders, gels, and creams.

Eye Makeup

Eye makeup colour should be chosen to enhance the natural eye colour. Eyeliners are applied at the base of the eyelids and enhance the size and shape of the eyes. It can also be applied to the bottom of the eye the produce a more dramatic effect. Eyeliners come in many different colours and forms such as pencils, powders, cakes, and liquids.

Eyeshadows are applied on the eyelids and sometimes in-between the eyelids and the eyebrows. They also come in many different colours and forms such as creams, mates, and pencils.

Mascaras are used to enhanced eyelashes. Nowadays, mascara comes in many different colours.

Lip Makeup

Lipliners are applied around the perimeter of the lips. They are used to define the shape of the mouth and to hold the lipstick in place. Lipliners usually come under the form of pencils. Lipstick and lipliner should match and blend together. Lipsticks vary in types, textures, and colours. It is possible to find gloss, frost, mate, and cream lipsticks.

Appendix E

Pixel Radiance Plots and Rendered Faces

Bibliography

[1] Cinefex website. http://www.cinefex.com/home.html.

[2] Columbia-Utrecht reflectance and texture database. http://www1.cs.columbia.edu/CAVE/curet/.

[3] Kevin Aucoin's website. http://www.kevynaucoin.com/.

[4] Maggi hairstyles and cosmetics. http://www.sollab.net/maggi/index.

[5] Make-up artist magazine. www.makeupmag.com.

[6] Make-up mania. www.makeupmania.com.

[7] Makeup artist. www.makeupart.net.

[8] Makeup411. www.makeup411.com.

[9] Makeupalley. www.makeupalley.com.

[10] Shop online makeup section. http://makeup.all-the-stores.com.

[11] Soyouwanna do your makeup? www.soyouwanna.com/site/syws/makeup/makeup.html.

[12] Tipsofallsorts / makeup. www.tipsofallsorts.com/makeup.html.

[13] R. Anderson, B.S. Parrish, and J. Parrish. The optics of human skin. *J Invest Dermatol.*, 77(1):13–19, July 1981.

[14] E. Angelopoulou. The reflectance spectrum of human skin. Technical Report MS-CIS-99-29, University of Pennsylvania, December 1999.

[15] E. Angelopoulou. Understanding the color of human skin. In SPIE Press, editor, *Proceedings of the SPIE Conference on Human Vision and Electronic Imaging VI (SPIE)*, volume 4299, pages 243–251, May 2001.

[16] E. Angelopoulou. The uniqueness of the color of human skin. *Electronic Imaging (EI)*, 11(2):5, June 2001.

[17] E. Angelopoulou, R. Molana, and K. Daniilidis. Multispectral skin color modeling. Technical Report MS-CIS-01-22, University of Pennsylvania, June 2001.

[18] E. Angelopoulou, R. Molana, and K. Daniilidis. Multispectral skin color modelling. *IEEE conference on Computer Vision and Pattern Recognition (CVPR)*, pages 635–642, December 2001.

[19] M. Ashikhmin and P. Shirley. Steerable illumination textures. *ACM Transactions on Graphics*, 21(1):1–19, 2002.

[20] K. Aucoin. *The Art of Makeup*. Perennial, May 1996.

[21] K. Aucoin. *Face Forward*. Little Brown & Company, October 2000.

[22] Y. Bando, T. Kuratate, and T. Nishita. A simple method for modeling wrinkles on human skin. *10th Pacific Conference on Computer Graphics and Applications (PG'02)*, page 166, October 2002.

[23] B.G. Becker and N.L. Max. Smooth transitions between bump rendering algorithms. *Proceedings of SIGGRAPH'93*, 27:183–190, August 1993.

[24] P. Blasi, B. Le Saec, and C. Schlick. A rendering algorithm for discrete volume density objects. *Computer Graphics Forum*, 12(3):201–207, 1993.

[25] J.F. Blinn. Models of light reflection for computer synthesized pictures. *Computer Graphics*, 11(2):192–198, July 1977.

[26] J.F. Blinn. Light reflection functions for simulation of clouds and dusty surfaces. *Computer Graphics*, 16(3):21–29, July 1982.

[27] C.F. Bohren. Multiple scattering of light and some of its observable consequences. *American Journal of Physics*, 55(6):524–533, June 1987.

[28] L. Boissieux, G. Kiss, N. Magnenat-Thalmann, and P. Kalra. Simulation of skin aging and wrinkles with cosmetics insight. In *Proceedings of Eurographics Workshop on Animation and Simulation (EGCAS 2000)*, page 15, August 2000.

[29] R.F. Bonner, R. Nossal, S. Havlin, and G.H. Weiss. Model for photon migration in turbid biological media. *J. Opt. Soc. Am.*, 4:423–432, 1987.

[30] R.M. Boynton and C.X. Olson. Locating basic colors in the OSA space. *Color Research and Applications*, 12:94–105, 1987.

[31] S. Brabec and H.-P. Seidel. Shadow volumes on programmable graphics hardware. *Computer Graphics Forum*, 22(3):433, September 2003.

[32] M.J. Brooks and B.K. Horn. *Shape From Shading.* The MIT Press, July 1989.

[33] L.A. Brunsting and C. Sheard. The color of the skin as analyzed by spectrophotometric methods: *ii*. the role of pigmentation. *The Journal of Clinical Investigation*, 7:574–592, 1929.

[34] T.P. Bui. Illumination for computer generated pictures. *Communications of the ACM*, 18(6):311–317, 1975.

[35] H. Buiteveld, J.M.H. Hakvoort, and M. Donze. The optical properties of pure water. *In SPIE Proceedings on Ocean Optics XII*, 2258:174–183, 1994.

[36] B. Cabral, N.L. Max, and R. Springmeyer. Bidirectional reflection functions from surface bump maps. *Proceedings of SIGGRAPH'87*, 21:273–281, July 1987.

[37] N.A. Carr, J.D. Hall, and J.C. Hart. GPU algorithms for radiosity and subsurface scattering. In *Proceedings of the ACM SIGGRAPH/EUROGRAPHICS conference on Graphics hardware*, pages 51–59. Eurographics Association, 2003.

[38] S. Chandrasekhar. *Radiative Transfer.* Dover Publications, June 1960.

[39] W.-F. Cheong, S.A. Prahl, and A.J. Welch. A review of the optical properties of biological tissues. *IEEE J. Quant. Electron.*, 26:2166–2185, 1990.

[40] E. Claridge, S. Cotton, P. Hall, and M. Moncrieff. From colour to tissue histology: physics based interpretation of images of pigmented skin lesions. *Medical Image Computing and Computer-Assisted Intervention*, 2488:730–738, September 2002.

[41] E. Claridge and S.J. Preece. An inverse method for the recovery of tissue parameters from colour images. *Information Processing in Medical Imaging (IPMI)*, LNCS 2732:306–317, 2003.

[42] J.H. Clark. Hierarchical geometric models for visible surface algorithms. *Communications of the ACM*, 19(10):547–554, 1976.

[43] R.L. Cook and K.E. Torrance. A reflectance model for computer graphics. In *Proceedings of SIGGRAPH'81*, pages 307–316, 1981.

[44] O.R. Corson. *Fashions in Makeup, from Ancient to Modern Times.* Peter Owen Ltd., September 1997.

[45] R. Corson and J. Glavan. *Stage Makeup.* Allyn & Bacon, December 2000.

[46] S. Cotton and E. Claridge. Developing a predictive model of human skin colouring. *Proceedings of SPIE Medical Imaging*, 2708:814–825, 1996.

[47] O.G. Cula and K.J. Dana. Compact representation of bidirectional texture functions. *In Proceedings of IEEE Conference on Computer Vision and Pattern Recognition*, 1:1041–1047, 2001.

[48] O.G. Cula and K.J. Dana. Image-based skin analysis. In *The 2nd International Workshop on Texture Analysis and Synthesis*, pages 35–41, June 2002.

[49] C. Dachsbacher and M. Stamminger. Translucent shadow maps. In *Proceedings of the 13th Eurographics workshop on Rendering*, pages 197–201. Eurographics Association, 2003.

[50] K.J. Dana, B. van Ginneken, S.K. Nayar, and J.J. Koenderink. Reflectance and texture of real-world surfaces. *ACM Transactions on Graphics*, 18(1):1–34, 1999.

[51] P. Debevec, T. Hawkins, C. Tchou, H.-P. Duiker, W. Sarokin, and M. Sagar. Acquiring the reflectance field of a human face. In *Proceedings of SIGGRAPH'2000*, pages 145–156. ACM Press/Addison-Wesley Publishing Co., 2000.

[52] P. Delamar. *The Complete Make-Up Artist: Working in Film, Television and Theatre.* Northwestern University Press, March 1995.

[53] J. Dorsey, A. Edelman, H.W. Jensen, J. Legakis, and H. Køhling Pedersen. Modeling and rendering of weathered stone. In *Proceedings of SIGGRAPH'99*, pages 225–234. ACM Press/Addison-Wesley Publishing Co., 1999.

[54] G. Eason, A. Veitch, R. Nisbet, and F. Turnbull. The theory of the backscattering of light by blood. *J. Physics*, 11:1463–1479, 1978.

[55] V. Ebin. *The Body Decorated.* Thames and Hudson, November 1984.

[56] A.A. Efros and T.K. Leung. Texture synthesis by non-parametric sampling. *IEEE International Conference on Computer Vision*, pages 1033–1038, september 1999.

[57] T.J. Farell, M.S. Patterson, and B. Wilson. A diffusion theory model of spatially resolved, steady state diffuse reflectance for the noninvasive determination of tissue optical properties in vivo. *Med. Phys*, 19:879–888, July/August 1992.

[58] S. Fleishman, I. Drori, and D. Cohen-Or. Bilateral mesh denoising. *ACM Trans. Graph.*, 22(3):950–953, 2003.

[59] B. Fleming. *3D Photorealism Toolkit.* John Wiley & Sons, April 1998.

[60] B. Fleming. *Advanced 3D Photorealism Techniques.* John Wiley & Sons, June 1999.

[61] S.T. Flock, M.S. Patterson, B.C. Wilson, and D.R. Wyman. Monte Carlo modeling of light propagation in highly scattering tissue: I. model predictions and comparison with diffusion theory. *IEEE Trans. Biomed. Eng.*, 36:1162–1168, 1989.

[62] B. Flury. *Common Principal Components and Related Multivariate Models.* John Wiley & Sons, 1988.

[63] A. Fournier. Filtering normal maps and creating multiple surfaces. Technical Report TR-92-41, University of British Columbia, 1992.

[64] A. Fournier. Normal distribution functions and multiple surfaces. *Graphics Interface Workshop on Local Illumination*, pages 45–52, May 1992.

[65] R.K. Freinkel and D.T. Woodley. *The Biology of the Skin.* CRC Press-Parthenon Publishers, March 2001.

[66] K. Furutso. Diffusion equation derived from space-time transport equation. *J. Opt. Soc. Am.*, 70:360, 1980.

[67] A. Georghiades, P. Belhumeur, and D. Kriegman. Illumination-based image synthesis: creating novel images of human faces under differing pose and lighting. *In Proc. Workshop on Multi-View Modeling and Analysis of Visual Scenes*, pages 47–54, 1999.

[68] A.S. Glassner. *Principles of Digital Image Synthesis.* Morgan Kaufman, 1995.

[69] B. Gooch and A.A. Gooch. *Non-Photorealistic Rendering.* A K Peters Ltd, July 2001.

[70] W.B. Gratzer. Tabulated molar extinction coefficient for hemoglobin in water. Med. Res. Council Labs, London. Data compiled by Scott Prahl (prahl@ece.ogi.edu).

[71] B. Guenter, C. Grimm, D. Wood, H. Malvar, and F. Pighin. Making faces. In *Proceedings of SIGGRAPH'98*, pages 55–66. ACM Press, 1998.

[72] C.S. Haase and G.W. Meyer. Modeling pigmented materials for realistic image synthesis. *ACM Transactions on Graphics (TOG)*, 11(4):305–335, 1992.

[73] T. Hachisuka. Real-time BSSRDF (in japanese). http://members.jcom.home.ne.jp/himatsubushi/cnt_html/diary.html.

[74] P. Hanrahan and W. Krueger. Reflection from layered surfaces due to subsurface scattering. In *Proceedings of SIGGRAPH'93*, pages 165–174. ACM Press, 1993.

[75] X. Hao, T. Baby, and A. Varshney. Interactive subsurface scattering for translucent meshes. *ACM Symposium on Interactive 3D Graphics*, pages 75–82, April 2003.

[76] A. Haro, B. Guenter, and I. Essa. Real-time, photo-realistic, physically based rendering of fine scale human skin structure. *Proceedings of the 12th Eurographics Workshop on Rendering*, pages 53–62, June 2001.

[77] G.A. Harrison. *Genetical Variation in Human Populations.* Pergamon, Oxford, 1961.

[78] X.D. He, K.E. Torrance, F.X. Sillion, and D.P. Greenberg. A comprehensive physical model for light reflection. In *Proceedings of SIGGRAPH'91*, pages 175–186. ACM Press, 1991.

[79] P.S. Heckbert. Writing a ray tracer. In Andrew S. Glassner, editor, *An Introduction to Ray Tracing*, pages 263–294. Academic Press, 1990.

[80] W. Heidrich, K. Daubert, J. Kautz, and H.-P. Seidel. Illuminating micro geometry based on precomputed visibility. In *Proceedings of SIGGRAPH'2000*, pages 455–464. ACM Press/Addison-Wesley Publishing Co., 2000.

[81] L. Henyey and J. Greenstein. Diffuse radiation in the galaxy. *Astrophys. Journal*, 93:70–83, 1941.

[82] C. Hery. Stupid RenderMan tricks on shadow buffers... http://www.renderman.org/RMR/Examples/srt2002/PrmanUserGroup2002.ppt.

[83] C. Hery. Implementing a skin BSSRDF (or several...). Chapter 4, Siggraph 2003 RenderMan course notes, July 2003.

[84] K.E. Hoff, J. Keyser, M. Lin, D. Manocha, and T. Culver. Fast computation of generalized Voronoi diagrams using graphics hardware. In *Proceedings of SIGGRAPH'99*, pages 277–286. ACM Press/Addison-Wesley Publishing Co., 1999.

[85] H.K. Hussein. Towards realistic facial modeling and re-rendering of human skin aging animation. *Shape Modeling International 2002 (SMI'02)*, page 205, May 2002.

[86] A. Hyvarinen, J. Karhunen, and E. Oja. *Independent Component Analysis.* Wiley-Interscience, May 2001.

[87] T. Igarashi and J.F. Hughes. Clothing manipulation. *15th Annual Symposium on User Interface Software and Technology*, pages 91–100, October 2002.

[88] F. H. Imai, N. Tsumura, H. Haneishi, and Y. Miyake. Principal component analysis of skin color and its application to colorimetric color reproduction on CRT display and hardcopy. *J. Image Science and Technology*, 40(5):422–430, 1996.

[89] T. Ishii, T. Kurachi, T. Yasuda, S. Yokoi, and J.-I. Toriwaki. Rendering the surface of skin using Voronoi-division. *IPSJ SIGNotes Computer Graphics and Cad*, 46(9), 1990.

[90] T. Ishii, T. Yasuda, and J. Toriwaki. A generation model for human skin texture. *Proc. CG International '93: Communicating with Virtual Worlds*, pages 139–150, 1993.

[91] T. Ishii, T. Yasuda, S. Yokoi, and J.-I. Toriwaki. Human skin rendering based on the surface microstructures. *Information Processing Society of Japan Journal*, 32(5), 1991.

[92] J.E. Jackson. *A User's Guide to Principal Components.* John Wiley & Sons, 1991.

[93] S.L. Jacques. Origins of tissue optical properties in the UVA, visible and NIR regions. *Advances in Optical Imaging and Photon Migration*, 2:364–370, 1996.

[94] S.L. Jacques. Skin optics. Oregon Medical Laser Center News, January 1998. http://omlc.ogi.edu/news/jan98/skinoptics.html.

[95] H.W. Jensen. *Realistic Image Synthesis Using Photon Mapping.* AK Peters, 2001.

[96] H.W. Jensen and J. Buhler. A rapid hierarchical rendering technique for translucent materials. In *Proceedings of SIGGRAPH'2002*, pages 576–581. ACM Press, July 2002.

[97] H.W. Jensen, S.R. Marschner, M. Levoy, and P. Hanrahan. A practical model for subsurface light transport. *Proceedings of SIGGRAPH'2001*, pages 511–518, August 2001.

[98] T.R. Jones, F. Durand, and M. Desbrun. Non-iterative, feature-preserving mesh smoothing. *ACM Trans. Graph.*, 22(3):943–949, 2003.

[99] L. Kahney. Real agents for virtual models. Wired News, July 1999. http://www.wired.com/news/culture/0,1284,20736,00.html.

[100] J.T. Kajiya. The rendering equation. In *Proceedings of SIGGRAPH'86*, pages 143–150. ACM Press, 1986.

[101] J.T. Kajiya and T.L. Kay. Rendering fur with three dimensional textures. *Computer Graphics*, 23(3):271–280, 1989.

[102] P. Kalra and N. Magnenat-Thalmann. Simulation of facial skin using texture mapping and coloration. In S.P. Mudur and S.N. Pattanaik, editors, *Graphics, Design and Visualization, Proceedings of ICCG '93*, pages 365–374, 1993.

[103] P. Kalra and N. Magnenat-Thalmann. Modeling of vascular expressions in facial animation. *Computer Animation*, pages 50–58, 1994.

[104] M. Kaplan. A painterly approach to human skin. http://citeseer.nj.nec.com/467916.html.

[105] J. Kautz, W. Heidrich, and H.-P. Seidel. Real-time bump map synthesis. In *Proceedings of the ACM SIGGRAPH/EUROGRAPHICS Workshop on Graphics Hardware*, pages 109–114. ACM Press, 2001.

[106] V.J-R Kehoe. *Special Make-Up Effects.* Focal Press, February 1991.

[107] M. Keijzer, S.L. Jacques, S.A. Prahl, and A.J. Welch. Light distributions in artery tissue: Monte Carlo simulations for finite-diameter laser beams. *Laser Surg. Med.*, 9:148–154, 1989.

[108] M. Keijzr, W.M. Star, and P.R.M. Storchi. Optical diffusion in layered media. *Applied Optics*, 27(9):1820–1824, 1988.

[109] M. Kenji, W. Yasuhiko, and S. Yasuhito. A survey on rendering of human image. *IPSJ SIGNotes Computer Graphics and Cad*, 46(3), 1990.

[110] A. Kienle and M.S. Patterson. Improved solutions of the steady-state and the time-resolved diffusion equations for reflectance from semi-infinite turbid medium. *J. Opt. Soc. Am.*, 14:246–254, 1997.

[111] T.-Y. Kim and U. Neumann. Interactive multiresolution hair modeling and editing. In *Proceedings of SIGGRAPH'2002*, pages 620–629. ACM Press, 2002.

[112] R.V. Klassen. Modeling the effect of the atmosphere on light. *ACM Transactions on Graphics*, 6(3):215–237, July 1987.

[113] J. Kniss, S. Premoze, C. Hansen, and D. Ebert. Interactive translucent volume rendering and procedural modeling. In *Proceedings of the conference on Visualization '02*, pages 109–116. IEEE Press, 2002.

[114] J.J. Koenderinck and A. van Doorn. Shading in the case of translucent objects. *In Proceedings of SPIE*, 4299:312–320, 2001.

[115] J.J. Koenderink and S.C. Pont. The secret of velvety skin. *Special Issue on Human Modeling, Analysis and Synthesis of Machine Vision and Applications*, 14:260–268, 2002.

[116] J.J. Koenderink and A. van Doorn. Phenomenological description of bidirectional surface reflection. *J. Opt. Soc. Am. A*, 15(11):2903–2912, November 1998.

[117] V.J.-R. Kohoe. *The Technique of the Professional Make-Up Artist.* Focal Press; Revised edition, June 1995.

[118] A.A. Kokhanovsky. *Optics of Light Scattering Media: Problems and Solutions.* John Wiley & Son Ltd, March 1999.

[119] N. Kollias. Tabulated molar extinction coefficient for hemoglobin in water. Wellman Laboratories, Harvard Medical School, Boston. Data compiled by Scott Prahl (prahl@ece.ogi.edu).

[120] P. Kubelka. New contributions to the optics of intensely light-scattering materials, part *i*. *Journal of the Optical Society of America*, 38(5):448–457, May 1948.

[121] P. Kubelka. New contributions to the optics of intensely light-scattering materials, part *ii*: Nonhomogeneous layers. *Journal of the Optical Society of America*, 44(4):330–335, April 1954.

[122] P. Kubelka and F. Munk. Ein beitrag zur optik der farbanstriche (translation by Steve Westin available at http://graphics.cornell.edu/∼westin/pubs/kubelka.pdf). *Z. Tech. Physik.*, 12:593, 1931.

[123] J.M. Kukla and E.J. Bedwell. A procedural texture for epidermal tissue. University of Maryland Baltimore County. http://www.csee.umbc.edu/∼ebedwe/skin/.

[124] E.P.F. Lafortune, S.-C. Foo, K.E. Torrance, and D.P. Greenberg. Non-linear approximation of reflectance functions. In *Proceedings of SIGGRAPH'97*, pages 117–126. ACM Press/Addison-Wesley Publishing Co., 1997.

[125] L. Lefebvre and P. Poulin. Extraction and synthesis of bump maps from photographs. Graphics Interface Posters Proceedings, May 2000.

[126] H. Lensch, M.Goesele, P. Bekaert, J. Kautz, M. Magnor, J. Lang, and H.-P. Seidel. Interactive rendering of translucent objects. *Proceedings of Pacific Graphics'02*, pages 214–224, October 2002.

[127] W.F. Lever and G. Schaumburg-Lever. *Histopathology of the Skin.* J.B. Lippincott Company, 1990.

[128] R. Lu, J.J. Koenderink, and A.M.L. Kappers. Optical properties (bidirectional reflection distribution functions) of velvet. *Applied Optics*, 37(25):5974–5984, 1998.

[129] J.M. Macy. Emotive components in facial skin textures of realistic 3d computer generated characters. MFA Thesis Progress, Spring 2003. http://www.accad.ohio-state.edu/∼jmacy/Thesis/index.html.

[130] A. Madrano. A colorful history. http://influx.uoregon.edu/1999/makeup/history.html.

[131] S. Magda, T. Zickler, D. Kriegman, and P. Belhumeur. Beyond Lambert: reconstructing surfaces with arbitrary BRDFs. In *International Conference on Computer Vision*, volume 2, pages 391–399, 2001.

[132] L.T. Maloney. Evaluation of linear models of surface spectral reflectance with small numbers of parameters. *Journal of the Optical Society of America A*, 3:1673–1683, 1986.

[133] T. Malzbender, D. Gelb, and H. Wolters. Polynomial texture maps. In *Proceedings of SIGGRAPH'2001*, pages 519–528. ACM Press, 2001.

[134] W.R. Mark, R.S. Glanville, K. Akeley, and M.J. Kilgard. Cg: a system for programming graphics hardware in a C-like language. *ACM Trans. Graph.*, 22(3):896–907, 2003.

[135] L. Markosian. *Art-based Modeling and Rendering for Computer Graphics*. PhD thesis, Brown University, May 2000.

[136] S.R. Marschner. *Inverse Rendering for Computer Graphics*. PhD thesis, Cornell University, 1998.

[137] S.R. Marschner, B. Guenter, and S. Raghupathy. Modeling and rendering for realistic facial animation. In *Proceedings of the 11th Eurographics Rendering Workshop*, pages 231–242, June 2000.

[138] S.R. Marschner, S.H. Westin, E.P.F. Lafortune, and K.E. Torrance. Image-based measurement of the bidirectional reflectance distribution function. *Applied Optics*, 39(16):2592–2600, June 2000.

[139] S.R. Marschner, S.H. Westin, E.P.F. Lafortune, K.E. Torrance, and D.P. Greenberg. Image-based BRDF measurement including human skin. *Proceedings of the 10th Eurographics Rendering Workshop*, pages 139–152, 1999.

[140] S.R. Marschner, S.H. Westin, E.P.F. Lafortune, K.E. Torrance, and D.P. Greenberg. Reflectance measurements of human skin. Technical Report PCG-99-2, Cornell University, 1999.

[141] ATI Developer GDC 2003 Material. Advanced visual effects with Direct3d - special effects. http://www.ati.com/developer/.

[142] A. Matsumoto, H. Saito, and S. Ozawa. 3d reconstruction of skin surface from photometric stereo images with specular and inter-reflections. *The 4th International Conference on Control, Automation, Robotics, and Vision*, 2:778–782, 1996.

[143] A. Matsumoto, H. Saito, and S. Ozawa. 3d reconstruction of skin surface from photometric stereo images with specular and inter-reflections. *Transactions of the Institute of Electrical Engineers of Japan*, 117-C(10):1391–1397, 1997.

[144] N. Max. Horizon mapping: shadows for bump-mapped surfaces. *The Visual Computer*, 4(2):109–117, July 1988.

[145] I.V. Meglinski and S.J. Matcher. The analysis of spatial distribution of the detector depth sensitivity in multi-layered inhomogeneous highly scattering and absorbing medium by the Monte Carlo technique. *Opt. Spectrosc.*, 91:654–659, 2001.

[146] I.V. Meglinski and S.J. Matcher. Modelling the sampling volume for the skin blood oxygenation measurements. *Med. Biol. Eng. Comput.*, 39:44–50, 2001.

[147] I.V. Meglinski and S.J. Matcher. Quantitative assessment of skin layers absorption and skin reflectance spectra simulation in the visible and near-infrared spectral regions. *Physiol. Meas.*, 23:741–753, November 2002.

[148] I.V. Meglinski and S.J. Matcher. Computer simulation of the skin reflectance spectra. *Comput Methods Programs Biomed.*, 70(2):179–186, 2003.

[149] T. Mertens, J. Kautz, P. Bekaert, H.-P. Seidel, and F. van Reeth. Interactive rendering

of translucent deformable objects. In *Proceedings of the 13th Eurographics workshop on Rendering*, pages 130–140. Eurographics Association, 2003.

[150] G. Miller. Efficient algorithms for local and global accessibility shading. In *Proceedings of SIGGRAPH'94*, pages 319–326. ACM Press, 1994.

[151] P.F. Millington and R. Wilkinson. *Skin (Biological structure and function; 9).* Cambridge University Press, 1983.

[152] W. Montagna and P.F. Parakkal. *The Structure and Function of Skin.* Academic Press, November 1997.

[153] T. Morawetz. *Making Faces, Playing God: Identity and the Art of Transformational Makeup.* University of Texas Press, August 2001.

[154] G.R. Nadrich. Monkeying around with makeup. FOX News, July 2001. http://www.foxnews.com/story/0,2933,30513,00.html.

[155] M. Nahas, H. Huitric, M. Rioux, and J. Domey. Facial image synthesis using skin texture recording. *The Visual Computer*, 6(6):337–343, 1990.

[156] F. Nars and F. Baron. *Makeup Your Mind.* PowerHouse Books, January 2002.

[157] S.K. Nayar and M. Oren. Generalization of the Lambertian model and implications for machine vision. *International Journal of Computer Vision*, 14:227–251, 1995.

[158] C.S.-L. Ng. *Simulation and rendering of skin-like surfaces.* PhD thesis, Nanyang Technological University, 2001.

[159] C.S.-L. Ng and L. Li. A multi-layered reflection model of natural human skin. *Computer Graphics International 2001 (CGI'01)*, pages 249–256, July 2001.

[160] C.S.-L. Ng and L. Li. A psychophysically-based colour model for human skin. *International Conference on Imaging Science, Systems, and Technology*, 2001.

[161] F.E. Nicodemus, J.C. Richmond, and J.J. Hsia. Geometrical considerations and reflectance. National Bureau of Standards, October 1977.

[162] K. Niimoto, Y. Honda, and S. Kaneko. A formalization of photometric stereo method using two light sources and its application to reconstruction of human skin replicas. *Trans. IEICE D-II*, pages 10–18, 1999.

[163] T. Nishita, Y. Miyawaki, and E. Nakamae. A shading model for atmospheric scattering considering luminous intensity distribution of light sources. In *Proceedings of SIGGRAPH'87*, pages 303–310. ACM Press, July 1987.

[164] Nvidia. Cg skin shader. http://developer.nvidia.com.

[165] N. Ojima. Application of spectral information to the analysis of skin applied with cosmetics. *Journal of the Society of Photographic Science and Technology of Japan*, 65:264, 2002.

[166] N. Ojima, T. Minami, and M. Kawai. Transmittance measurement of cosmetic layer applied on skin by using image processing. In *In Proceeding of The 3rd Scientific Conference of the Asian Societies of Cosmetic Scientists*, page 114, 1997.

[167] N. Ojima, K. Yoshida, O. Osanai, and S. Akasaki. Image synthesis of cosmetic applied to skin based on optical properties of foundation layers. In *In Proceedings of International Congress of Imaging Science*, pages 467–468, 2002.

[168] E. Okada, M. Firbank, M. Schweiger, S.R. Arridge, M. Cope, and D.T. Delpy. Theoretical and experimental investigation of near-infrared propagation in a model of the adult head. *Appl. Opt.*, 36:21–31, 1997.

[169] M. Olano and M. North. Normal distribution mapping. Technical Report 97-041, University of North Carolina at Chapel Hill, 1997.

[170] M. Oren and S.K. Nayar. Generalization of Lambert's reflectance model. In *Proceedings of SIGGRAPH'94*, pages 239–246. ACM Press, 1994.

[171] F.I. Parke and K. Waters. *Computer Facial Animation.* A.K. Peters, 1996.

[172] M. Patel. Colouration issues in computer generated facial animation. *Computer Graphics Forum*, 14(2):117–126, June 1995.

[173] M. Pharr. Layered media for surface shaders. SIGGRAPH'2001 RenderMan Course Notes, July 2001.

[174] M. Pharr and P. Hanrahan. Monte Carlo evaluation of non-linear scattering equations for subsurface reflection. In *Proceedings of SIGGRAPH'2000*, pages 75–84. ACM Press/Addison-Wesley Publishing Co., 2000.

[175] M. Pharr and G. Humphreys. *Physically-Based Image Synthesis: Design and Implementation of a Rendering System.* Draft, (April 2nd 2003), to appear.

[176] G. Poirier. References for human skin modelling and rendering, December 2003. http://www.cgl.uwaterloo.ca/∼gpoirier/thesis/references.htm.

[177] P. Poulin and A. Fournier. A model for anisotropic reflection. In *Proceedings of SIGGRAPH'90*, pages 273–282. ACM Press, 1990.

[178] S.A. Prahl. Optical absorption of hemoglobin. Oregon Medical Laser Center. http://omlc.ogi.edu/spectra/hemoglobin/index.html.

[179] S.A. Prahl. *Light Transport in Tissue.* PhD thesis, University of Texas at Austin, 1988.

[180] S.A. Prahl, M. Keijzer, S.L. Jacques, and A.J. Welch. A Monte Carlo model of light propagation in tissue. *SPIE Institute Series*, 5:102–111, 1989.

[181] E. Praun, A. Finkelstein, and H. Hoppe. Lapped textures. In *Proceedings of SIGGRAPH' 2000*, pages 465–470, 2000.

[182] Y.M. Proshina and N.A. Razumikhina. In vivo studies of human skin optical reflectance. *Proceedings of the SPIE - The International Society for Optical Engineering*, 4001:286, 2000.

[183] S. Roberts and R. Everson. *Independent Component Analysis : Principles and Practice.* Cambridge University Press, March 2001.

[184] H. Rushmeier, G. Taubin, and A. Guéziec. Applying shape from lighting variation to bump map capture. *In Rendering Techniques '97*, pages 35–44, June 1997.

[185] I.S. Saidi. *Transcutaneous Optical Measurement of Hyperbilirubinemia in Neonates*. PhD thesis, Rice University, 1992.

[186] H. Saito, Y. Somiya, and S. Ozawa. Shape reconstruction of skin surface from shading images using simulated annealing. *ACCV'95*, 3:348–352, December 1995.

[187] H. Saito, Y. Somiya, and S. Ozawa. 3d reconstruction of skin surface from multi-shading images including shadows. *Transactions of the Society of Instrument and Control Engineers*, 32(8):1160–1167, 1996.

[188] D. Sartor and J. Pivovarnick. *Theatrical FX Makeup, Book and CD-ROM edition*. Heinemann, September 2001.

[189] C. Schlick. *Divers elements pour une synthese d'images realistes*. PhD thesis, Universite Bordeaux 1, November 1992.

[190] C. Schlick. An inexpensive BRDF model for physically based rendering. *Computer Graphics Forum*, 13(3):233–246, Septembre 1994.

[191] A. Secord. Weighted voronoi stippling. In *Proceedings of the second international symposium on Non-photorealistic animation and rendering*, pages 37–43, 2002.

[192] H. Shimizu, K. Uetsuki, N. Tsumura, Y. Miyake, and N. Ojima. Analyzing the effect of cosmetic essence by independent component analysis for skin color images. In *Proceedings of the Third International Conference on Multispectral Color Science*, pages 65–68, June 2001.

[193] P.-P.J. Sloan and M. Cohen. Hardware accelerated horizon mapping. *Proceedings of the 11th Eurographics Workshop on Rendering*, pages 281–286, June 2000.

[194] H. Song, D.C. Banks, and A. Srivastava. Measuring a surface's reflectance and re-mapping it to new surfaces. Florida State University, 2003. http://ww2.cs.fsu.edu/∼hui/research/reflectance_remap.html.

[195] R.E. Spear. *The Divine Guido: Religion, Sex, Money and Art in the World of Guido Reni*. Yale University Press, December 1997.

[196] S. Stahlberg. Tutorials and evolution. http://www.optidigit.com/stevens/.

[197] J. Stam. Multiple scattering as a diffusion process. In *Proceedings of the 6th Eurographics Workshop on Rendering*, pages 69–79, June 1995.

[198] J. Stam. Diffraction shaders. In *Proceedings of SIGGRAPH'99*, pages 101–110. ACM Press/Addison-Wesley Publishing Co., 1999.

[199] J. Stam. An illumination model for a skin layer bounded by rough surfaces. *Proceedings of the 12th Eurographics Workshop on Rendering*, pages 39–52, June 2001.

[200] P. Strauss. A realistic lighting model for computer animators. *IEEE Computer Graphics and Applications*, 10(6):56–64, November 1990.

[201] T. Strothotte and S. Schlechtweg. *Non-Photorealistic Computer Graphics: Modeling, Rendering and Animation*. Morgan Kaufmann, June 2002.

[202] Y. Su, W. Wang, K. Xu, and C. Jiang. Optical properties of skin. *Proceedings of the SPIE - The International Society for Optical Engineering*, 4916:299, 2002.

[203] R. Swinfield. *Stage Makeup Step-By-Step*. Betterway Pubns, March 1995.

[204] G. Szabò, A.B. Gerald, M.A. Pathak, and T.B. Fitzpatrick. Racial differences in the fate of melanosomes in human epidermis. *Nature (London)*, 222:1081, 1969.

[205] Y. Takemae, T. Morimaya, and S. Ozawa. The correspondence between physical features and subjective evaluation on skin image. In *IEICE General Conference*, page 268, 1999.

[206] Y. Takemae, H. Saito, and S. Ozawa. The evaluating system of human skin surface condition by image processing. *IEEE International Conference on Systems, Man, and Cybernetics*, 2000.

[207] M. Tarini, H. Yamauchi, J. Haber, and H.-P. Seidel. Texturing faces. In *Proceedings Graphics Interface 2002*, pages 89–98, 2002.

[208] L. Thudium. *Stage Makeup: The Actor's Complete Step-By-Step Guide to Today's Techniques and Materials*. Back Stage Books, April 1999.

[209] E. Tomson. Human skin for "Finding Nemo", practical subsurface scattering with RenderMan. Chapter 5, Siggraph 2003 RenderMan course notes, July 2003.

[210] K.E. Torrance and E.M. Sparrow. Theory of off-specular reflection from roughened surfaces. *Journal of the Optical Society of America*, 57:1104–1114, September 1967.

[211] N. Tsumura, H. Haneishi, and Y. Miyake. Independent component analysis of skin color image. *Journal of Optical Society of America*, 16(9):2169–2176, 1999.

[212] N. Tsumura, H. Haneishi, and Y. Miyake. Independent component analysis of spectral absorbance image in human skin. *Optical Review*, 7(6):479–482, 2000.

[213] N. Tsumura, M. Kawabuchi, H. Haneishi, and Y. Miyake. Mapping pigmentation in human skin from multi-channel visible spectrum image by inverse optical scattering technique. *Journal of Imaging Science and Technology*, 45(5):444–450, 2001.

[214] N. Tsumura, N. Ojima, K. Sato, M. Shiraishi, H. Shimizu, H. Nabeshima, S. Akazaki, K. Hori, and Y. Miyake. Image-based skin color and texture analysis/synthesis by extracting hemoglobin and melanin information in the skin. *Proceedings of SIGGRAPH' 2003*, 22(3):770–779, 2003.

[215] V.V. Tuchin. Light scattering study of tissue. *Physics - Uspekhi*, 40(5):495–515, 1997.

[216] G. Turk. Generating textures on arbitrary surfaces using reaction-diffusion. In *Proceedings of SIGGRAPH'91*, pages 289–298. ACM Press, 1991.

[217] G. Turk. Re-tiling polygonal surfaces. *Computer Graphics*, 26(2):55–64, 1992.

[218] M.J.C. van Gemert, S.L. Jacques, H.J.C.M Sterenborg, and W.M.Star. Skin optics. *IEEE Transactions on Biomedical Engineering*, 36(12):1146–1154, 1989.

[219] M.L. Viaud and H. Yahia. Facial animation with wrinkles. *Proc. Eurographics Workshop on Animation and Simulation '92*, pages 1–13, 1992.

[220] P. Volino and N. Magnenat-Thalmann. Fast geometrical wrinkles on animated surfaces. *Proc. WSCG'99*, 1999.

[221] L.V. Wang. Rapid modelling of diffuse reflectance of light in turbid slabs. *J. Opt. Soc. Am.*, 15(4):936–944, 1998.

[222] L.V. Wang, S.L. Jacques, and L. Zheng. MCML — Monte Carlo modelling of light transport in multi-layered tissues. *Comput. Methods Programs Biomed.*, 47:131–146, 1995.

[223] G.J. Ward. Measuring and modeling anisotropic reflection. In *Proceedings of SIGGRAPH'92*, pages 265–272. ACM Press, 1992.

[224] Alias Wavefront. Maya skin shader. http://www.aliaswavefront.com. Community, Download.

[225] L.-Y. Wei and M. Levoy. Fast texture synthesis using tree-structured vector quantization. In *Proceedings of SIGGRAPH' 2000*, pages 479–488, 2000.

[226] S.H. Westin, J.R. Arvo, and K.E. Torrance. Predicting reflectance functions from complex surfaces. *Proceedings of SIGGRAPH'92*, 26:255–264, July 1992.

[227] J.T. Whitton and J.D. Everall. The thickness of the epidermis. *British Journal of Dermatology*, 89:467–476, 1973.

[228] J. Wiedemann. *Digital Beauties.* TASCHEN America Llc, December 2001.

[229] J. Wiedemann. *Digital Beauties: 2nd and 3rd Computer Generated Digital Models.* TASCHEN America Llc, December 2002.

[230] L. Williams. Casting curved shadows on curved surfaces. In *Proceedings of SIGGRAPH'78*, pages 270–274. ACM Press, 1978.

[231] B.C. Wilson and G. Adam. A Monte Carlo model for absorption and flux distributions of light in tissue. *Med. Phys.*, 10:824–830, 1983.

[232] E.J. Wood and P.T. Bladon. *The Human Skin; Studies in Biology no. 164*. Edward Arnold, publishers, 1985.

[233] S. Worley. A cellular texture basis function. In *Proceedings of SIGGRAPH'96*, pages 291–294. ACM Press, 1996.

[234] S. Wray, M. Cope, D.T. Delpy, J.S. Wyatt, and E.O.R. Reynolds. Characterization of the near infrared absorption spectra of cytochrome aa3 and haemoglobin for the non-invasive monitoring of cerebral oxygenation. *Biochimica et Biophsica Acta*, 933:184–192, 1988.

[235] Y. Wu, P. Kalra, and N. Magnenat-Thalmann. Physically-based wrinkle simulation and skin rendering. *EGCAS'97*, September 1997.

[236] Y. Wu, P. Kalra, L. Moccozet, and N. Magnenat-Thalmann. Simulating wrinkles and skin aging. *The Visual Computer*, 15(4):183–198, 1999.

[237] Y. Wu, P. Kalra, and N.M. Thalmann. Simulation of static and dynamic wrinkles of skin. *Proc. Computer Animation'96*, pages 90–97, 1996.

[238] Y. Wu, N.M. Thalmann, and D. Thalmann. A plastic-visco-elastic model for wrinkles in facial animation and skin aging. *Proc. Pacific Graphics'94*, pages 201–213, 1994.

[239] T. Yamada, H. Saito, and S. Ozawa. 3d reconstruction of skin surface from image sequence. *IAPR Workshop on Machine Vision Applications (MVA98)*, November 1998.

[240] T. Yamada, H. Saito, and S. Ozawa. 3d shape inspection of skin surface from rotation of light source. *QCAV'99*, pages 245–251, 1999.

[241] I.V. Yaroslavsky and V.V. Tuchin. Light transport in multilayered scattering media. Monte Carlo modelling. *Opt. Spectrosc.*, 72:934–939, 1992.

[242] U. Yoshiaki, U. Munetoshi, K. Tsuneya, and A. Ken-ichi. Methods for human modeling skin, hair, and walking. *IPSJ SIGNotes Computer Graphics and Cad*, 46(11), 1990.

[243] Y. Yu, K. Dana, H. Rushmeier, S. Marschner, S. Premoze, and Y. Sato. Image-based surface details. SIGGRAPH'2000 Course Notes, July 2000.

Index